Corrosion Behavior of Aluminum-Based Materials in Polymer Electrolyte Membrane Fuel Cell Environment

Doctoral Thesis

March 2024

岩手大学
IWATE UNIVERSITY

Aklima Jahan

Graduate School of Science and Engineering
Faculty of Science and Engineering
Iwate University, Japan

Contents

Chapter 1

Introduction

Chapter 1: Introduction

1-1 Background and general framework of fuel cells

Energy necessities are rising with enduring industrialization, population growth, and technological advancements. So, the harmless, ecologically friendly, and unfailing power supplies are vital to mankind for sustainability and a better quality of life. However, fossil fuel assets are decreasing quickly in parallel with increasing energy demand. Energy and the atmosphere are of universal apprehension, which has enthused worldwide research on fresh, effective, and sustainable energy technologies. Cosmological energy, wind energy, geothermal energy, bioenergy, hydropower, ocean energy, and fuel cells are among the most well-known renewable energy sources that could potentially exchange dependency on fossil fuels. In the circumstances of sustainable development, exploring clean air and green energy generation is a routine apprehension; the fresh hydrogen energy created by technologies such as fuel cells, the key solutions for the 21st century,[1, 2] and water electrolysis[3, 4] have attracted vast research interests.

However, resourceful energy carriers are essential for movable applications.[5] Thermal and electrical energy can be efficiently generated from hydrogen, methanol, and natural gas using fuel cells, which convert chemical energy to electrical energy.[6, 7] In recent decades, because of their high proficiency and limited discharge, fuel cells have attracted more and more attention for their ability to generate water and heat via the direct, effective conversion of chemical energy into electrical energy.[8, 9] For the time being, they can be a solution for serious worries such as the deficiency of fossil fuel resources and crises in environmental pollution.

Therefore, several countries, in their national strategies, implement measures to promote the fuel cell industry by including hydrogen development. For instance, the government of Japan has raised hydrogen energy to a national strategy, including a mature manufacturing chain leading in technology with a manufacture capacity of over 800,000-unit FCV by 2030 of Toyota Mirai, more than 5.3m sets of Ene-farm, and more than 320 hydrogen refueling system (HRS) by 2025.[10] The planned strategic roadmap for hydrogen and fuel cells in Japan[11] are represented in **Fig. 1.** Japan has addressed a complete roadmap for hydrogen manufacture, fuel cell automobiles, and saleable applications from 2020 to 2030.

Goals for hydrogen production	Goals for FCV (200k)	
Cost of brown coal gasification (¥ 12/kWh) Durability: 130,000 hours; Scale-up of liquefied hydrogen tank (50,000m^3) Higer efficiency of Liquefaction (6 kWh/kg)	Cost of main FCV system FC (¥ 5k/kW) Hydrogen storage (¥ 0.3m) Goals for HRS (320) Construction cost (¥ 200) Operating cost (¥ 15m/year), Compressor (¥ 50m), Accumulator (¥ 10m)	Goals for FCV (800) k Goals for HRS (900) k Goals for Bus (1,200) k Cost of FC bus will be half (¥ 52.5m)

2020 **2025** **2030**

Goals for stationary fuel cell	Goals for commercial application	
Ene-farm Cost: ¥ 800k (PEMFC) ¥ million (SOFC) Efficiency of hydrogen power generation: 27% for 1MW scale	Efficiency: over 55 % Durability: 130,000 hours: Realize grid- parity combining the utilization of exhaust hears: Low voltage: CAPEX (¥ 500,000/kW), power generation cost (¥ 25/kwh) High voltage: CAPEX (¥300,000kW, Power generation cost (¥ 17/kWh)	Establishment of the technology for commercialization of hydrogen power generation *Goals for hydrogen supply chain* CIF cost (¥ 30/Nm^3) Cost of electrolyzer: (¥ 50.000/kW) Energy consumption (4.3 kWh/Nm^2) *Goals for Ene-farm* 5.3 million cumulative sales and recover investment.

Fig. 1 Strategy and roadmap of Japan for hydrogen and fuel cells from 2020 to 2035.

Since fuel cells contain fewer moving parts, they emit fewer pollutants during operation. Based on the type of electrolyte used, fuel cells can be classified into different categories, such as alkaline, phosphoric acid, molten carbonate, solid oxide, etc. Therefore, the classification and features of fuel cells are shown in **Table 1-1.**

Table 1-1: The classification and features of fuel cells.

Fuel cell	**Electrolyte**	**Temperature (K)**	**Efficiency (%)**	**Application**
Polymer Electrolyte Membrane Fuel Cell（PEMFC）	Polymer Electrolyte Membrane	~373	40~50	Vehicle Stationary
Phosphoric Acid Fuel Cell （PAFC）	H_3PO_4	473	40~45	Stationary
Alkaline Fuel Cell （AFC）	KOH/H_2O	~373	50~70	Space application
Molten Carbonate Fuel Cell （MCFC）	Molten Carbonate	923	50~60	Stationary （high temperature type）
Solid Oxide Zirconium Fuel Cell （SOFC）	Zirconium	973~	50~60	Stationary （high temperature type）

1-2 Outline of PEMFC

There has been increasing demand for fresh and sustainable universal energy applications due to the quick development of proton-exchange membrane fuel cell technology. Fuel cell-based proton exchange membrane fuel cell (PEMFC) is amongst the most promising categories of fuel cells.[12-15] The PEMFC transforms the chemical energy liberated during the electrochemical reaction of hydrogen and oxygen to electrical energy, as opposed to the direct combustion of hydrogen and oxygen gases to produce thermal energy.

The schematic illustration of PEMFC is revealed in **Fig. 2.** The PEMFC consists of three main components such as membrane electrode assembly (MEAs), bipolar plates, and sealing materials. As shown in **Fig. 2**, the PEMFC cell has an assembly in which a membrane electrode assembly (MEA) is sandwiched between the bipolar plates (BPs) in which a gas flow path is formed. MEA consists of a polymer electrolyte membrane (polymer electrolyte membrane, PEM) such as Nafion®, which is a proton conductor, a catalyst layer (catalyst layer, CL) consisting of catalysts such as Pt and Pt-Ru, and carbon paper and carbon cloth. It is composed of a gas diffusion layer (GDL).[16,17] The PEMFC reaction consists of a hydrogen oxidation reaction of the anode electrode shown in the following equation (1) and an oxygen reduction reaction of the cathode pole shown in the equation (2).

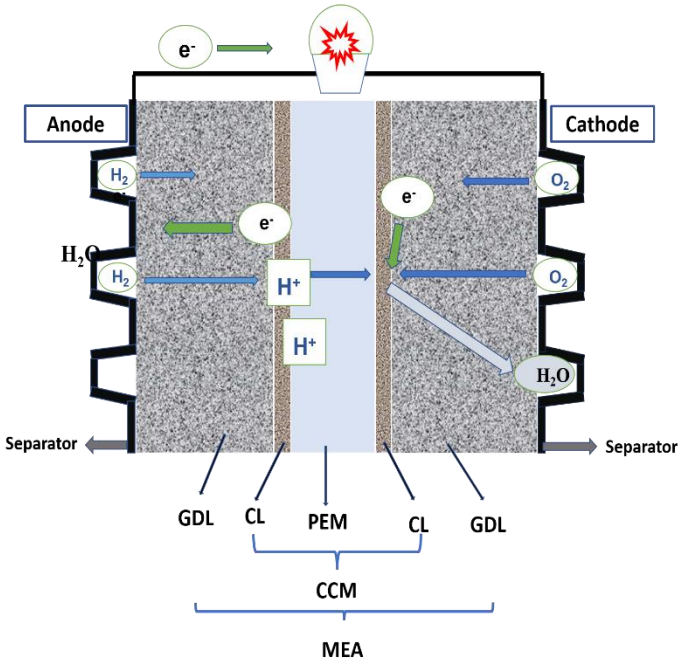

Where,

MEA: Membrane electrode assembly

PEM: Polymer electrolyte membrane

CL: Catalyst layer

GDL: Gas diffusion layer

CCM: Catalyst coated membrane

Fig. 2. Schematic diagram of PEMFC single cell.[18]

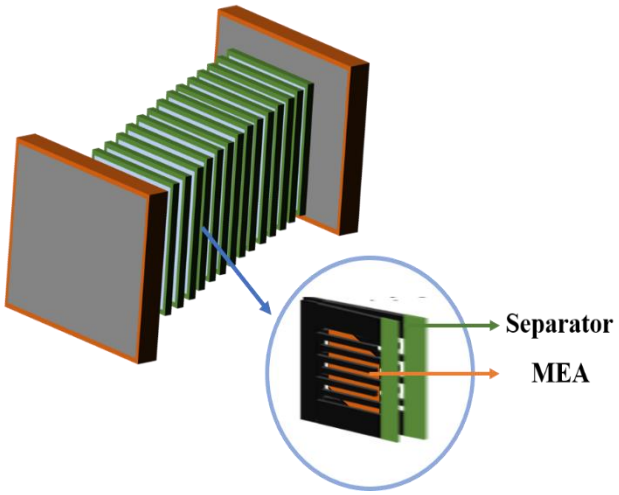

Fig. 3. Schematic diagram of PEMFC stack.

The oxidation half-cell or hydrogen oxidation reaction is represented by:

At the anode:

$$H_2 \longrightarrow 2H^+ + 2e^- \quad \ldots\ldots\ldots\ldots\ldots\ldots\ldots\ldots \quad (1)$$

At the cathode:

$$\tfrac{1}{2}\, O_2 + 2H^+ + 2e^- \longrightarrow H_2O \quad \ldots\ldots\ldots\ldots\ldots \quad (2)$$

Overall reaction:

$$H_2 + \tfrac{1}{2}\, O_2 \longrightarrow H_2O \quad \ldots\ldots\ldots\ldots\ldots\ldots \quad (3)$$

The cell potential is obtained by Nernst`s equation.

$$E^{\circ}_{\text{cell}} = -\frac{\Delta_r G^{\circ}}{nF}$$

Here, E°_{cell} = Cell potential, $\Delta_r G^{\circ}$ = Standard reaction Gibbs energy change and F = Faraday`s constant.

The theoretical cell potential at 298 K is, $E^{\circ}_{\text{cell}} = 1.229$ V and $\Delta_r G^{\circ} = -273.13$ kJ mol^{-1}.

Since the standard generated Gibbs energy change $\Delta G^{\circ} = -237$ kJ / mol at 298 K (25 °C) and n = 2 in Eq. (3), the theoretical standard battery potential is 1.23 V. However, when electricity is extracted from an actual battery, the cell voltage decreases with increasing current density due to a voltage loss called polarization or overvoltage.[19] Since the cell voltage per single cell is 0.65 to

0.75 V, in order to obtain a high voltage, a large number of cells are stacked to form a cell stack as shown in **Fig. 3**.

Therefore, it is used as an in-vehicle power supply. In this case, as shown in **Fig. 3**, several of these cells are stacked to form a stack. For example, the stack installed in Toyota Motor Corporation`s "MIRAI" has 370 cells, where, 740 separators are used to obtain the specified voltage.[20]

1-3 Characteristics and functions of bipolar plate

The bipolar plate is an equally significant component as a membrane-electrode assembly (MEA) in the PEMFC stack. The main action is summarized in **Table 1–2**.[21-22] Therefore, in high mechanical strength workable materials are required which is shown in **Table 1-3.** Therefore, the bipolar plate must have the following characteristics: [23]

(1) The bipolar plate is the framework of the whole PEMFC and provides the mechanical strength to support the MEA, so it is necessary to have sufficient strength. Meanwhile, in consideration of the improvement of power density, it is better to choose materials with higher specific strength;

(2) The surface of the bipolar plate needs the processing flow field as the channel of gas and water. Therefore, a good processing performance must be maintained;

(3) The bipolar plate has the function of collecting and conducting current, so it must be a good conductor;

(4) The bipolar plate needs to effectively segregate the oxidizer from the reducing agent to avoid the contact them, which requires the bipolar plate to have a low gas permeability;

(5) The electrolyte of PEMFC is an acidic medium, so the bipolar plate must possess good chemical and electrochemical corrosion resistance to improve service life;

Table 1-2. Role of bipolar plate.

- To support the electrode material
- To collect and conduct current
- To segregate oxidants and reducing agents
- Discharge of generated water and
- To guide the flow of oxidants and reducing agents on the inner surface of the electrode

Table 1-3. Requirements of bipolar plate.

- Including uniform gas distribution
- Low contact resistance and high electrical conductivity
- Mechanical strength
- Gas impermeable
- Cheap and
- Easy fabricating

The United States Department of Energy (DOE) is an inventor in developing technological goals for PEMFC and their related components. Bipolar plate technical indicators of PEMFC were proposed by the U.S. DOE, and displayed in **Table 1-4.** According to **Table 1-4**, many of the design targets for bipolar plate in 2020 and 2025, including anode and cathode corrosion, electrical conductivity, or areal specific resistance, have been already completed in 2015.[24, 25] However, some design parameters still need to be significantly improved. In particular, the cost should be reduced from 7 \$ kW^{-1} net in the current status to a requirement of 2 \$ kW^{-1} 1 net in 2025, which is one of the most challenging characteristics.[24-25]

Table 1-4. Bipolar plate technical indicators of PEMFC from the U.S. DOE.[22-23]

Characteristic	Units	2015 Status	2020 Status	2025 Target
Plate cost	$\$/kW^{-1}$	7	3	2
Plate weight	kg/kW^{-1}	<0.4	0.4	0.18
Plate H_2 permeation	$cm^3\,sec^{-1}\,cm^{-2}\,Pa^{-1}$	0	1.3×10^{-14}	2×10^{-6}
Corrosion anode	$\mu A/\,cm^2$	No active peak	<1 and no active peak	<1 and no active peak
Corrosion cathode	$\mu A/\,cm^2$	<0.1	<1	<1
Electrical conductivity	S/cm	>100	>100	>100

Areal specific resistance	Ohm cm^2	0.006	0.01	<0.01
Flexural strength	MPa	>34 (Carbon plate)	25	>40
Lifespan	hours	20-40	5000	8000

The BP candidate materials are roughly classified into carbon-based and metal-based materials.[26-33] As the separator material, a carbon-based material such as graphite,[34] and a metal-based metals such as aluminum,[35-37] stainless steel,[38-41] titanium,[42] and copper[43] and their alloys has been conducted. The chief advantages and drawbacks of carbon-based materials and metal-based materials, respectively[34, 42] are shown in **Table1-5**.

Table 1-5 Advantages and Disadvantages of Carbon and Metallic Materials.

Carbon based Materials

Advantages:

- High corrosion resistance
- Low density

Disadvantages:

- Low gas impermeability
- Low mechanical strength

Metal based Materials

Advantages:

- High gas impermeability
- High mechanical strength

Disadvantages:

- Low corrosion resistance
- High density

Yashiro H. et al. proposed a new type of bipolar plate in which the flow path forming material and the bottom plate (reaction gas isolation plate) are different which is shown in **Fig. 4**.

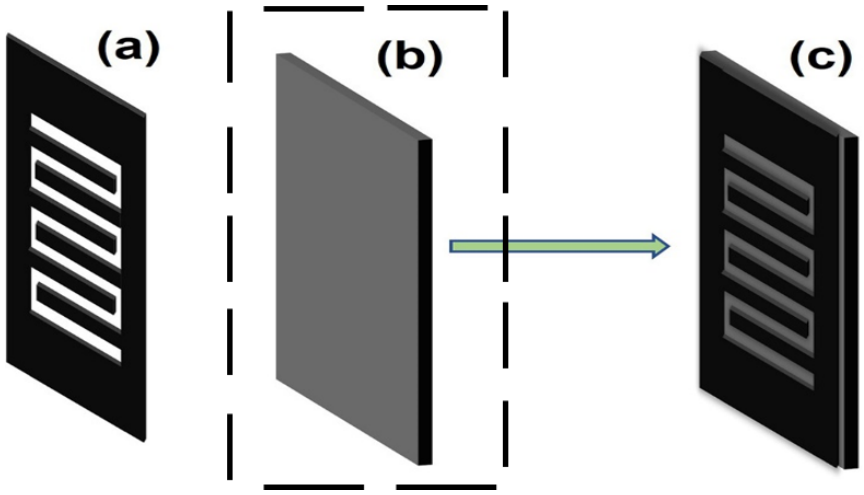

Fig. 4 (a) Flow path-forming plate inside the separator; (b) gas separator; and (c) bipolar plate assembly (configured separator).

The most extensively studied applicant stainless steels (SSs) have been verified and cast-off as BPs by numerous researchers,[43-48] who reported that corrosion expanse is slight and PEMFC output is steady even after 1000 h of operation.[49,50] But disastrously, it was thought that due to its massive weight, it could be a severe delinquent in light of transportation utilization. Along with these limitations, aluminum (Al) is regarded as one of the most promising materials for renewal functions, and some of its remarkable facilities include high electrical and fatigue resistance, high power, recyclability, thermal conductivity, low density, low price, and light heaviness.[51-54] It seems to be the Al BP maximum that diminishes 65% heaviness compared to the SS BPs. Al is susceptible to corrosion due to the creation of a durable oxide film on the surface of the bipolar plates.[55] Therefore, in this research, we will consider the application of Al as a reaction gas isolation plate with the aim of reducing the weight of the BP.

In simulated environments, previous studies have concerted on the corrosion features of Al in some dilute acidic solutions such as sulfuric acid, hydrochloric acid,[56,57] sulfuric acid with hydrogen fluoride media,[58] neutral dilute salt solutions for instance, halide media [59-60] and sodium sulfate with sodium fluoride solution.[61-62] It is known that the typical operating environment for PEMFC includes a pH value in the range of 3 to 6, which is weakly acidic, whereas BPs are typically handled on crevice corrosion by discharging major anions such as F^-, SO_4^{2-}, Cl^-, etc. from the perfluoro-sulfonic acid membrane, and the temperature can reach up to 80 °C.[63-65]

1-4 Objectives of this research work

Considering the use of metallic materials as the reaction gas isolation plate, it is necessary to investigate the corrosion behavior at the bottom of the flow path in the actual power generation environment, but in general, research on the corrosion of metal separators is based on contact with MEA. It is performed assuming a severely corroded environment such as a part (rib part). Since the bottom of the flow path does not come into direct contact with the MEA, it is expected that the corrosive environment will be milder than that of the rib part, and light metal materials such as Al, which are superior in terms of lightness compared to conventional metal-based materials, will be used. However, there is no example of investigating the corrosion behavior of light metal materials in the environment at the bottom of the flow path.

In addition, a PEMFC separator using a carbon-based material as the flow path forming material and Al as the reaction gas isolation plate was prototyped, and the corrosive environment at the bottom of the flow path was investigated through a power generation test to use it as a reaction gas isolation plate in this study.

Though several studies have been proposed based on the simulated conditions, it is considered that the cathodic and anodic solutions in the real environment are more rational and featured the PEMFC operating system. Thus, it is significantly needed to study the correlation of the corrosion behavior of Al between the solutions in simulated and real environments in PEMFC. That's why our research interest was to find out the corrosion behavior of Al in simulated and real environments for use as the bipolar plate in PEMFC. Therefore, in this study, a PEMFC BP using the carbon-based material as the flow path-forming material and Al as the reaction gas isolation plate was prototyped. Furthermore, the corrosive environment at the bottom of the flow path and the useability of Al as a reaction isolation plate were investigated through the power generation tests.

References

1. Z. Sharaf, M. F. Orhan, *Renew. Sust. Energ. Rev.* **32**, 810−853 (2014).
2. D. R. Dekel, *J. Power Sources* **375**, 158−169 (2018)
3. W. E. Mustain, P. A. Kohl, *Nat. Energy* **5**, 359−360 (2020).

4. M. R. Kraglund, M. Carmo, G. Schiller, S. A. Ansar, D. Aili, E. Christensen, J. O. Jensen, *Energy Environ. Sci.* **12**, 3313−3318 (2019).
5. K. H. Hou, C. H. Lin, M. D. Ger, S.W. Shiah and H. M. Chou, *J. Green Energy* **9**(1), 71–83 (2012).
6. K. Sopian, W. R. Daud, *Renew. Energy* **31**(5), 719–727 (2006).
7. D. G. Lopes, E. P. da Silva, C.S. Pinto, N. P. N. Jr, J.C. Camargo, P. F. P. Ferreira, A. L. Furlan, *Renew. Energy* **45**, 205–212 (2012).
8. G. Hoogers, Fuel Cell Technology Handbook; CRC Press: Florida, USA, 2003.
9. A. Barjola, J. L. Reyes-Rodríguez, O. Solorza-Feria, E. Giménez, V. Compañ, *Ind. Eng. Chem. Res.* **60**, 9107–9118 (2021).
10. Y. Wang, D. F. Ruiz Diaz, K. S. Chen, Z. Wang, X. C. Adroher, *Mater. Today* **32**, 178–203 (2020).
11. Hydrogen and Fuel Cell Strategy Council. `The Strategic Road Map for Hydrogen and Fuel Cells`, March 12, 2019.
12. B. -T. Tsai, C. -J. Tseng, Z. -S. Liu, C. -H. Wang, C. -I. Lee, C.-C. Yang, S. -K. Lo, *Int. J. Hydrogen Energy* **37**, 13060–13066 (2012).
13. H. Heidary, M. J. Kermani, B. Dabir, *Energy Convers. Manag.* **124**, 51–60 (2016).
14. M. Zhiani, S. Kamali, S. Majidi, *Int. J. Hydrogen Energy* **41**, 1112–1119 (2016).
15. M. Zhiani, S. Majidi, M. M. Taghiabadi. *Fuel Cells* **13**(5), 946–955 (2013).
16. K. Yoshida, R. Okada, *Honda R & D Technical Review* **30**, 2 (2018).
17. Y. Wang, D. F. R. Diaz, K. S. Chen, Z. Wang, X. C. Adroher, *Mater. Today* **32**, 178–203 (2020).
18. K. Yoshito, K. Ken. G. Akihito, K. Taisuke, *Honda R & D Technical Review* **29**, 2 (2017).
19. H. Uchida, H. Ikeda, I. Chiaki, T. Yoshio, Functional Chemistry Series of Electrons and Ions, Vol. 4 `All about solid polymer fuel cells `, NTS, (2003).
20. H. Yanagimoto, *Surface Technology* **71**, 17–20 (2020).
21. S. Karimi, N. Fraser, B. Roberts, F. R. Foulkes, *Mater Sci Eng.* **20**, 1–22 (2012).
22. A. Hermann, T. Chaudhuri, P. Spagnol, *Int J Hydrogen Energy* **30**, 1297–302 (2005).
23. R. Taherian, *Journal of Power Sources* **265**, 370-390 (2014).
24. DOE. Fuel cell technologies office multi-year research, development, and demonstration (MYRD & D) plan. Washington, D.C: U.S. Department of Energy; 2013.

25. Y. X. Song, C. Z. Zhang, C. Y. Ling, M. Han, R. Y. Yong, D. Sun, et al, *Int J Hydrogen Energy* **45**, 29832–47 (2020).
26. H. Tawfik, Y. Hung, D. Mahajan, *J Power Sources* **163**, 755–767 (2007).
27. S. S. Dihrab, K. Sopian, M. A. Alghoul, M. Y. Sulaiman, *Renew Sustain Energy Rev*. **13**, 1663–1668 (2009).
28. R. A. Antunes, M. C. L. De Oliveira, G. Ett, V. Ett, *J Power Sources* **196**, 2945–2961 (2011).
29. S. Karimi, N. Fraser, B. Roberts, F. R. Foulkes. *Ann Mater Sci Eng* **2012**, 1–22 (2012).
30. M. C. L. De Oliveira, G. Ett, R. A. Antunes, *J Power Sources* **206**, 3–13 (2012).
31. R. Taherian, *J Power Sources* **265**, 370–390, (2014).
32. A. Iwan, M. Malinowski, G. Pasciak, *Renew Sustain Energy Rev*. **49**, 954–967 (2015).
33. D. Y. Li, Y. X. Shi, H. P. Xu, Y. Chen, P. Zhou, X. W. Li, W. X. Feng, S. P. Wang, *Int. J. Electrochem. Sci.* **13**, 9346–9358 (2018).
34. X. Yan, M. Hou., H. Zhang, F. Jing, P. Ming, B. Yi, *J. Power Sources* **160**(1), 252–257 (2006).
35. C. Alegre, L. Álvarez-Manuel, R. Mustata, L. Valiño, A. Lozano, F. Barreras, *Int. J. Hydrogen Energy* **44**, 25,12748–12759 (2019).
36. C. Lin, S. Tsai, *Applied Energy* **100**, 87–92 (2012).
37. A. G. González-Gutiérrez, M. A. Pech-Canul, G. Chan-Rosado, P. J. Sebastian, *Fuel* **235**, 1361-1367 (2019).
38. C. K. Jin, K. H. Lee, C.G. Kang, *Int. J. Hydrogen Energy* **40**(20), 6681–6688 (2015).
39. M. Dadfar, M. Salehi, M. A. Golozar, S. Trasatti, M. P. Casaletto, *Int. J. Hydrogen Energy* **42**, 41, 25869–25876 (2017).
40. B. Mi, Z. Chen, Q. Wang, Y. Li, Z. Qin, H. Wang, *Int. J. Hydrogen Energy* **46**(64), 32645–32654 (2021).
41. Y. Leng, P. Ming, D. Yang, C. Zhang, *J. Power Sources* **451**, 227783 (2020).
42. J. Shi, P. Zhang, Y. Han, H. Wang, X. Wang, Y. Yu, J. Sun, *Int. J. Hydrogen Energy* **45**(16), 10050–10058 (2020).
43. V. V. Nikam, R.G. Reddy, *Electrochimica Acta* **51(**28), 6338–6345 (2006).
44. R. C. Makkus, A. H. H Janssen, F. A. de Bruijn, R. K. A. M. Mallant, *J. Power Sources* **86**, 274 (2000).

45. D. P. Davies, P. L. Adcock, M. Turpin, S. J. Rowen, *J. Power Sources* **86**, 237–242 (2000).
46. D. P. Davies, P. L. Adcock, M. Turpin, S. J. Rowen, *J. Appl. Electrochem.* **30**, 101–105 (2000).
47. K. Iversen, *Corros. Sci.* **48,** 1036–1058 (2006).
48. M. Kumagai, S. -T. Myung, Y. Katada, H. Yashiro, *Electrochim. Acta* **211**, 754−760 (2016).
49. H. Yashiro, R. Asaishi, S. Kuwata, M. Kumagai, A. Yao, *Trans. Mater. Res. Soc. Jpn*. **32**, 963–966 (2007).
50. M. Kumagai, S. -T. Myung, S. Kuwata, R. Asaishi, H. Yashiro, *Electrochim. Acta* **53**, 4205–4212 (2008).
51. D. Y. Li, Y. X. Shi, H. P. Xu, Y. Chen, P. Zhou, X. W. Li, W. X. Feng, S. P. Wang, *Int. J. Electrochem. Sci.* **13**, 9346–9358 (2018).
52. S. Caporali, S. Fossati, A. Lavacchi, I. Perissi, A. Tolstogouzov, U. Bardi, *Corros. Sci.* **50**, 534–539 (2008).
53. H. Fang, K. Chen, Z. Zhang, C. Zhu, *Trans. Nonferrous Met. Soc. China* **18**, 28–32 (2008).
54. R. Rosaliza, W. B. W. Nik, H. B. Senin, *Mater., Chem. Phys.* **107,** 281–288 (2008).
55. V. Mountarlier, M. P. Gigander, B. Normand, J. Pagetti, *J. Corros. Sci*. **47**, 937–951 (2005).
56. J. P. Dasquet, D. Caillard, E. Conforto, *Thin Solid Films* **371**, 183–190 (2000).
57. I. V. Aoki, M. C. Bernard, C. D. Torresi, *Electrochim. Acta* **46,** 1871–1878 (2001).
58. A. Jahan, M. A. Alam, S. Yonezawa, E. Suzuki, H. Yashiro, *ECS trans.* **102**, 45–54 (2021).
59. Z. Bo, L. Ying, F. Wang, *Corros. Sci.* **51** 268 (2009).
60. E. Mccafferty, *Corros. Sci.* **45**, 1421 (2009).
61. M. A. Alam, A. Jahan, S. Yonezawa, E. Suzuki, H. Yashiro, *ECS trans.* **108**, 131–141 (2022).
62. M. A. Alam, A. Jahan, E. Suzuki, H. Yashiro, *ChemistrySelect* **8**, 02300379 (2023).
63. A. Agneaux, M. H. Plouzennec, L. Antoni, J. Granier, *Fuel Cells* **6,** 47-53 (2006).
64. R. L. Borup, N. E. Wanderborgh, *Mater. Res. Soc. Symp. Proc.* **393**, 151–155 (1995).
65. M. C. Li, C. L. Zeng, S. Z. Luo, J. N. Shen, H. C. Lin, C. N. Cao, *Electrochim. Acta* **48**, 1735–1741 (2003).

Chapter 2

Investigation of Corrosion Performance of Aluminum as Bipolar Plate in PEMFC Environment

Chapter 2: Investigation of Corrosion Performance of Aluminum as Bipolar Plate in PEMFC Environment

2-1 Introduction

Fuel cells have recently been developed as devices, which convert chemical energy into electric energy directly. For the time being, they can be a solution for serious concerns such as the shortage in fossil fuel resources and crises in environmental pollution. Proton exchange membrane fuel cell (PEMFC) is among the most promising types of fuel cells for many advantages such as high-power density, high efficiency, first start up, low operating temperature (< 100 °C), noiselessness.[1-13] Bipolar plate (BP) is an important multifunctional component in polymer electrolyte membrane fuel cells (PEMFCs) system[14,15] which should possess some specifications such as superior electrical and thermal conductivity, high corrosion resistance, good mechanical performance, and low cost.[16] Also, the BP can fasten the component of PEMFC stack, supply fuel and air, provide water and heat flow, collect current, electricity and prevent leakage of electrolyte.[17-20]

The BP candidate materials are roughly classified into carbon-based and metal-based materials. [21-28] Carbon-based materials are lightweight and have excellent corrosion resistance, but are inferior to metal-based materials in terms of gas shielding properties and mechanical strength. Metallic materials have the opposite characteristics, and corrosion resistance is a particular and important issue. Aluminum (Al) is considered to be one of most promising material for transformation applications for its special qualities of low density, low cost and light weight.[29] Earlier, it was proposed that the PEMFC BP can be divided into two parts: gas isolation plate and flow path forming material which is shown in **Fig. 1.**[30] Normally, metallic BPs are corroded exclusively at the rib part where BP contacts with the gas diffusion layer (GDL), while there is not much corrosion at the bottom of the flow path. Therefore, the corrosion resistance required for the reaction gas isolation plate would not be as high as required for the flow path forming material. In our previous studies, some techniques were followed to check and reduce the corrosion resistance of Al used as bipolar plate in PEMFC in different conditions.[31-33] Yet some study for modification and surface treatment is required to evaluate the Al based materials for use as bipolar plate in PEMFC. That`s why, in this study, a composite BP using Al alloy such as A1060 as the reaction gas isolation plate and carbon-based materials as the flow path forming materials was fabricated

to investigate the corrosion behavior of A1060 as the reaction gas isolation plate through power generation test.

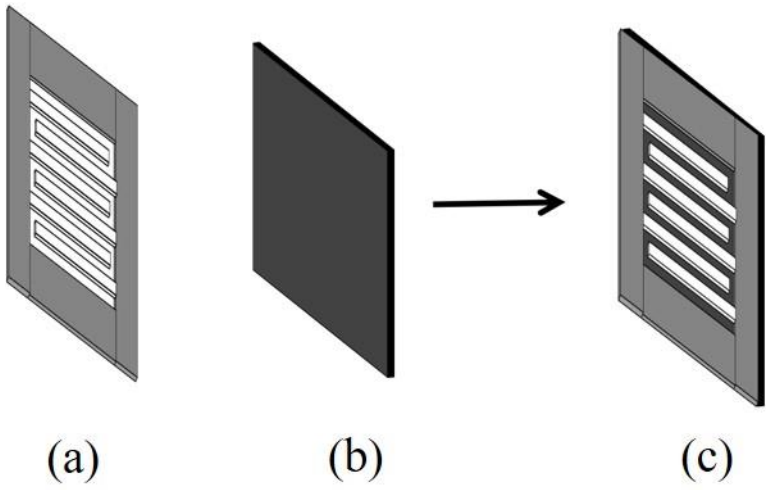

Fig. 1 (a) Graphite as channel former (b) Graphite, TiN-SBR coated A1060 and Bare A1060 as gas isolation plates and (c) Bipolar plate assembly.

2-2 Experimental Section

2-2-1 Corrosion test in simulated environment

2-2-1-1 Exposure test in humid air

In order to simulate an environment in which only gas exists in the PEMFC cell flow path, an exposure test of in moist air was conducted using a device shown in **Fig. 2**. The commercial-type of Al alloy (A1060) plates was cut into specimens of having size of 40 × 15 × 5 mm^3 (shown in **Fig. 4**) which were electropolished[34,35] under the conditions of **Table 1**. The ultrapure water (18.2 MΩ cm @ 273 K) was used as the test solution. Ultrapure water was placed in a flask at 348 K and the test piece was hung on the upper part of the device for 24 hours. The temperature of the upper part of the device was maintained at 353 K (80 ° C) using a heating mantle. The saturated water vapor pressure at 348 K was 38.58 kPa.

2-2-1-2 Immersion test in pure water

In order to simulate the environment where liquid water exists in the PEMFC cell flow path, a dipping test of A1060 in pure water was performed using a device as shown in **Fig. 3**. As in the

exposure test, A1060 was electropolished under the conditions of **Table 2-2** which was used as the test piece and ultrapure water was used as the test solution. The test piece was immersed in a Teflon container containing ultrapure water and kept in a constant temperature at 353 K (80 ° C) for 24 hours.

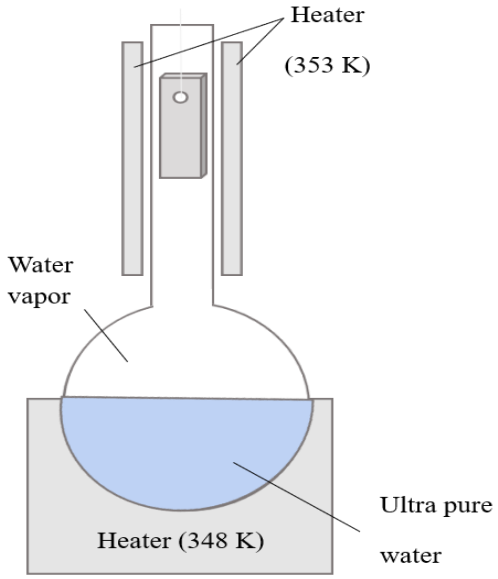

Fig. 2 Schematic diagram of exposure test in humid air.

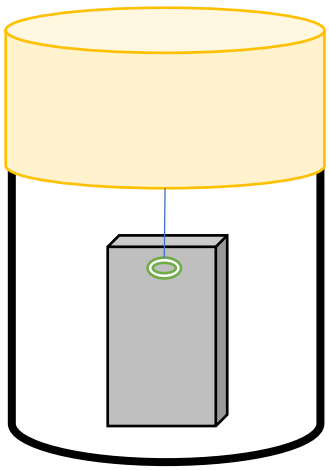

Fig. 3 Schematic diagram of experimental cell for the immersion test.

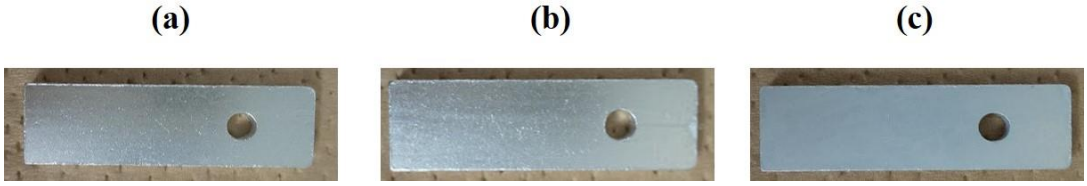

Fig. 4 The appearance of A1060 specimens (a) before exposer, (b) after exposure in humid air and (c) after exposure in distilled water.

Table 1. Condition used for electropolishing of A1060.

Chemicals	H_3PO_4 : H_2SO_4 = 10:1
Temperature	333 K (60℃)
Density	0.4 A dm^{-2}
Time	10 min

2-2-2 Single cell power generation test.

The A1060 (80 mm × 80 mm × 2 mm) and graphite (80 mm × 80 mm × 5 mm) were machined into BPs using serpentine flow field bestowed by NEDO and reported by the Japan Automobile Research Institute (JARI)[36] and used for the single cell power generation test as the reaction gas isolating plate. The reaction gas isolating plates were electropolished under the condition shown in **Table 1**. The single cell power generation test was accomplished using the fuel cell (FC) evaluation test equipment (FC5100 series, CHINO) shown in **Fig. 5** using a Japan Automobile Research Institute (JARI) standard cell incorporating various BPs.[36] Commercially available membrane electrode assembly (MEA) with an appealing carbon paper gas diffusion layer (GDL) was used with the compressive power of 200 N cm^{-2} measured by a torque wrench. MEA was prepared by superimposing GDL (SIGRACET® 28BC, SGL Carbon) on the catalyst layers on both sides of a commercially available catalyst-coated membrane (CCM) and hot pressing. Before the single cell test, a load of 1.0 A cm^{-2} was applied to activate the electrodes for about 1 day. The single cell test conditions are exposed in **Table 2**.

Fig. 5 Appearance of fuel cell evaluation test equipment (FC5100 series, CHINO).

Table 2. Single cell test conditions

Anode (H_2) flow rate	125 cm^3 min^{-1}
Cathode (O_2) flow rate	520 cm^3 min^{-1}
Cell temperature	348 K (75 ℃)
Humidification Temp.	343 K (70 ℃)
Activation area	5 cm × 5 cm
Load current density	1.0 A cm^{-2}
Applied pressure	1.5 MPa

2-2-3 AC impedance measurement.

After the *i-V* measurement and during the single cell power generation test, an AC impedance measurement device (FC-200F, CHINO) was used to measure the AC impedance in the power generation state. The measurement was performed under the conditions of a superimposed current of 100 mA (4 mA cm^{-2}), frequency range of 0.1 Hz to 15000 Hz, frequency sweep direction of high to low, and a division number of 20 steps per decade.

2-2-4 TiN-SBR coating process.

TiN-SBR was applied using the spray method to the surfaces of the A1060 plate and the graphite current collector plate, which had been electropolished under the condition of **Table 1**. TiN particles (Japan New Metals Co. Ltd.) with a particle size of 0.8 μm were used as the main coating material, and water dispersed with 40% styrene butadiene rubber (SBR) (BM400B, Nippon Zeon) was diluted to 6.7% with distilled water to make a binder. Distilled water and 2-propanol were used as dispersion medium. The TiN-SBR ink was mixed at a composition ratio shown in **Table 3** and dispersed by ultrasonic waves for around 10 minutes to obtain a turbid liquid. Using a spray coating device, TiN-SBR ink was spread to 80 mm × 80 mm of A1060 plate or graphite current collector fixed on a hot plate heated to 90 ℃. Subsequently, the TiN-SBR layer was adhered by drying for 90 seconds in an oven heated to 180 ℃.

Table 3. TiN-SBR ink composition (mass %)

TiN	6.7% SBR	2-propanol	Distilled water
1.0	2.25	67.7	29.0

2-2-5 Surface morphology analysis

After the corrosion tests and single cell operations, the surfaces of Al060 specimens and gas separator plates were analyzed by optical microscope and scanning electron microscope (SEM) and the elemental analyses were done by energy dispersive X-ray (EDX) spectroscopy using FE-SEM (JSM-7800F). An accelerating voltage of 10 kV and 10.00 mm of working distance were maintained at the time of taking SEM and EDX.

2-2-6 Transmission electron microscopy (TEM)

After the cell operation for 500 h the test pieces and the cell were disassembled and the bipolar plate in cathode and anode side were cut to an appropriate size for TEM observation. The sample were prepared using a focused ion beam (FIB) and loaded on a copper mesh, and processed as thin as possible by Ga+ ion beam at an acceleration voltage of 30 kV. The specimens after the corrosion tests were also analyzed in cross section.

2-3 Results and Discussion

2-3-1 Microscopic images after the corrosion test

At first, one as polished A1060 was immersed in distilled water (DSW) for 24 hours at 353K. The other was exposed at 353K to humid air saturated at 348K for 24 h. As a result of the immersion test, the white corrosion products were formed on the A1060 surfaces after the immersion in distilled water. On the other hand, it remained glossy when A1060 was exposed to humid air which is shown in **Fig. 6.**

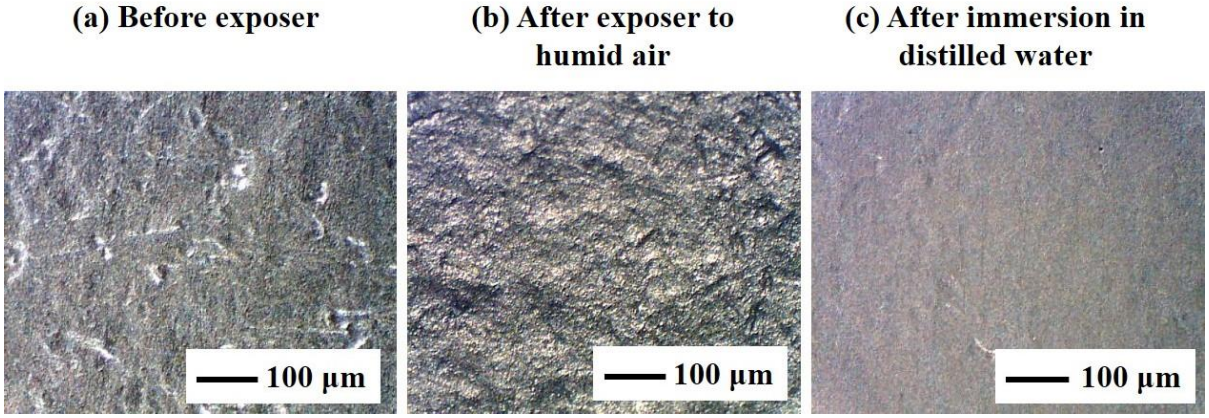

Fig. 6. Microscopic images of the test specimens (a) before and (b) after exposure to humid air and (c) after immersion into distilled water for 24h at 353K.

2-3-2 Fuel Cell Performance.

To study the effect of the gas isolating plate material on the cell performance, a single cell was operated using A1060 gas isolating plate. The A1060 was used as the reaction gas isolating plate with or without TiN-SBR coating. The results are shown in **Fig. 7.** When uncoated A1060 was used as the reaction gas isolating plate, the cell voltage was lower than that of graphite. It is

attributed that the contact electrical resistance was higher due to well-known passive layer formation between the A1060 reaction gas isolating plate and the glassy carbon channel former. But after being TiN-SBR coated, the cell performance was improved compared to the case of using untreated A1060, and the performance was close to that of using a full graphite BP. Thus, it can be suggested that A1060 can be used as a reaction gas isolating plate with no significant problem, at least in terms of cell performance.

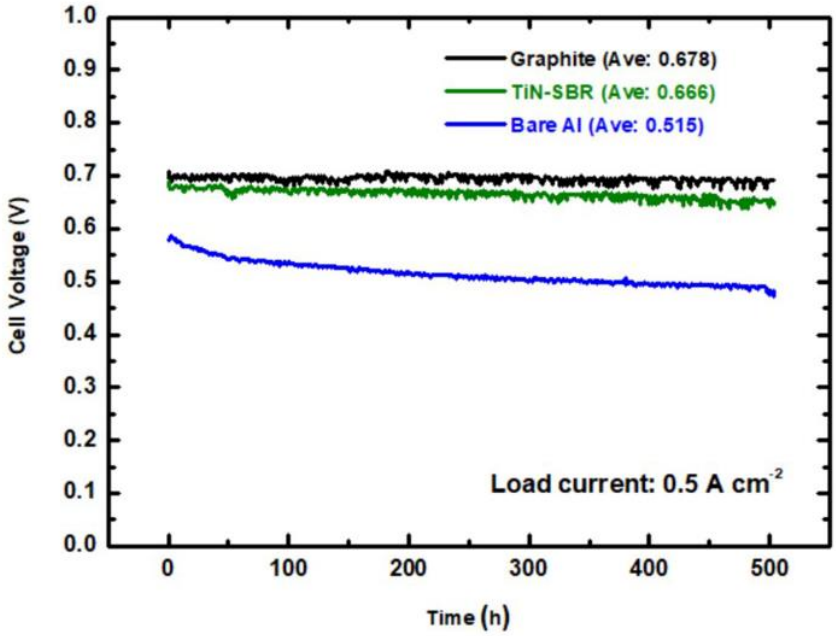

Fig. 7 Single cell power generation test using a full graphite BP and composite BPs adopting A1060 as the reaction gas isolating plate with and without TiN-SBR coating.

For the performance comparison, *i-V* curve characteristics before and after 500 h of single cell power generation test of using three types of BPs such as graphite, bare Al (A1060) and TiN-SBR-treated A1060 reaction gas isolating plates was measured which is shown in **Fig. 8.** The initial cell voltage versus current density curves is presented in **Fig. 8**(a). It can be seen here that the initial cell voltage of graphite and TiN-SBR coated BP were 0.58 V and 0.52 V, respectively at 0.5 A cm^{-2}. On the other hand, for graphite-glassy carbon composite engaging or bare A1060 as BP, the initial cell voltage was around 0.42 V at 1 A cm^{-2} which is being lower than that of the graphite cell. From the *i-V* curve changed over time, the cell performance was improved for TiN-SBR coated A1060 compared to the case of using untreated A1060, and the performance was close to

that of using graphite. **Fig. 8**(b) depicts the final state (after 500 h of single cell power generation test) current density versus voltage curve which is almost same as initial state. This proves that the *i-V* curve and the graph changed over time, the cell performance was improved for TiN-SBR coated A1060 compared to the case of using untreated or bare A1060. Thus, the high *i–V* performance of the TiN-SBR coated BPs illustrated their suitability for PEMFC.

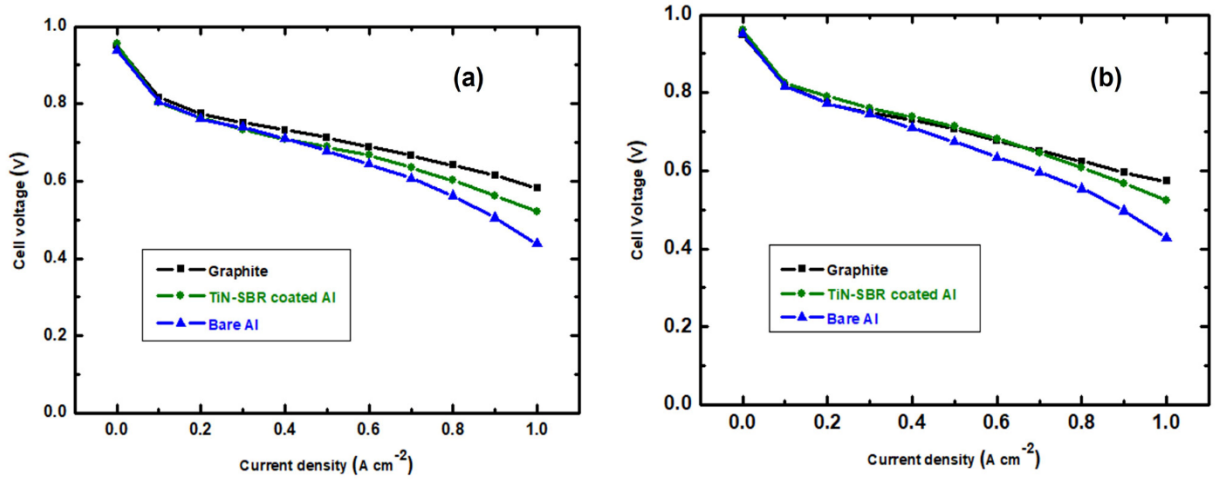

Fig. 8 *i–V* performance curves of the fuel cell using a full graphite BP and component BPs adopting A1060 as the reaction gas isolating plate with and without TiN-SBR coating: (a) initial state, and (b) final state.

2-3-3 Impedance data analysis.

We have also evaluated the change in AC impedance initially and during the long-term single cell power generation test that were assembled with the BPs of graphite, and A1060 as the reaction gas isolating plate and glassy carbon as the channel former which was conducted in a testing environment of 0.6 V and 80 °C. **Fig. 9**(a) shows the results of AC impedance measurement performed at a load current density of 1.0 A cm^{-2} after *i-V* measurement in a single cell using pure graphite and A1060 as a reaction gas isolating plate. Since the size of the arc in case of A1060 is almost the same as that in case of graphite, it is considered that there is not much difference between R_{ct} and R_{diff}, but R_{cont} is considered to be larger than in case of graphite since the arc in case of A1060 is shifted in the positive direction of the real axis. This difference in resistance is considered to be due to the fact that the contact resistance between A1060 and glassy carbon is larger than that of between graphite and glassy carbon.

The variation over time from 0 h to 96 h for A1060 gas isolating plate is shown in **Fig. 9**(b) where the reaction resistance and diffusion resistance increased over time. In addition, the contact resistance of the composite BP was higher. Thus, it is thought that the low cell potential of the composite BP was due to the high contact resistance. It is mentioned that, the shift of the arch in the positive direction of the real axis is considered to be the increase of contact resistance with the channel former due to the growth of the film formed on the surface of Al,[37] and the change in the shift width was due to the change in the film. From the perspective of generating power from a single cell using A1060 as a BP, although the cell potential was not as high as that of a graphite BP, we were succeeded in generating power continuously for 500 hours using the A1060 gas isolating plate.

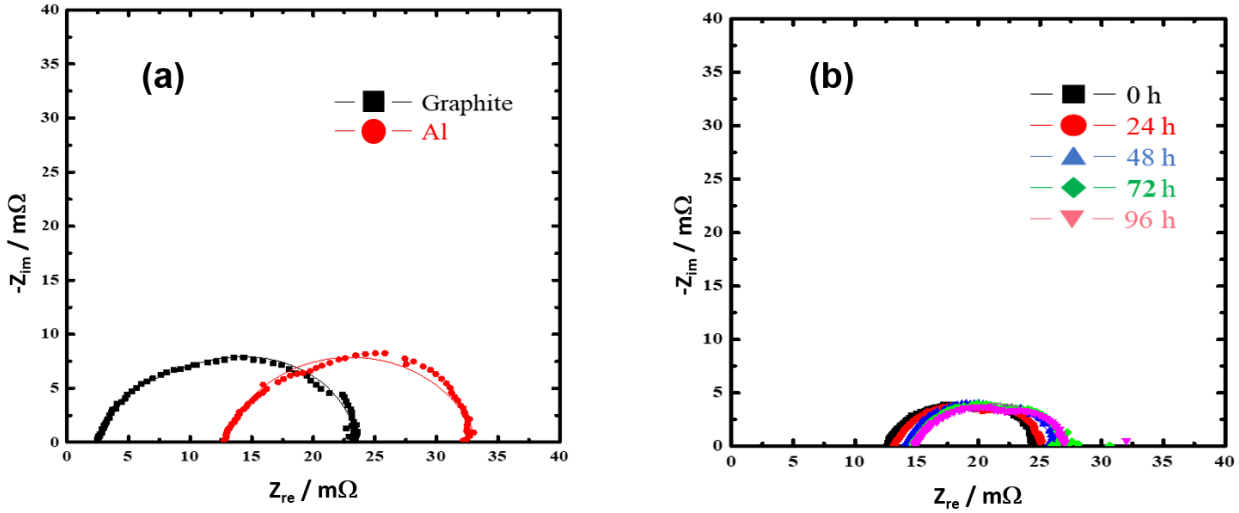

Fig. 9 Impedance behavior changes of the single cell power generation test using (a) graphite, and A1060 as the reaction gas isolating plate at the time of starting of power generation and (b) in different times such as 0, 24, 48, 72 and 96 h for A1060 gas isolating plate.

The electrical equivalent circuit to illustrate the impedance data for interpreting the results; in fact, other researchers have used similar circuits is shown in **Fig. 10**.[38] In this model, R_{cont} represents contact resistance, R_{ct} represents charge-transfer resistance of the cathode reaction, R_{diff} is the mass transfer resistance on the cathode side and constant phase element or CPE shows non-ideal capacitive behavior. It is assumed that constant phase elements exist in parallel in these resistance components. It can be seen that the membrane resistance was contained in R_{cont}, but it is considered that the contact resistance is dominant under the experimental conditions in this study.

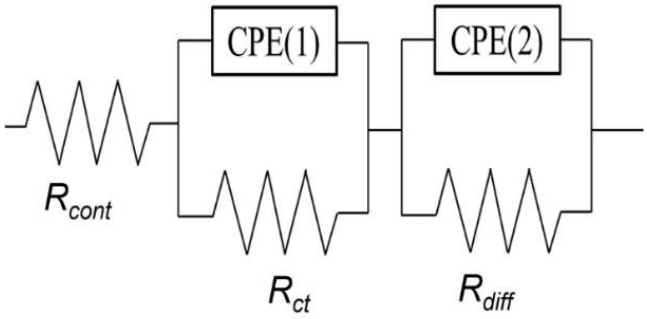

Fig. 10 Prospective equivalent circuit used for fitting the experimental data.

2-3-4 Cathode and Anode Side after Single Cell Power Generation Test.

In addition to the above discussion, we tried to evaluate the appearances of the A1060 reaction gas isolating plate on the cathode and anode sides before and after 500 h of single cell power generation test in order to get more clear data about the corrosion behavior of A1060 BPs used in PEMFC.

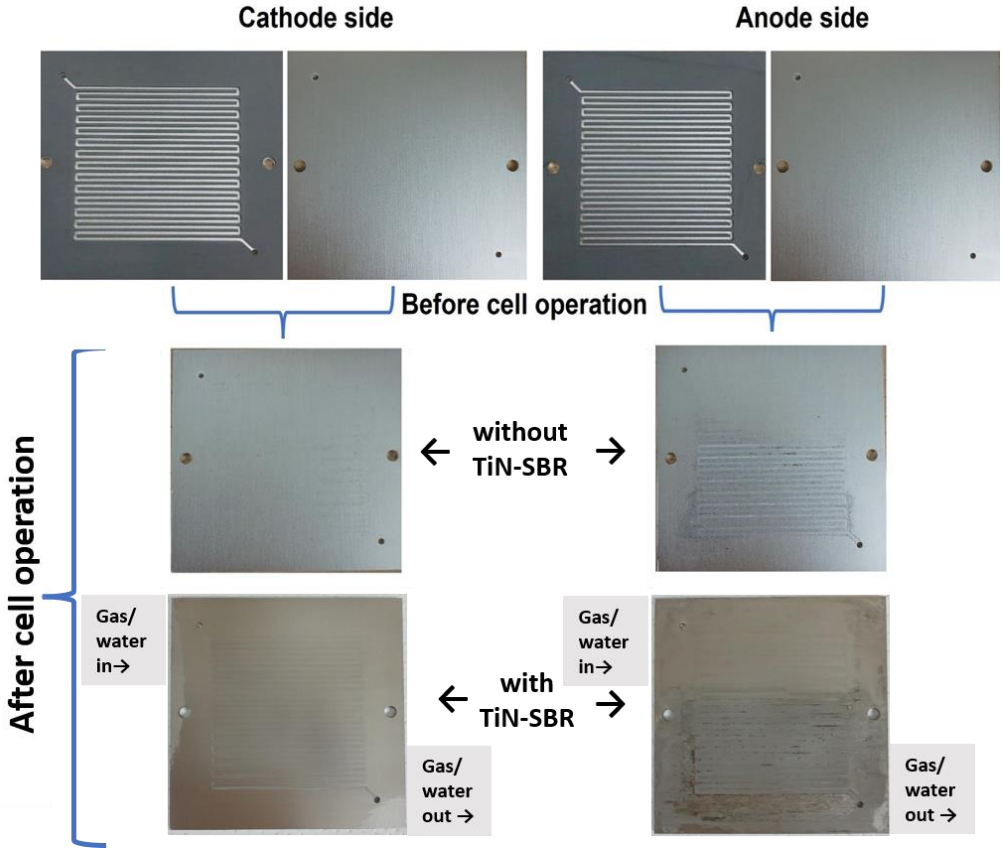

Fig. 11 Appearances of the cathode and anode sides of the gas isolating plates (A1060) before and after 500 h of single cell power generation test.

2-3-5 Cathode and Anode Side after Single Cell Power Generation Test using SEM and EDX.

The appearances of the A1060 reaction gas isolating plate on the cathode and anode sides before and after 500 h of single cell power generation test which is shown in **Fig. 11**. From the images, it was clearly seen on the cathode side that the gas isolating plate maintained its metallic luster, and no thick film was observed before and after the single cell power generation test. On the contrary, in the case of anode side, the A1060 gas isolating plate maintained its luster near the gas inlet side but turned white along the flow path from the central part to the gas outlet side. Since the reaction gas isolating plate has a part of the flow path through which gas and water flowed and a part that overlapps with the glassy carbon channel former, each was observed by SEM images and EDX analysis. From the appearance of the gas isolating plate, there was no significant difference observed depending on the change of position. So the SEM images of the central part of the cathode side were also taken and observed for further study which is shown in **Fig. 12**. **Fig. 13** shows the elemental EDX mapping composition for the cathode side and detecteed the distribution compositions as aluminum (Al), carbon (C), and oxygen (O). Neither SEM images nor EDX elemental mapping showed any mentionable corrosion products between the flow path part and the overlapped part, though a trace amount was observed due to the electrolytic polishing that was performed as pretreatment of the BP.

Similar to the cathode side, the overlapped part of the flow path part and the channel former were evaluated by SEM and EDX analysis. The gas inlet side that maintained the gloss and the central part where the whitening part was observed. **Fig. 12** represents the SEM images that reveal the whitening part on the anode side along the flow path from the central part to the gas outlet side. In

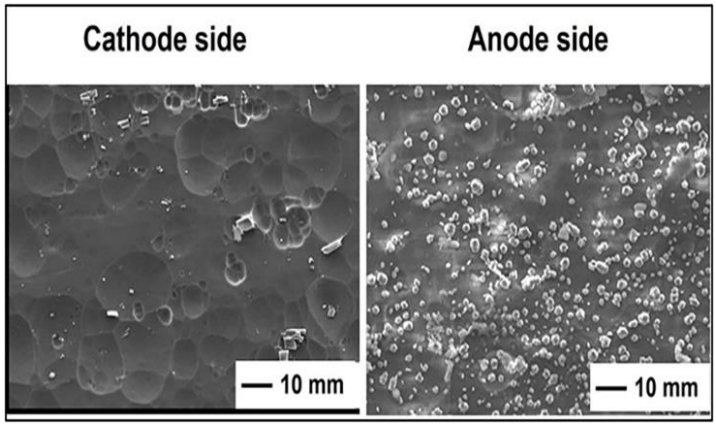

Fig. 12 SEM images of A1060 reaction gas isolating plate on the cathode and anode sides after 500 h of single cell power generation test.

addition, the corrosion products were found throughout the flow path at the whitening parts, and granular corrosion products as particles of different sizes were observed. Futhermore, **Fig. 13** shows the elemental mappings that confirmed the presence of the elemental compositions Al, C, and O. Therefore, it was assumed that the cathode side was in an environment where only gas was present during the single cell power generation test.

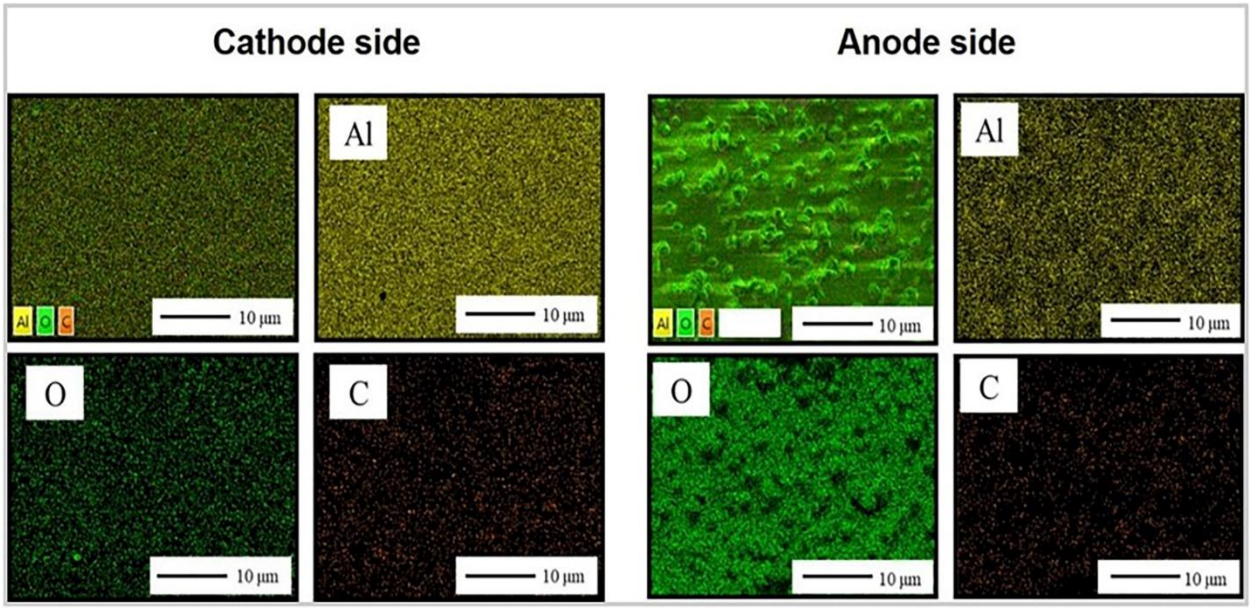

Fig. 13 EDX elemental mapping of the flow path of the cathode side reaction gas isolating plate on the cathode (superposition part) and anode sides after 500 h of single cell power generation test.

2-3-6 TEM analyses

The TEM images were taken to investigate the thickness of the film on the surface of the Al gas isolation plate after the single cell operation and A1060 alloy after immersion in water. **Fig. 14** shows that a thin oxide film with thickness around 50 nm was found on the cathode side **Fig. 14**(a), but a thick oxide film with thickness of 1.1 μm were observed in the whitening part on the anode side (b), and the film thickness was 1.2 μm after immersion in distilled water for 24 hours at 353K (c). It was found that the film on the anode side whitening part is similar to that of Al immersed in distilled water. Moreover, the thin oxide layer found on the cathodic side was similar to that found on Al after exposure to humid air. It is probable that the cathode-side reaction gas isolating plate inside was not in a state of being immersed in liquid water for a long time. It is considered that the bottom of the flow path on the cathode side was an environment which was only exposed to humid

gas. On the contrary, for the anode side, a thickness film was observed. These films were considered to be pseudo-boehmite hydrated oxide films. It is mentioned that the pseudoboehmite is recognized as alumina monohydrate, where boehmite is non-toxic, tasteless, odorless, white colloid (wet product) or powder (dry) with high crystal phase purity, good peptization performance, strong adhesion, high specific surface, large pore volume, etc.

Thus, it is considered that the white spots on the reaction gas isolating plate on the anode side were in a state of being immersed in liquid water during the single cell power generation test.

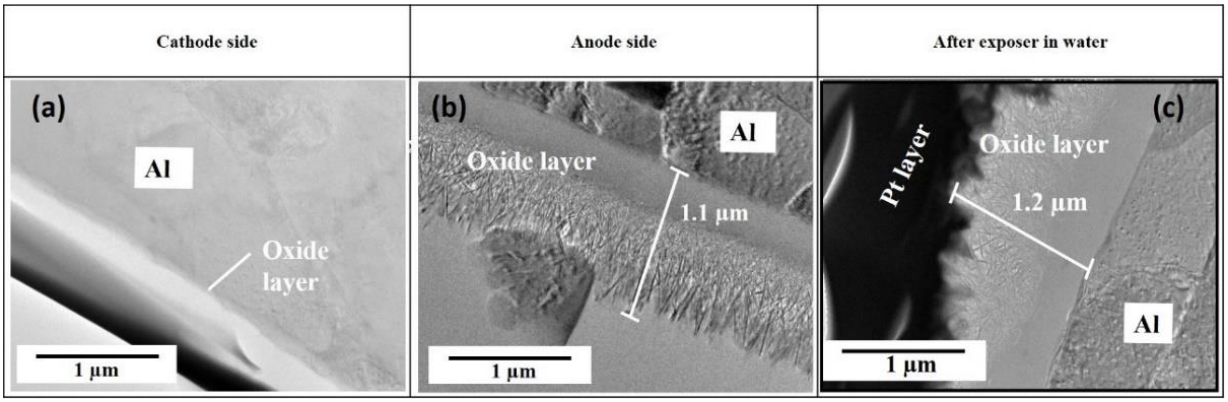

Fig. 14. Cross-sectional TEM images of A1060 reaction gas isolation plate on the (a) cathode and (b) anode side after 500 h of cell operation and (c) A1060 after exposure in distilled water for 24 h at 353K.

2-3-7 Corrosion behavior of Al reaction gas isolation plate treated with TiN-SBR.

The cross-sectional TEM images of a reaction gas isolation plate treated with TiN-SBR coating on the cathode and anode side after a 500-hour power generation test are shown in **Fig. 15**. No corrosion products could be confirmed in both cathode and anode side.

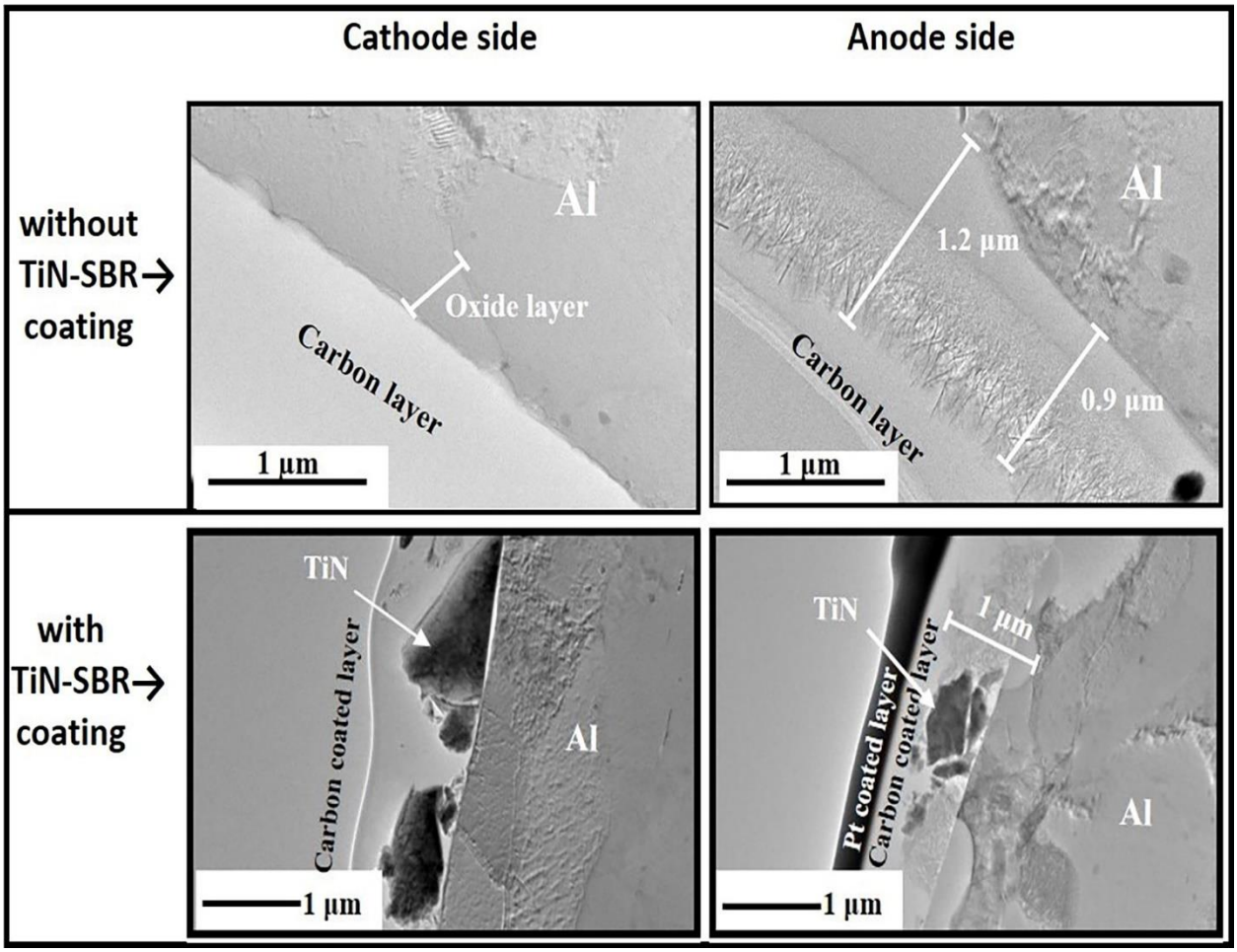

Fig. 15 Cross-sectional TEM images of the reaction gas isolating plate on the cathode and anode sides after 500 h of single cell power generation test (without and with TiN-SBR coating).

Therefore, the following findings were obtained because of conducting the PEMFC power generation test using a composite bipolar plate with A1060 as the reaction gas isolation plate and glassy carbon as the flow path forming material.

- No significant corrosion was observed on the A1060 isolation plate on the cathode side after the 500-h power generation test, but the anode side turned into white from the center of the flow path to the gas outlet side, and about 1 µm of a thick oxide film was formed.
- A thick oxide layer was formed when A1060 was immersed in distilled water while only a thin oxide layer was found in the saturated humid air.
- When a power generation test was conducted using A1060 bipolar plate coated with TiN-SBR, the cell voltage was increased significantly which was approached as similar as the

performance of graphite. It indicates that A1060 can be used as bipolar plates without any problem by performing surface treatment in combination with a carbon channel forming material.

References

1. B. -T. Tsai, C. -J. Tseng, Z. -S. Liu, C. -H. Wang, C. -I. Lee, C. -C. Yang, S. -K. Lo, *Int. J. Hydrogen Energy* **37**, 13060–13066 (2012).
2. H. Heidary, M. J. Kermani, B. Dabir, *Energy Convers. Manag.* **124**, 51–60 (2016).
3. M. Zhiani, S. Kamali, S. Majidi, *Int. J. Hydrogen Energy* **41**, 1112–1119 (2016).
4. M. Zhiani, S. Majidi, M. M. Taghiabadi, *Fuel cells* **13**, 946–955 (2013).
5. A. R. Vijay Babu, P. Manoj Kumar, G. Srinivasa Rao, *Alex. Eng. J.* **57**, 3953–3958 (2018).
6. H. Zeng, S. Gong, Y. Wang, Y. Shi, Q. Hu, N. Cai, *Energ. Convers. Manag*. **196**, 443–452 (2019).
7. Y. Liu, H. Li, *Energy* **189**, 116171 (2019).
8. A. Marinoiu, M. Raceanu, E. Carcadea, M. Varlam, I. Stefanescu, *Appl. Surf. Sci.* **424**, 93–100 (2017).
9. G. Zhang, L. Fan, J. Sun, K. Jiao, *Int. J. Heat Mass Tran.* **115**, 714–724 (2017).
10. G. Zhang, K. Jiao, *Energ. Convers. Manag*. **176**, 409–421 (2018).
11. D. Arora, C. Bonnet, M. Mukherjee, S. Raël, F. Lapicque, *Electrochim. Acta* **310**, 213–220 (2019).
12. T. Wang, Q. Li, H. Yang, L. Yin, X. Wang, Y. Qiu, W. Chen, *Energ. Convers. Manag*. **196**, 866–877 (2019).
13. Y. C. Park, S. H. Lee, S. K. Kim, S. Lim, D. H. Jung, S. Y. Choi, *Int. J. Hydrogen Energy* **38**, 10567–10576 (2013).
14. S. F. Husby H, O. E. Kongstein, A. Oedegaard, *Int. J. Hydrogen Energy* **2**, 951–957 (2014).
15. S. H. Lee, V. E. Pukha, V. E. Vinogradov, N. Kakati, S. H. Jee, S. B. Cho, *Int. J. Hydrogen Energy* **38**, 14284–14294 (2013).
16. D. Lee, J. W. Lim, S. Nam, I. Choi, D. G. Lee, *Compos. Struct*. **134**, 1–9 (2015).
17. K. Nikolov, K. Bunk, A. Jung, J. W. Gerlach, P. Kaestner, C. P. Klages, *Surf. Coat. Technol.* **328**, 142–151 (2017).
18. F. Madadi, A. Rezaeian, H. Edris, M. Zhiani, *Mater. Chem. Phys*. **238**, 121911 (2019).

19. P. Zhang, C. Hao, Y. Han, F. Du, H. Wang, X. Wang, J. Sun, *Surf. Coat. Technol.* **397**, 126064 (2020).
20. A. Hermann, T. Chaudhuri, P. Spagnol, *Int J Hydrogen Energy* **30**, 1297–1302 (2005).
21. H. Tawfik, Y. Hung, D. Mahajan, *J Power Sources* **163**, 755–767 (2007).
22. S. S. Dihrab, K. Sopian, M. A. Alghoul, M. Y. Sulaiman, *Renew Sustain Energy Rev.* **13**, 1663–1668 (2009).
23. R. A. Antunes, M. C. L. De Oliveira, G. Ett, V. Ett, *J Power Sources* **196**, 2945–2961 (2011).
24. S. Karimi, N. Fraser, B. Roberts, F. R. Foulkes. *Ann Mater Sci Eng.* **2012**, 1–22 (2012).
25. M. C. L. De Oliveira, G. Ett, R. A. Antunes, *J Power Sources* **206**, 3–13 (2012).
26. R. Taherian, *J Power Sources* **265**, 370–390 (2014).
27. A. Iwan, M. Malinowski, G. Pasciak, *Renew Sustain Energy Rev.* **49**, 954–967 (2015).
28. D. Y. Li, Y. X. Shi, H. P. Xu, Y. Chen, P. Zhou, X. W. Li, W. X. Feng, S. P. Wang, *Int. J. Electrochem. Sci.* **13**, 9346–9358 (2018).
29. C. -H. Lee, Y. -B. Lee, K. -M. Kim, M. -G. Jeong, and D. -S. Lim, *Renewable Energy* **54**, 46–50, (2013).
30. H. Yashiro, T. Ichikawa, S. -T. Myung, M. Kumagai, and S. Kozutsumi, *Zairyo-to-Kankyo* **60**(10), 432–434 (2011).
31. A. Jahan, M. A. Alam, S. Yonezawa, E. Suzuki, H. Yashiro, *ECS Trans.* **102**(5), 45–54 (2021).
32. M. A. Alam, A. Jahan, S. Yonezawa, A. Minoura, E. Suzuki, H. Yashiro, Zairyo-to-*Kankyo* **70**(3), 64–67 (2021).
33. M. A. Alam, A. Jahan, E. Suzuki, H. Yashiro, *ECS Trans.* **102**(5), 37–44 (2021).
34. Y. E. Dragon, *Light Metal* **9**, 47–56 (1953).
35. A. V. Krusenstjern, S. Tajima, *Electrochemistry* **27**(11), 583–591 (1959).
36. Japan Automobile Research Institute, NEDO Report (12-17-013-2-0002-2), 21, (2001).
37. S. Tsai, C. Bai, C. Lin, G. Shi, K. Hou, Y. Liu, M. Ger, M. *J. Power Sources* **214**, 51–58 (2012).
38. S. Zyun, *Electrochemistry* **78**(10), 846–851 (2010).

Chapter 3

Corrosion Behavior of Aluminum and Aluminum-Composite Bipolar Plates in the Simulated and Real Environments in Polymer Electrolyte Membrane Fuel Cells

Chapter 3: Corrosion Behavior of Aluminum and Aluminum-Composite Bipolar Plates in the Simulated and Real Environments in Polymer Electrolyte Membrane Fuel Cells

3-1 Introduction

Over the last few years, many research institutes in different countries have invested a lot in research and development in various sectors to minimize the energy and environmental concerns, including some new energy sources such as hydrogen energy, solar energy, biomass energy, wind energy, geothermal energy and specifically for the fuel cells.[1,2] In addition, exploring clean air and green energy generation is a routine apprehension; the fresh hydrogen energy created by technologies such as fuel cells, the key solutions for the 21st century,[3,4] and water electrolysis [5,6] has attracted vast research interests. Among these, fuel cells based on proton exchange membrane (PEMFCs) are clean energy electrochemical devices that use hydrogen and oxygen or air and subsequently generate water and heat *via* the direct effective conversion of chemical energy into electrical energy.[7,8] Currently, PEMFC, a typical representative of fuel cells and one of the fourth power generation devices which strongly switches equally between the research and marketplace as a latent supremacy source for future automotive and portable energy with numerous characteristics such as high-energy compactness, almost nil carbon-based gas release, low-temperature action (40–100 °C), low charge, easy assembly, fast start-up responses, and high energy proficiency.[9-17] Thus, PEMFC is the most suitable environmentally friendly energy system compared to fossil fuels in the vehicle power source area for holding the above features. Membrane electrode assembly (MEA) and bipolar plates (BPs) are the essential parts of PEMFC, where MEA is the combination of proton exchange membrane, gas diffusion and catalyst layers. The overview of a PEMFC is shown in **Fig. 1**.

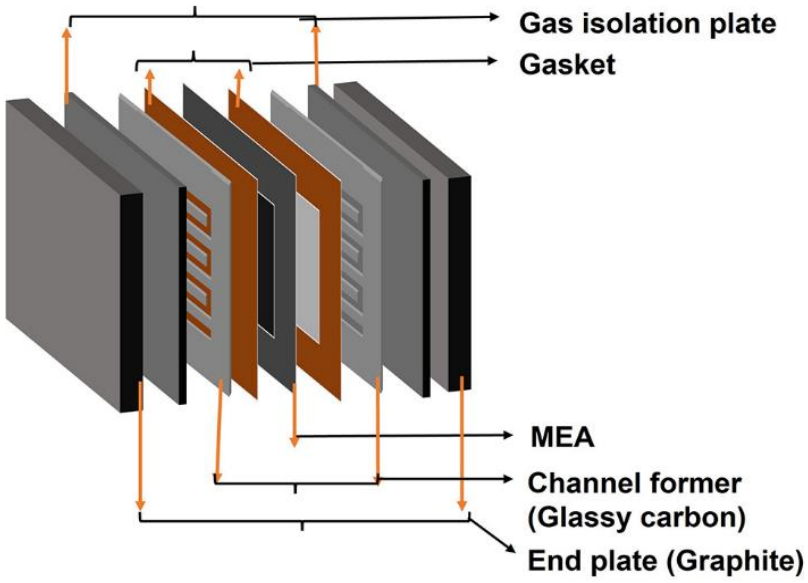

Fig. 1. An overview of PEMFC.

Besides catalysts and membranes, bipolar plate (BP), a significant and multifunctional component in the PEMFC stack, occupies around 60−80% of the weight and 35–45% of the total cost of PEMFC stack.[18]

BP plays a vital role in electronic assembly that can work and survive in harsh acidic conditions and is broadly used in PEMFC settings although its complete price, heaviness of the stack, water management transmission, and gas flow channels are the most important, challenging and concerning issue that should be overcome.[19,20] Hence, the formulation of a material that can reduce weight, cost, and corrosion rate is needed, which can be used as BP with low electrical resistance, superior corrosion resistance, and high chemical stability to recover the stable performance of BPs which is absolutely essential, though it is still a great challenge to simultaneously meet the moral conductivity and mechanical properties of the most appropriate BPs.

Presently, diverse materials such as graphite and metals have been commonly used for the creation of novel BPs in PEMFC.[21-23] The graphite BPs have some excellent advantages such as good corrosion resistance, better thermal and electrical conductivity although lower mechanical strength, large porosity and poor processing power are the main limitation for its application in PEMFC. On the other hand, the metals hold high strength, better processability and low cost compared to graphite.[24-27] In addition, the extraordinary power of carbon-based materials, or graphite, is their superior corrosion resistance, light mass, and little compactness, although they are lower than

metallic materials considering the mechanical durability and gas shielding properties. Hence, recently, the metals are used as the most potential materials for the BPs in PEMFC.[28,29]. Numerous studies have been conducted on modified surfaces, including metals and alloys. Based on these studies, metal-based BPs reduce fuel loss by around 22% compared to carbon-based BPs, though they have the reverse features, and corrosion safety is a particular and vigorous issue.[30-32] Recently, researchers suggest that the BP in PEMFCs classified into two portions: the gas isolating plate and the channel former.[33]

The most extensively studied applicant stainless steels (SSs) have also been verified and cast-off as BPs by numerous researchers,[34-36] who reported that corrosion expanse is slight and PEMFC output is steady even after 1000 h of operation.[37,38] But, unfortunately, it was thought that due to its massive weight, it could be a severe delinquent in light of transportation utilization. Along with these limitations, aluminum (Al) is regarded as one of the most promising materials for its renewal functions, and some of the remarkable facilities such as high electrical and fatigue resistance, high power, recyclability, thermal conductivity, low density, low price, and lightness.[39-41] It seems to be the Al BP maximum that diminishes 65% of heaviness compared to the SS BPs. Furthermore, Al is susceptible to corrosion due to the creation of a durable oxide film on the surface of the BPs in PEMFC.[42] So, our new proposal here is to use Al as a gas isolating plate.

Considering the use of metallic materials as the reaction gas isolating plate, it is necessary to investigate the corrosion behavior at the bottom of the flow path in the PEMFC environment, but the research on the corrosion behavior of metallic BPs is generally conducted based on the contact with MEA. It is performed assuming a severely corroded environment, such as the rib part in the BP systems. Since the bottom of the flow path does not come into direct contact with the MEA, it is expected that the corrosive environment will be milder than that of the rib part, and making it possible to use light metal materials such as Al, which are superior in terms of lightweight compared to conventional metal-based materials, was used in this work. However, there is almost no data on investigating the corrosion behavior of light metal materials in the environment at the bottom of the flow path of the BP.

In simulated conditions, earlier studies have concerted on the corrosion features of Al in some dilute acidic solutions such as sulfuric acid, hydrochloric acid,[43,44] sulfuric acid with hydrogen fluoride media,[45,46] and sodium sulfate with sodium fluoride solution.[47-49] It is known that the typical operating environment for PEMFC includes a pH value in the range of 3 to 6, which is

weakly acidic, whereas BPs are typically handled on crevice corrosion by discharging the major anions such as F^{-}, SO_4^{2-}, Cl^{-} etc from the perfluoro-sulfonic acid membrane, and the temperature can reach up to 80 °C.[50-52]

Though several studies have been proposed based on the simulated conditions, it is considered that the solutions generate through the cathode and anode during the power generation test are more rational and featured in PEMFC operating system. Thus, it is significantly needed to evaluate the correlation of the corrosion behavior of Al between the solutions in simulated and real environments in PEMFC. Considering the above facts, our research interest was to find out the corrosion behavior of Al in simulated and real environments for use as a BP component in PEMFC. In this context, a PEMFC BP was prototyped using the carbon-based material as the channel former and Al as the reaction gas isolating plate. Besides, the corrosive environment at the bottom of the flow path and the useability of Al as a reaction isolating plate were investigated through the power generation tests.

3-2 Experimental Section

3-2-1 Materials and Instruments.

The Al was used as the study material and designated as the test specimens, which were provided by Nilaco, Tokyo. The test specimens had dimensions of 30 mm × 20 mm × 1 mm. Prior to the immersion experiments, the surface of the test specimens was ground employing several marks of emery paper with No. 40, 60, 1200, and 2000 to remove the surface contaminants, and polished reflexively applying alumina paste, sequentially cleaned using distilled water, and dried at room temperature.

3-2-2 Immersion Process and Analysis. The immersion of the test specimens was done at 80 °C under aerated and deaerated conditions. The target solutions aimed at the immersion process were distilled water (DSW), 0.1 ppm F^{-}, 0.1 ppm SO_4^{2-}, 0.1 ppm F^{-} + 0.1 ppm SO_4^{2-}, 0.1 ppm F^{-} + 0.5 ppm SO_4^{2-}, and 0.1 ppm F^{-} + 1 ppm SO_4^{2-} prepared by using reagent grades of NaF and Na_2SO_4, which were purchased from Wako Pure Chemical Industries and Kanto Chemical Company Industries, respectively, Tokyo. In the present study, we also used the real solutions (cathodic and anodic solutions) collected from the cathode and anode of fuel cell during the 500 h of single cell power generation test, where Al was used as a gas isolating plate. All the real solutions were

analyzed by an ion analyzer (IA-100) provided by TOA Electronics Ltd., Tokyo. Initially, all the experimental samples were weighed, kept in 90 cm^3 of aqueous solutions, and observed for 120 h of immersion. All the immersion tests were conducted *via* a program control oven. Afterward, the test specimens were separated from the experimental solutions, sequentially cleaned using distilled water, dried in the desiccator at room temperature, and took the final weight. The microscopic images were taken by an Olympus metallurgical microscope (U-IF550, BX60M, Japan). The corrosion rate of the test specimens was calculated before and after immersion in the test solutions using weight loss method.

3-2-3 Corrosion Products Characterizations. The morphologies of the test specimens before and after the immersion test in simulated and real environments as well as before and after the single cell power generation tests were evaluated through high-resolution scanning electron microscopic (SEM) images and energy dispersive X-ray (EDX) spectroscopy using FE-SEM (JSM-7800F, JEOL, Japan), maintaining 10 kV and 10 mm of accelerating voltage and working distance, respectively. The JEM-F200 was used for transmission electron microscope (TEM) measurement. For the TEM measurement, the test specimens were prepared using a focused ion beam (FIB), loaded on a copper mesh, and processed as thinly as possible by a Ga+ ion beam at an acceleration voltage of 30 kV. The atomic force microscope (AFM) with non-contact mode of the Park Systems NX-10, Japan, was used to detect and investigate the surface topography of the study materials after exposure to the simulated and recovered solutions. The surface roughness parameters, such as arithmetic average surface roughness (*Ra*) and root mean square roughness (*Rq*), were also calculated from three different areas of dimension.

3-3 Results and Discussion

3-3-1 Corrosion Rate. The immersion test was executed to evaluate the effect of fluoride and sulfate ions on the corrosion rate of Al as a BP component in PEMFC. During the immersion, the test specimens were kept in the previously prepared different test solutions mentioned in experimental section as well as in the recovered solutions collected from the anode and cathode sides of PEMFC for different duration at 80 °C maintaining the deaerated environment using Ar gas with the help of glove box. It is revealed that the weight of the test specimens was gradually decreased after immersion in case of all the simulated test solutions due to corrosion and comparatively lower in the recovered solutions. The results showed that the wildest corrosion rate

and the worst corrosion resistance was found in case of the immersion in 0.1 ppm F^- solution and *vice versa* in case of 0.1 ppm F^- + 1 ppm SO_4^{2-} solution. It indicates that the fluoride ions accelerated the corrosion of Al plates through changing the structure and destroying the protectiveness of the film formed on Al surface after immersion. Thus, the corrosion resistance of Al plate decreased with the increase of fluoride ions concentration because the fluoride ions could dissolve the barrier film of Al plate into porous by forming some Al compounds. In addition, it can be summarized that the fluoride ions concentration was high enough to dissolve the entire barrier film into discontinuous and porous film, because the dissolution rate of Al_2O_3 surpassed its formation rate. Under this condition, the fluoride ions (F^-) reached to the surface of Al specimens and corroded the Al directly. According to **Fig. 2** and **Fig. 3** it reveals that the corrosion amount was slightly decreased with increasing the concentration of sulphate ions in the test solutions for both the cases (aerated and deaerated). In addition, **Fig. 2** and **Fig. 3** show that the corrosion rate

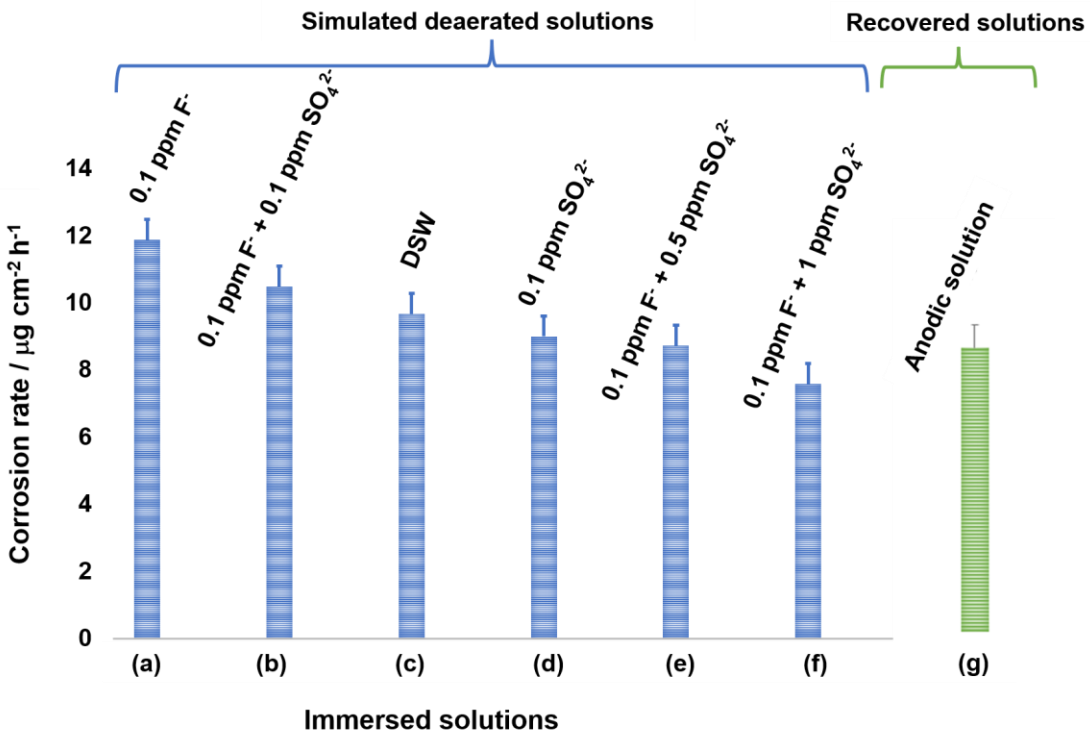

Fig. 2 Corrosion rate of Al after 120 h of immersion at 80 °C in deaerated solutions of (a) 0.1 ppm F^-, (b) 0.1 ppm F^- + 0.1 ppm SO_4^{2-}, (c) DSW, (d) 0.1 ppm SO_4^{2-}, (e) 0.1 ppm F^- + 0.5 ppm SO_4^{2-}, and (f) 0.1 ppm F^- + 1 ppm SO_4^{2-} and (g) recovered solution from anode.

of the test specimens was higher in case of the recovered solutions from anode (deaerated) than cathode (aerated) which indicates that the anode part was more corroded than the cathode part which will be discussed more in the next sections in this research. Moreover, **Fig. 2 and Fig. 3** show the corrosion rate of the test specimens after immersion in different simulated and recovered test solutions which indicates that the sulfate ions reduce the amount of corrosion. Therefore, it is considered that the sulfate ions will be acted as inhibitors when Al will be used as BP in the PEMFC environment.

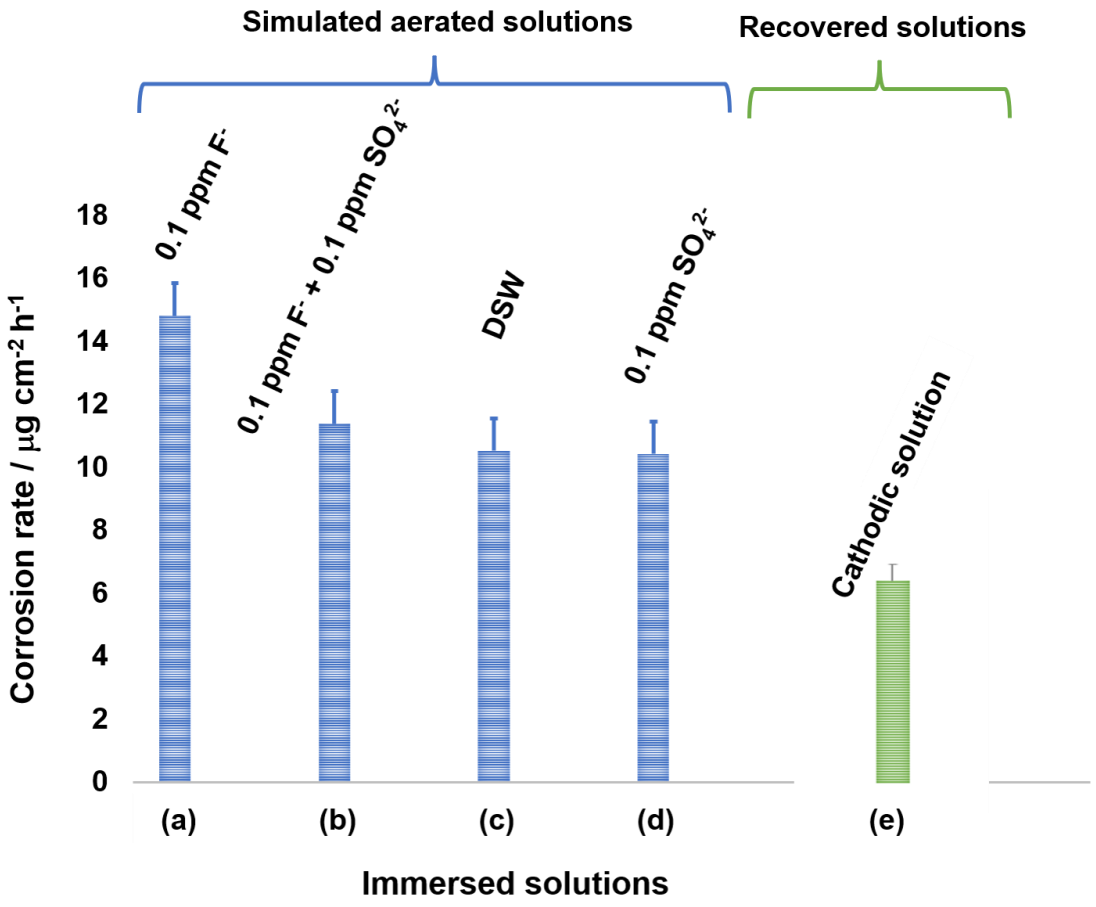

Fig. 3 Corrosion rate of Al after 120 h of immersion at 80 °C in aerated solutions of (a) 0.1 ppm F^-, (b) 0.1 ppm F^- + 0.1 ppm SO_4^{2-}, (c) DSW, (d) 0.1 ppm SO_4^{2-}, and (e) recovered solution from cathode.

3-3-2 Morphological Characterizations.

3-3-2-1 SEM Analysis Immersed in Simulated Solutions. In order to focus the variations of the Al surface, all samples were characterized using the surface sections of the test specimens by scanning electron microscopy (SEM) after exposure to fluoride-containing solutions of different amount of SO_4^{2-} ions for 120 h at 80 °C as shown in **Fig. 4.** From the SEM images, it is observed under the simulated conditions that some cubic precipitates or cuboid structures as obvious corrosion products were found on Al surface for almost all experimental solutions, though no pits or cracks were seen. Instead, in case of 0.1 ppm F^- + 0.5 ppm SO_4^{2-} solution, the dimension of the crystals was larger and overlapped with each other. The cubic corrosion products decreased with rising the concentration of SO_4^{2-} ions. This performance is attributed to the Al hydroxides and their oxides, which are crystallized on the surface, indicating general corrosion under the above conditions. When the concentration of SO_4^{2-} ions was increased up to 1 ppm, the lower corroded products were detected, and the surface was smoother than the previous one similar to Al. It could be seen that the entire surface was much smoother than the solutions with fewer sulfate ions, which indicates that the sulfate ions showed corrosion inhibitory action on the surface of the test samples.

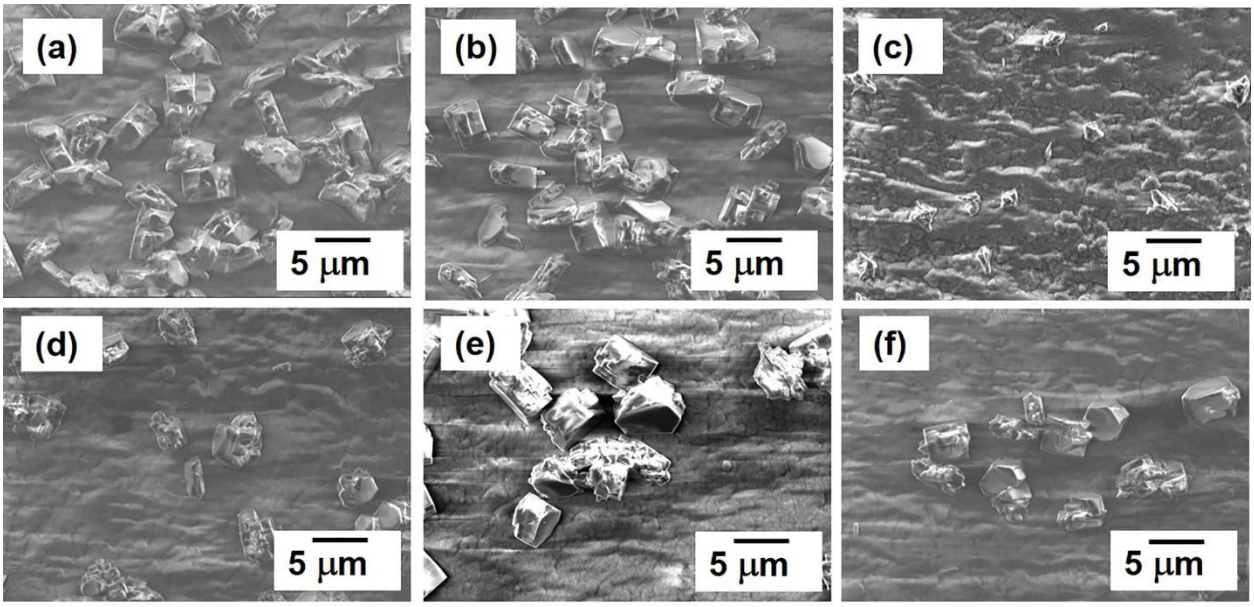

Fig. 4 Corrosion morphology of Al after 120 h of immersion in the simulated solutions (deaerated) of (a) 0.1 ppm F^-, (b) 0.1 ppm F^- + 0.1 ppm SO_4^{2-}, (c) DSW, (d) 0.1 ppm SO_4^{2-}, (e) 0.1 ppm F^- + 0.5 ppm SO_4^{2-}, and (f) 0.1 ppm F^- + 1 ppm SO_4^{2-} at 80 °C.

3-3-2-2 SEM Images in Recovered Solutions from Single Cell Power Generation Test.

The SEM morphologies of Al after being exposed for 120 h at 80 °C to the recovered solutions from cathode and anode during the single cell power generation test is displayed in **Fig. 5**. From the images, it can be seen that for both solutions, the surfaces of the test samples were corroded, but the superior corroded region was noticed for the anodic solution, apparently for the concerted actions of the high acidity, presence of hydrogen-rich (anode) environment, and halide anions, which are not similar to the simulated experiment results. In case of the simulated test result, some cubic precipitates were seen on the surfaces of the test specimen when the solution contained only F^- and SO_4^{2-}, but some granular corrosion products were noticed in the recovered solutions containing F^-, SO_4^{2-}, Cl^- and PO_4^{3-}, indicating the general corrosion under these conditions. In addition, it is acknowledged that the PO_4^{3-} ion was found as the relative ions measured by the help of an ion analyzer from the collected solutions of anode and cathode channels after 500 h of single cell power generation test.

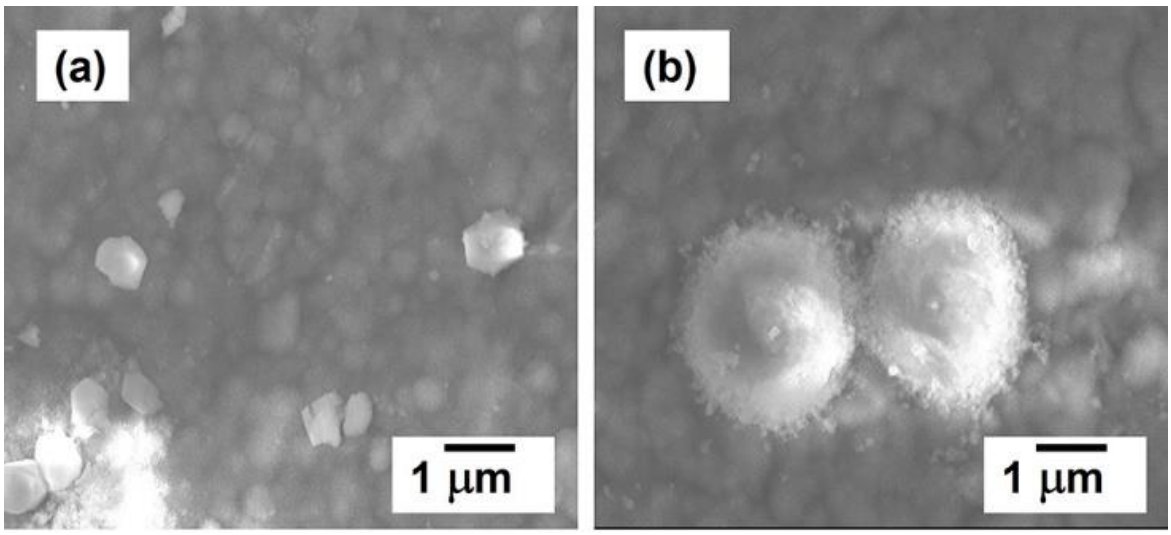

Fig. 5 Overall morphology by SEM images from the (a) cathodic (aerated) and (b) anodic (deaerated) solutions recovered from 500 h of single cell operation test and immersed at 80 °C for 120 h.

3-3-3 EDX mappings analysis.

3-3-3-1 EDX mappings for recovered solutions

The elemental compositions through EDX mapping for both cathodic and anodic solutions is shown in **Fig. 6**. The EDX analysis confirms that the surface oxide layer was more enriched with the presence of aluminum (Al), carbon (C) and oxygen (O) elements upon exposure of the Al test samples to the test solutions (anodic and cathodic). Furthermore, **Fig. 6** reveals the elemental compositions with 64.00% of oxygen (O) and 7.24% of carbon (C) for anodic solution and the elemental compositions with 61.68% of oxygen (O) and carbon (C) of 10.76% for cathodic solution which is high and illustrates the presence of corrosion products.

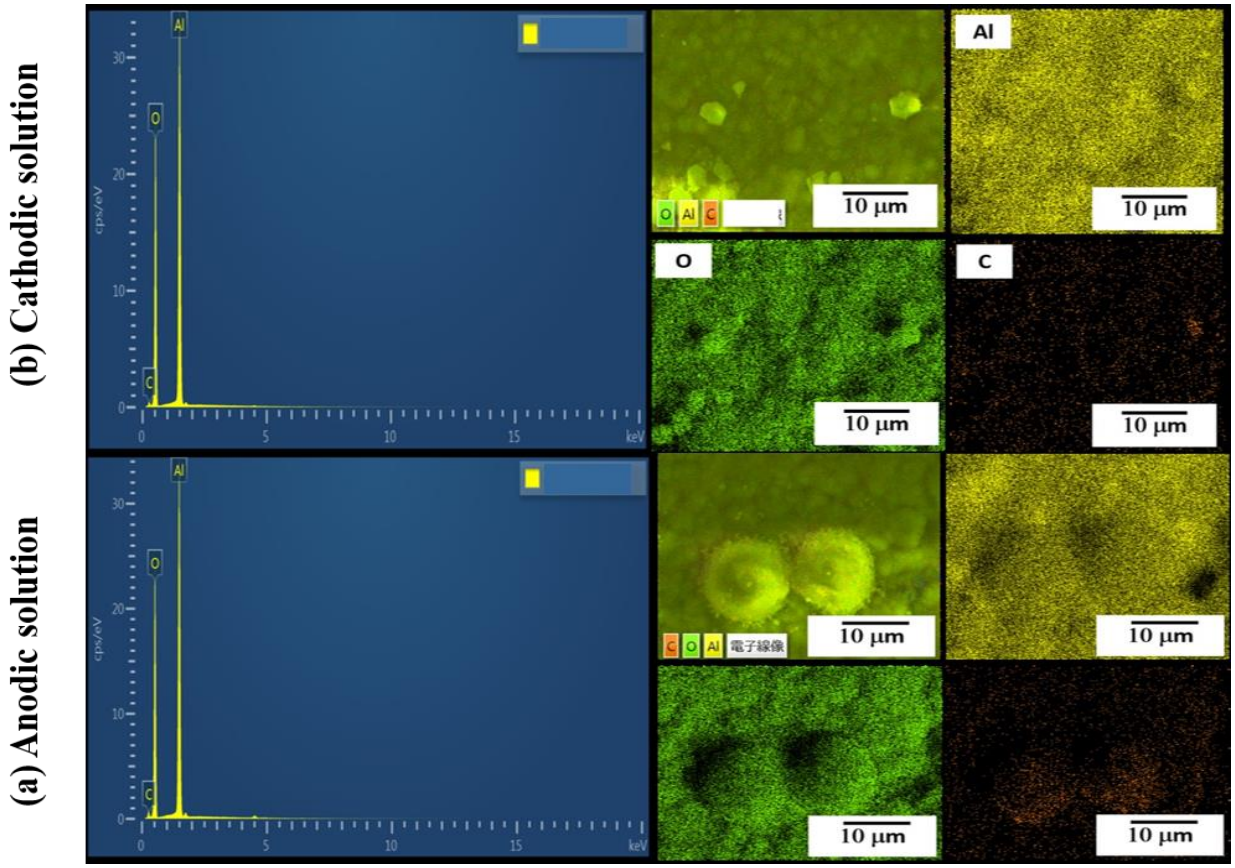

Fig. 6 EDX elemental mapping of Al test samples after 120 h of immersion at 80 °C in (a) cathodic (aerated) and (b) anodic (deaerated) solutions recovered from 500 h of single cell operation test.

3-3-3-2 EDX mappings for simulated solutions.

Table 1 characterizes the EDX mapping results to determine the composition of corrosion products after exposure to different environments. In case of 0.1 ppm F^- solution, the oxide layer of the test sample as corrosion products was enhanced by fluorine whose atomic percent ratio was 0.11. But,

in case of 0.1 ppm F^- + 1 ppm SO_4^{2-} solution, the amount of the oxide layer as corrosion products in the test sample was decreased in presence of additional sulfate ion (1 ppm SO_4^{2-}) where the atomic percent ratios of fluorine and sulfur were 0.01 and 0.16, respectively. So, it was clear that sulfate ions act as corrosion inhibitors as the oxide layer was slightly minimized and the atomic percent ratio of sulfur was higher than fluorine.

Table 1. EDX analysis of Al after 120 h of immersion in 0.1 ppm F^- and 0.1 ppm F^- + 1 ppm SO_4^{2-} solution:

Immersion in 0.1 ppm F^- solution				Immersion in 0.1 ppm F^- + 1 ppm SO_4^{2-}			
Element	Line (c/s)	Weight%	Atomic%	Element	Line (c/s)	Weight%	Atomic%
Al	Kα	40.21	28.03	Al	Kα	40.70	28.63
O	Kα	55.82	66.38	O	Kα	54.88	64.46
C	Kα	3.86	5.48	C	Kα	4.25	6.74
F	Kα	0.11	0.11	F	Kα	0.01	0.01
		100.00	100.00	S	Kα	0.16	0.16
						100.00	100.00

3-3-4 Cross-sectional TEM images analysis.

3-3-4-1 For Simulated Solutions. Fig. 7 displays the detailed cross-sectional transmission electron microscopy (TEM) investigation of the Al test samples after 120 h of exposure in different solutions (deaerated) at 80 °C. For all solutions, it is clearly seen that there is a two-layer thick oxide film (the outer layer looks fibrous and the inner layer looks dense) with an unusual thickness on the surface of the test samples. The thickness of the corrosion products was found to be 1.30, 1.25, 1.23, 1.20, 1.17, and 1.10 μm after immersion in 0.1 ppm F^-, 0.1 ppm F^- + 0.1 ppm SO_4^{2-}, DSW, 0.1 ppm SO_4^{2-}, 0.1 ppm F^- + 0.5 ppm SO_4^{2-}, and 0.1 ppm F^- + 1 ppm SO_4^{2-} solutions, respectively, at 80 °C in the simulated environment (deaerated). Thus, the results suggested that the thickness

of Al was significantly reduced with increasing the concentrations of sulfate ions, as conversed earlier. Thus, it was considered that the function of sulfate ions is as the corrosion inhibitor.

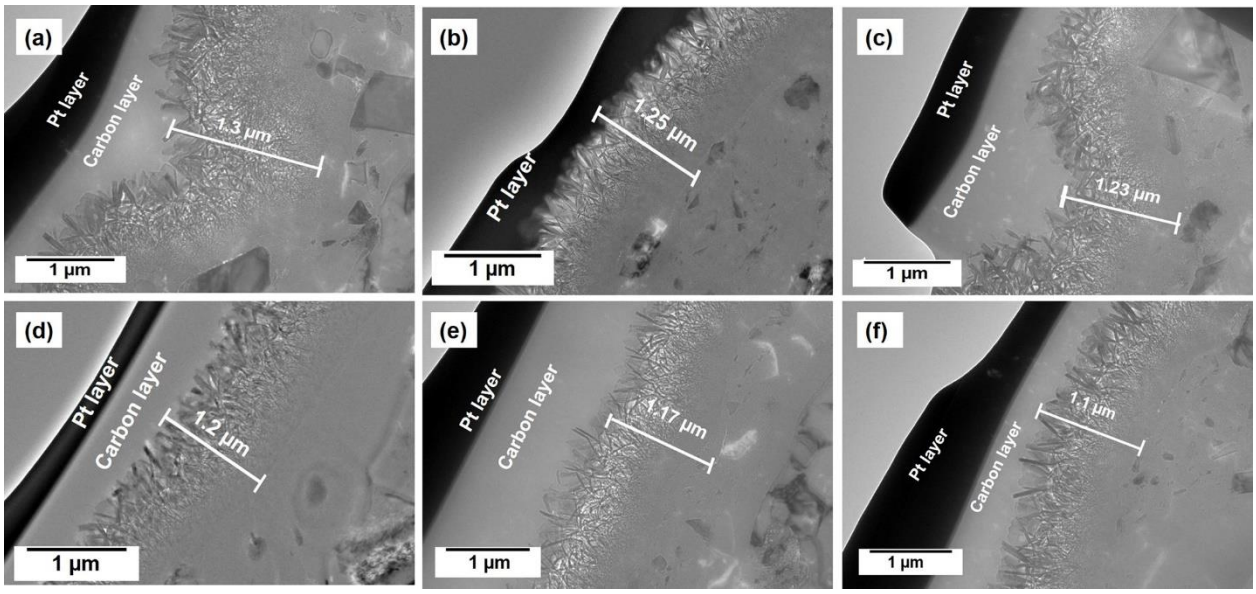

Fig. 7 TEM investigations of Al test samples after 120 h of immersion in (a) 0.1 ppm F^-, (b) 0.1 ppm F^- + 0.1 ppm SO_4^{2-}, (c) DSW, (d) 0.1 ppm SO_4^{2-}, (e) 0.1 ppm F^- + 0.5 ppm SO_4^{2-}, and (f) 0.1 ppm F^- + 1 ppm SO_4^{2-} solutions at 80 °C in the simulated environment (deaerated).

3-3-4-2 For Recovered Solutions. Fig. 8 shows the cross-sectional TEM images of Al after exposure to recovered (cathodic and anodic) soliutions from single cell operation. Apparently, the Al endured chemical attack and formed a film with different thicknesses both in cathodic and anodic solutions. The thickness of the films was around 1.07 µm and 1.2 to 1.4 µm for cathodic and anodic solutions, respectively. It is considered that the higher thickness of the films in the case of anodic solutions was found. It is considered that the higher thickness of the films in case of anodic solutions was found due to the presence of some surface-enriched contaminants such as F^-, SO_4^{2-}, Cl^-, PO_4^{3-} and NO_2^- ions on the anode side of the gas isolating plate at the beginning of single cell power generation test. It is mentioned that the anodic solution was collected from the anode side of the BP during single cell power generation test under the standard conditions of the single cell power generation test used in this study. The air flow rate on the anode side was 125 $cm^3\,min^{-1}$, and the utilization rate was 70%. It was observed that, the surface becomes smoother as

the operation time increases. That's why we did not treasure any aggressive ions in the anodic solution with increasing time during the single cell power generation test.

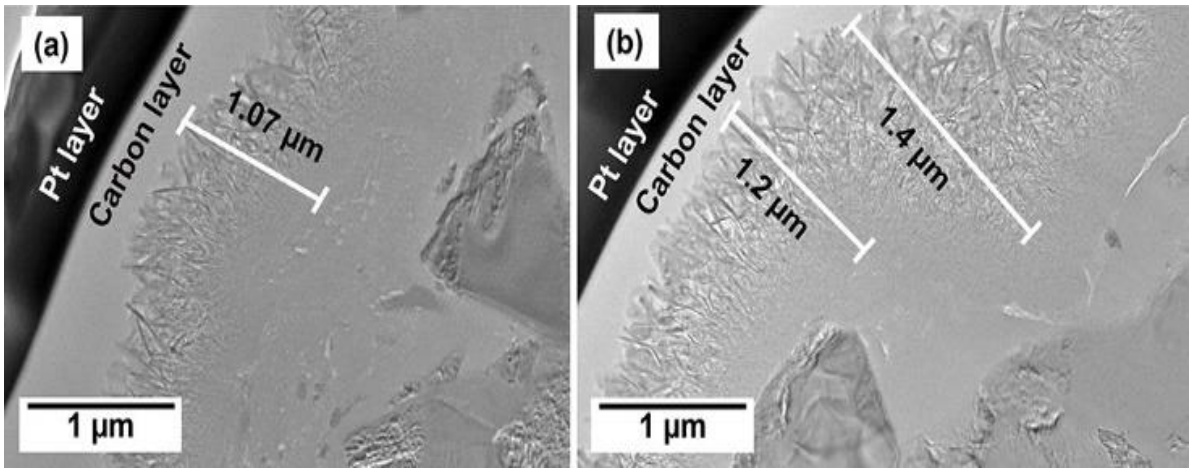

Fig. 8 Cross-sectional TEM images of Al after 120 h of exposure at 80 °C to recovered solutions from (a) cathode and (b) anode.

3-3-5 Surface Topography by AFM. AFM topography was used to assess the surface roughness of the test samples. Three-dimensional (3D) AFM structure images of Al after 120 h of immersion in different experimental solutions in the simulated environment at 80 °C are shown in **Fig. 9.** The surface roughness of the test samples in the simulated environment under deaerated and aerated condition was estimated using the roughness parameters, *Ra* shown in **Table 2 and Table 3.** The results demonstrate that the higher surface roughness in deaerated condition was found in the case of immersion in 0.1 ppm F^- solution (*Ra* 1.673 µm) and lower in the case of 0.1 ppm F^- + 1 ppm SO_4^{2-} solution (*Ra* 0.429 µm). On the contrary, the surface roughness in aerated condition was found in the case of immersion in 0.1 ppm F^- solution (*Ra* 1.837 µm) and in the case of 0.1 ppm F^- + 0.1 ppm SO_4^{2-} solution (*Ra* 1.621 µm) It is considered that the surface roughness of Al substantially reduces with increasing concentrations of sulfate ions, which indicates lower corrosion products occurred in the test samples. Thus, it can be suggested that the sulfate ions play the role of the corrosion inhibitor, which is also correlated with the SEM and TEM images explained in earlier sections.

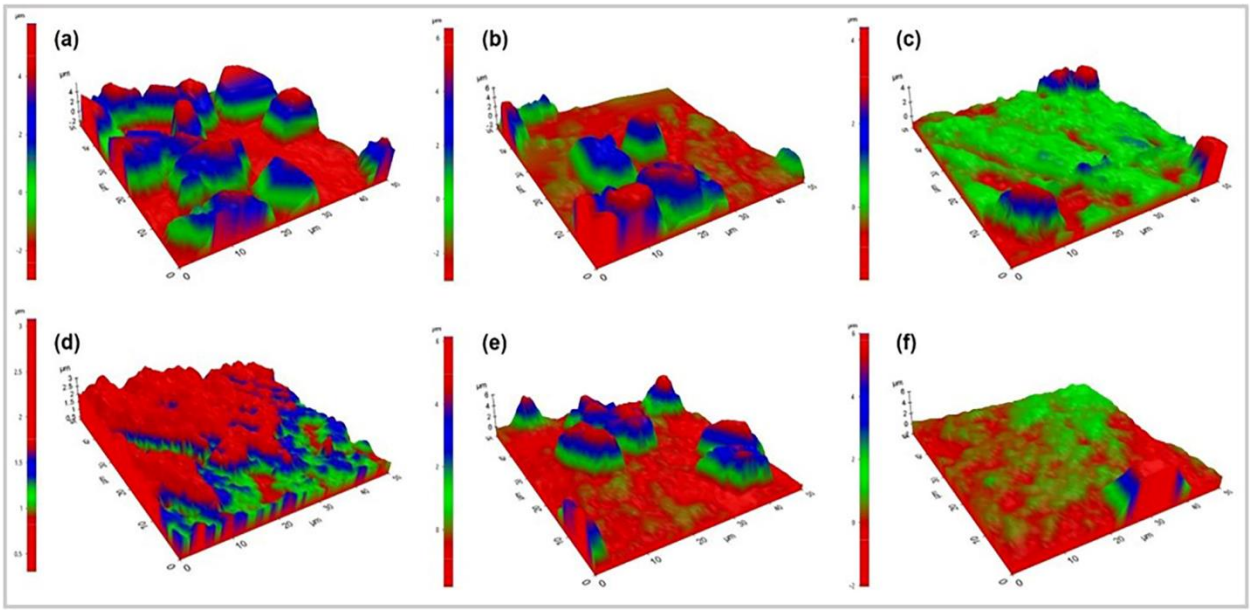

Fig. 9 AFM topography (3D) images of Al after 120 h of immersion in (a) 0.1 ppm F^-, (b) 0.1 ppm F^- + 0.1 ppm SO_4^{2-}, (c) DSW, (d) 0.1 ppm SO_4^{2-}, (e) 0.1 ppm F^- + 0.5 ppm SO_4^{2-}, and (f) 0.1 ppm F^- + 1 ppm SO_4^{2-} solutions at 80 °C in the simulated environment (deaerated)**.**

Table 2. Surface roughness value of Al after 120 h of immersion in the simulated deaerated and recovered / real solutions (anodic).

	Used solutions	Average surface roughness, *Ra* (*μ*m)
Simulated solutions	0.1 ppm F^-	1.673
	0.1 ppm F^- + 0.1 ppm SO_4^{2-}	1.150
	DSW	0.908
	0.1 ppm SO_4^{2-}	0.508
	0.1 ppm F^- + 0.5 ppm SO_4^{2-}	0.537
	0.1 ppm F^- + 1 ppm SO_4^{2-}	0.429
Real/ Recovered solutions	Anodic solution	0.902

Table 3. Surface roughness value of Al after 120 h of immersion in the simulated aerated and recovered / real solutions (cathodic)

	Used solutions	Average surface roughness, *Ra* (μm)
Simulated aerated solutions	0.1 ppm F^-	1.837
	0.1 ppm F^- + 0.1 ppm SO_4^{2-}	1.621
	DSW	1.109
	0.1 ppm SO_4^{2-}	0.886
Real/ Recovered solutions	Cathodic solution	0.580

The two-dimensional (2D) surface morphology and three-dimensional (3D) structure appearance on the left and right sides, respectively, of Al after 120 h of exposure at 80 °C in the recovered solutions (cathodic and anodic) collected during the single cell power generation test which is explored *via* AFM and illustrated in **Fig. 10**. A remarkable change in the AFM topography of Al when exposed to cathodic and anodic solutions was observed. In comparison, it appears rational to suspect that the surface of the test samples exposed in cathodic solution has lower roughness values than that in anodic solution, and it is outward that the surface is relatively smooth, which also corresponds to the SEM images.

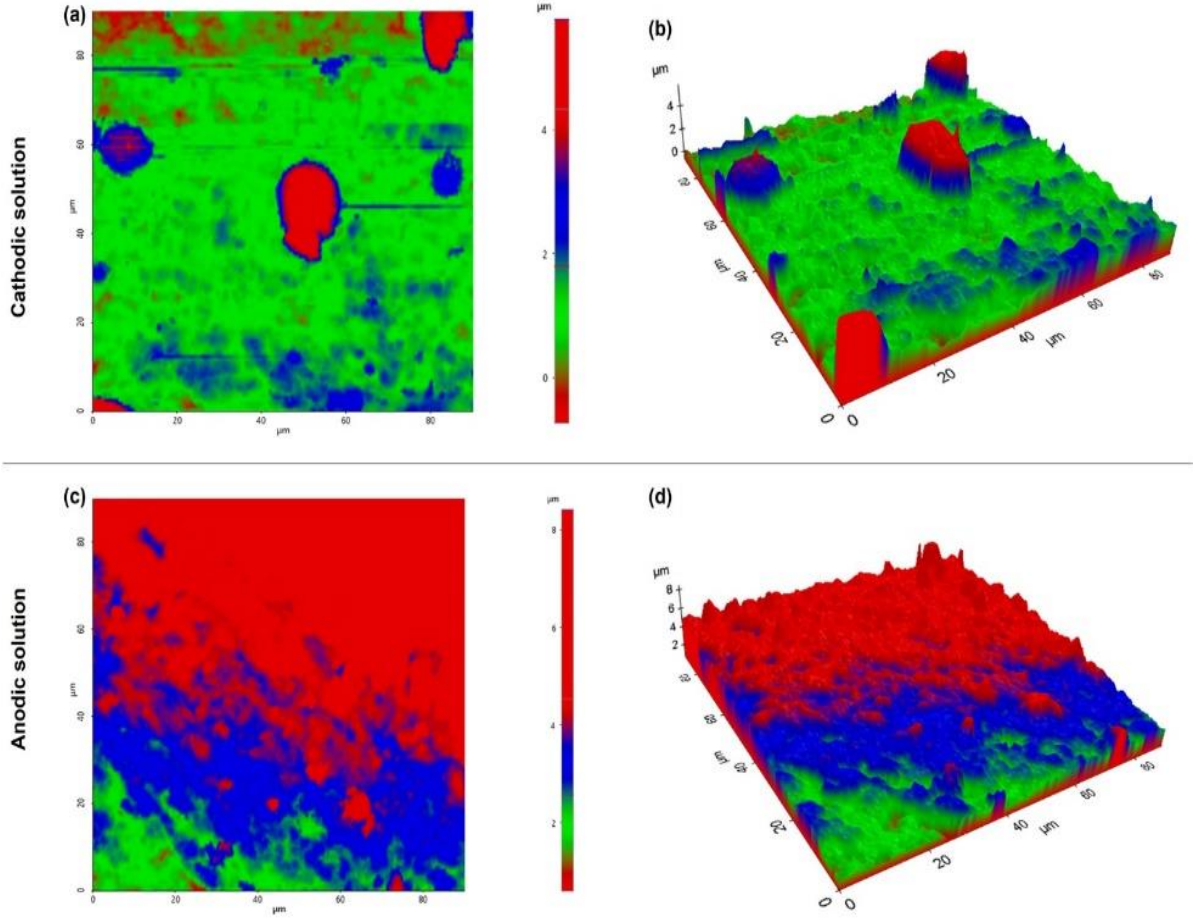

Fig. 10 AFM topography (2D and 3D) images of Al in the recovered solutions from cathode (a, b) and anode (c, d) after 120 h of immersion at 80 °C.

3-4 Conclusion

In this chapter, we have reported the corrosion behavior of Al and its correlation between the simulated and real environments for use as BPs in PEMFC and the following findings were attained:

- Systematically explored the corrosion performance of Al in simulated and real environments in PEMFC. Surprisingly, the results showed that the corrosion in the real environment was more positive than that in the simulated environment.
- Almost no substantial corrosion was discovered on the Al reaction gas isolating plate on the cathode side after the 500 h of single cell power generation test. It was clearly seen that the gas isolating plate maintained its metallic luster, and no thick film was observed. Thus,

it was presumed that the cathode side was in an environment where only gas was present during the single cell power generation test. However, in case of the anode side, the Al gas isolating plate maintained its luster near the gas inlet side but turned into white discoloration along the flow path from the central part to the gas outlet side, and a hydrated oxide layer of pseudo-boehmite with a two-layer structure of around 1 μm thick oxide film was formed after 500 h of single cell power generation test. So, it was suggested that during the single cell power generation test, the condensed water in which humidified gas and back-diffused water were condensed existed in the flow path on the anode side.

- A two-layer thick oxide film of approximately 1.2 μm was formed on the surface when Al was immersed in distilled water, which is also considered to be a hydrated oxide film of pseudo-boehmite.

Thus, it is concluded that the Al would become the suitable candidate as the gas isolating plate material in polymer electrolyte membrane fuel cell applications.

References

1. X. Li, *CRC Press*, (2005).
2. W. R. Daud, R. E. Rosli, E. H. Majlan, S. A. A. Hamid, R. Mohamed, T. Hosaini, *Renew. Energy* **113**, 620−638 (2017).
3. O. Z. Sharaf, M. F. Orhan, *Renew. Sust. Energy Rev.* **32**, 810−853 (2014).
4. D. R. Dekel, *J. Power Sources* **375**, 158−169 (2018).
5. W. E. Mustain, P. A. Kohl, *Nat. Energy* **5***,* 359−360 (2020).
6. M. R. Kraglund, M. Carmo, G. Schiller, S. A. Ansar, D. Aili, E. Christensen, J. O. Jensen, *corros. Sci.* **12***,* 3313−3318 (2019).
7. G. Hoogers, Fuel Cell Technology Handbook; CRC Press: Florida, USA, 2003.
8. A. Barjola, J. L. Reyes-Rodríguez, O. Solorza-Feria, E. Giménez, V. Compañ, *Ind. Eng. Chem. Res.* **60***,* 9107−9118 (2021).
9. H. Chen, Z. Song, X. Zhao, T. Zhang, P. Pei, C. Liang, *Appl. Energy* **224**, 289–299 (2018).
10. M. X. Li, Y. F. Bai, C. Z. Zhang, Y. X. Song, S. F. Jiang, D. Grouset, M. J. Zhang, *Int. J. Hydrog. Energy* **44***,* 10677–10693 (2019).
11. Y. X. Song, C. Z. Zhang, C.Y. Ling, M. Han, R.Y. Yong, D. Sun, J. R. Chen, *Int. J. Hydrog. Energy* **45***,* 29832–29847 (2020).

12. Y. Q. Zhao, Y. J. Mao, W. X. Zhang, Y. L. Tang, P. Z. Wang, *Int. J. Hydrog. Energy* **45**, 23174–23200 (2020).
13. J. Shi, P. Zhang, Y. Han, H. Wang, X. Wang, Y. Yu, J. Sun, *Int. J. Hydrog. Energy* **45**, 10050-10058 (2020).
14. P. Yi, D. Zhang, D. Qiu, F. Peng, X. Lai, *Int. J. Hydrog. Energy* **44**, 6813-6843 (2019).
15. P. Yi, L. Zhu, C. Dong, K. Xiao, *Surf. Coat. Technol.* **363,** 198-202 (2019).
16. R. Haider, Y. Wen, Z. F Ma, D. P. Wilkinson, L. Zhang, X. Yuan, S. Song, J. Zhang, *Chem. Soc. Rev.* **50**, 1138-1187 (2021).
17. K. Yao, D. Adams, A. Hao, J. P. Zheng, Z. Liang, N. Nguyen, *Energy & Fuels* **31**,14320−14331 (2017).
18. H. Tsuchiya, O. Kobayashi, *Int. J. Hydrog. Energy* **29**, 985-990 (2004).
19. Y. Wang, S. Zhang, P. Wang, Z. Lu, S. Chen, L. Wang, *Prog. Org. Coat*. **137**, 105327 (2019).
20. X. Z. Wang, C. P. Ye, D. D. Shi, H. Q. Fan, Q. Li, *Corros. Sci.* **189**, 109624 (2021).
21. R. A. Antunes, M. C. L. De Oliveira, G. Ett, V. Ett, *J. Power Sources* **196**, 2945–2961 (2011).
22. M. C. L. De Oliveira, G. Ett, R. A. Antunes, *J. Power Sources* **206**, 3−13 (2012).
23. R. Taherian, *J. Power Sources* **265**, 370–390 (2014).
24. A. Hermann, T. Chaudhuri, P. Spagnol, *Int. J. Hydrog. Energy* **30**, 1297–1302 (2005).
25. Y. D. Kuan, C. W. Ciou, M. Y. Shen, C. K. Wang, R. Z. Fitriani, C. Y. Lee, *Int. J. Hydrog. Energy* **46**, 16801−16814 (2021).
26. S. Simaafrookhteh, M. Khorshidian, M. Momenifar, *Int. J. Hydrog. Energy* **45**, 14119-14132 (2020).
27. Y. Zeng, Z. He, Q. Hua, Q. Xu, Y. Min, *ACS Omega* **5,** 16976−16985 (2020).
28. V. Mehta, J. S. Cooper, *J. Power Sources* **114**, 32-53 (2003).
29. Y. Peiyun, Z. Di, Q. Diankai, P. Linfa, L. Xinmin. *Int. J. Hydrog. Energy* **44**, 6813−6843 (2019).
30. H. Tawfik, Y. Hung, D. Mahajan, *J. Power Sources* **163**, 755−767 (2007).
31. A. G. Gonzalez-Gutierrez, M. A. Pech-Canul, G. Chan-Rosado, P. J. Sebastian, *Fuel* **235**, 1361−1367 (2019).
32. Y. Hung, H. Tawfik, D. Mahajan, *J. Power Sources* **186**, 123−127 (2009).

33. H. Yashiro, T. Ichikawa, S. -T. Myung, M. Kumagai, Kozutsumi, *Zairyo-to-Kankyo* **60**, 432–434 (2011).
34. D. P. Davies, P. L. Adcock, M. Turpin, S. J. Rowen, *J. Power Sources* **86**, 237−242 (2000).
35. A. K. Iversen, *Corros. Sci.* **48**,1036–1058 (2006).
36. M. Kumagai, S. -T. Myung, Y. Katada, H. Yashiro, *Electrochim. Acta* **211**, 754−760 (2016).
37. H. Yashiro, R. Asaishi, S. Kuwata, M. Kumagai, A. Yao. *Trans. Mater. Res. Soc. Jpn*. **32**, 963-966 (2007).
38. M. Kumagai, S. -T. Myung, S. Kuwata, R. Asaishi, H. Yashiro, *Electrochim. Acta* **53**, 4205-4212 (2008).
39. D. Y. Li, Y. X. Shi, H. P. Xu, Y. Chen, P. Zhou, X.W. Li, W. X. Feng, S. P. Wang, *Int. J. Electrochem. Sci.* **13**, 9346−9358 (2018).
40. S. Caporali, A. Fossati, A. Lavacchi, I. Perissi, A. Tolstogouzov, U. Bardi, *Corros. Sci.* **50**, 534–539 (2008).
41. R. Rosaliza, W. B. Wan Nik, H. B. Senin, Mater. *Chem. Phys.* **107**, 281–288 (2008).
42. V. Mountarlier, M. P. Gigander, B. Normand, J. Pagetti, *J. Corros. Sci*. **47**, 937−951(2005).
43. J. P. Dasquet, D. Caillard, E. Conforto, *Thin Solid Films* **371**, 183−190 (2000).
44 I. V. Aoki, M. C. Bernard, C. D. Torresi, *Electrochim. Acta* **46**, 1871-1878 (2001).
45. M. A. Alam, A. Jahan, A. Minoura S. Yonezawa, E. Suzuki, H. Yashiro, H. *Zairyo-to-Kankyo* **70**, 64−67 (2021).
46. A. Jahan, M. A. Alam, S. Yonezawa, E. Suzuki, H. Yashiro, *ECS trans.* **102**, 45−54 (2021).
47. M. A. Alam, A. Jahan, S. Yonezawa, E. Suzuki, H. Yashiro, *ECS trans.* **108**, 131−141 (2022).
48. M. A. Alam, A. Jahan, E. Suzuki, H. Yashiro, *ChemistrySelect* **8**, e202300379 (2023).
49. M. A. Alam, A. Jahan, E. Suzuki, H. Yashiro, *Engineering Reports* e12750 (2023).
50. A. Agneaux, M. H. Plouzennec, L. Antoni, J. Granier, *Fuel Cells* **6**, 47−53 (2006).
51. R. L. Borup, N. E. Wanderborgh, *Mater. Res. Soc. Symp. Proc.* **393**, 151−155 (1995).
52. M. C. Li, C. L. Zeng, S. Z. Luo, J. N. Shen, H. C. Lin, C. N Cao, *Electrochim. Acta* **48**, 1735−1741 (2023).

Chapter 4

Corrosion Behavior of Aluminum in Fluoride Ion Containing Sulfuric Acid Solution Through Immersion Process

Chapter 4: Corrosion Behavior of Aluminum in Fluoride Ion Containing Sulfuric Acid Solution Through Immersion Process

4-1 Introduction

Aluminum (Al) is considered one of the most promising materials for transformation applications for its special qualities of low density, low cost, and light weight.[1] Corrosion is more than just an inevitable natural phenomenon; its impact is felt in three areas of concern, namely economics, safety, and environmental damage. Metallic corrosion, seemingly innocuous, affects many sectors.[2] The consequences of corrosion are many and varied, and the effects of these on the safe, reliable, and efficient operation of equipment or structures are often more serious than the simple loss of a mass of metal.[3]

Al and its alloys, however, are reactive materials and are prone to corrosion.[4] Al generally exhibits passive behavior in aqueous solutions due to the formation of a strong and compact adherent passive oxide film on the surface, which affects corrosion susceptibility. The adhesive passivating surface oxide film is amphoteric, and consequently, the metal is readily dissolved when exposed to aggressive acidic and alkaline solutions. In fact, the corrosion of metallic materials in an acidic solution causes considerable costs.[5,6] Previous reports have focused on the corrosion characteristics of Al in weak acid media (hydrochloric acid, sulfuric acid.[7,8] aqueous alkaline solutions[9,10]and neutral dilute salt solutions (for instance, halide media [11,12]) and sodium sulfate solution.[13]

The Al, which is stable in a wide range of electrolytes, can undergo intense localized attack in the presence of chloride and bromide ions. The behavior of Al in sodium fluoride and sodium sulfate electrolytes is very different to that observed with Cl^- and Br^- solutions. Here, the attack seems to be more general in nature, with the net result being a gradual destabilization of the oxide film, which is less protective than the original oxide film. Therefore, the corrosive behavior of Al in pure water or water containing trace amounts of fluoride or sulfate ions particularly at low concentration levels[14-16] is an important issue, but only limited research has been found in such an environment. That's why it was our interest to study the influence of the fluoride and sulfate anion on the stability of films formed on Al in sodium fluoride and sulfuric acid media through immersion process.

4-2 Experimental Section

4-2-1 Materials and Methods

Al having a thickness of 1 mm and area of 6 cm^2 were used as the test pieces for immersion process. The test pieces were dipped into the PTFE cells containing around 90 cm^3 of test solution with different composition for a certain period.

4-2-2 Immersion conditions with test solutions

The test solutions for the immersion process were 2.5×10^{-6} M H_2SO_4 (pH 5.41), 5×10^{-6} M H_2SO_4 (pH 5.14), 2.5×10^{-6} M H_2SO_4 + 2 ppm F^- (pH 5.57), 5×10^{-6} M H_2SO_4 + 2 ppm F^- (pH 5.45) and 2 ppm F^- (pH 6.00) solutions using reagent grade of H_2SO_4 and NaF. The test pieces were polished by emery paper 4/0, 6/0, 1200 and 2000, then rinsed and immersed in around 90 cm^3 of aqueous solutions for 24 h, 48 h, 72 h, 96 h and 120 h at 80° C.

4-2-3 Electrochemical test

The open circuit potential (OCP) of as polished Al was measured under different test solutions at 80° C. The OCP was conducted for 1 hour with using a saturated calomel electrode (SCE) as reference electrode and the test specimens as working electrode system.

4-2-4 Surface Roughness Measurement

The surface roughness of the test specimens before and after immersion in the test solutions was observed and analyzed by atomic force microscope (AFM, NX-10).

4-2-5 Surface Morphology Analyses

The surface morphology of the test specimens through scanning electron microscopic (SEM) images and elemental analyses by energy dispersive x-ray (EDX) spectroscopy before and after immersion was taken by FE-SEM. The used machine was JSM-7800F keeping an accelerating voltage of 10 kV and 10.00 mm of working distance.

4-3 Results and Discussion

4-3-1 Open Circuit Potential

The open circuit potential (OCP) of pure as-polished Al was measured for a period of 1h under different test solutions at 80° C. The specific experimental results are shown in **Fig. 1.** It can be seen from **Fig. 1** that the open circuit potential of as-polished Al was lowest for 2 ppm F^- and highest for 2.5×10^{-6} M H_2SO_4 among the test solutions. At the same time, with increasing the concentrations of acid solutions as well as by the addition of fluoride ions with acid media, the value of the OCP increases. Thus, OCP results suggest that SO_4^{2-} ions are less aggressive than F^- ions which means the corrosion tendency gets lower with higher potential in the case of 2.5×10^{-6} M H_2SO_4 solution.

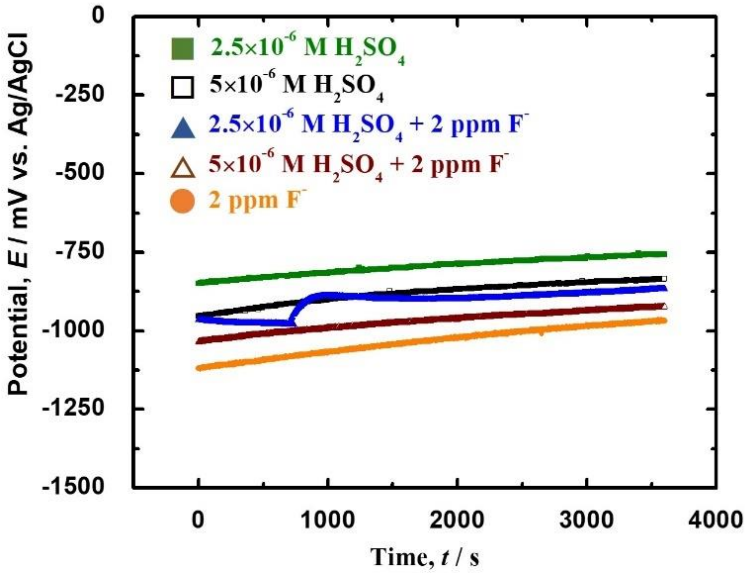

Fig. 1 Open circuit potential of pure as-polished Al under the test solutions at 80° C.

4-3-2 Amount of corrosion after immersion process

The test specimens were kept in the test solutions for immersion process under the certain period. As a result of the immersion test, the mass after the test increased in all the test pieces with different solutions. The amount of corrosion was calculated as a function of immersion time in different test solutions which is shown in **Fig. 2**. Firstly, the amount of corrosion was increased with increasing of the concentration of sulfuric acid. As higher concentrations of sulfates implied a higher

concentration of Al^{3+} ions in the aqueous environment, the reduction reactions on the cathode are catalyzed, which, in turn, accelerates oxidation reactions, thereby producing an increase in the corrosion rate and increased more after the addition of 2 ppm F^- ions in the acid solutions. From the results found in this study, it is concluded that pure as-polished Al undergoes a severe corrosion in sodium fluoride whereas sulfate ions form much lower corrosion as well as act as inhibitor when Al is used as bipolar plate in the PEMFC environment.

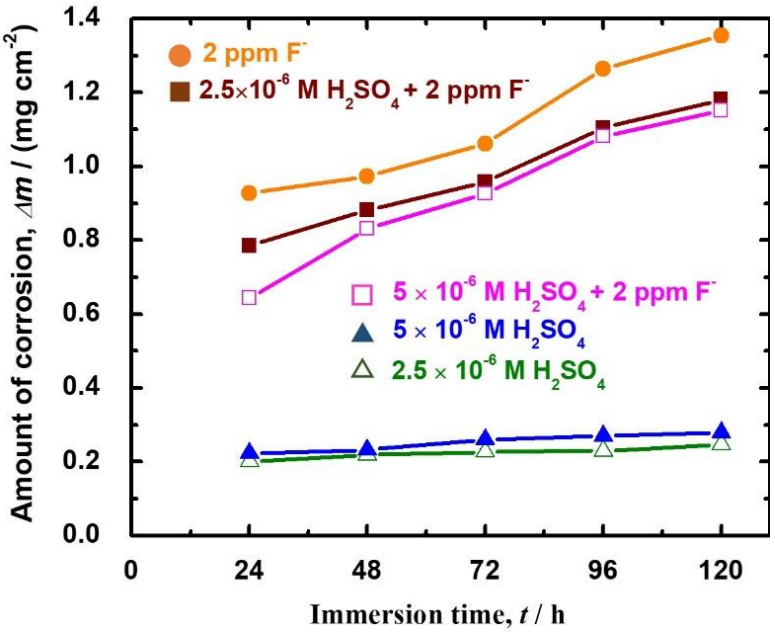

Fig. 2 Amount of corrosion as a function of immersion time in different solution.

4-3-4 Surface Roughness Analyses

The AFM images of pure as-polished Al before and after immersion in different test solutions for 120 h at 80° C are shown in **Fig. 3**. The images show the surface roughness of the test samples which indicates the corrosion behavior in the different solutions before and after immersion. The results reveal that the surface becomes smoother in case of sulfate ions and rough surfaces are found in the fluoride containing solutions.

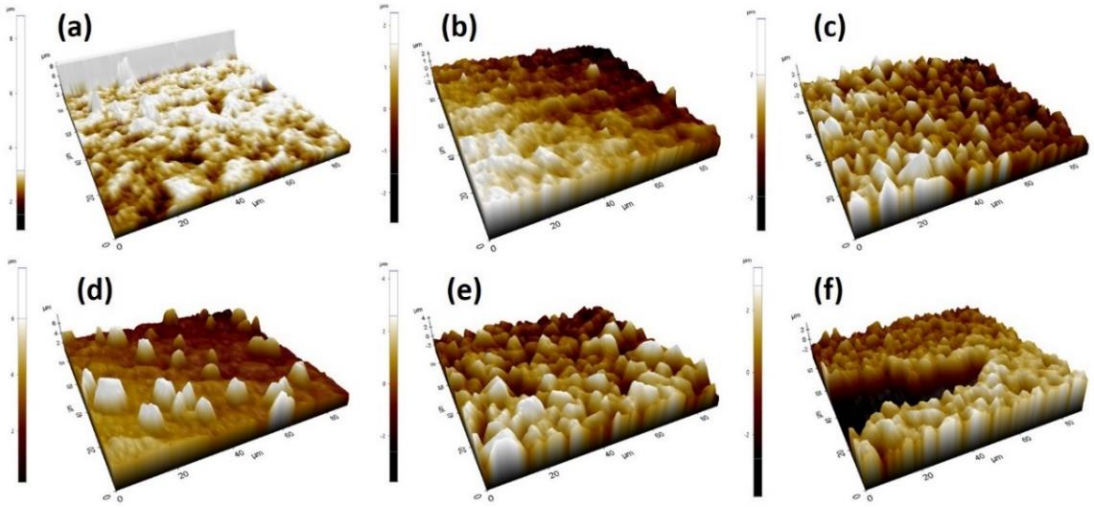

Fig. 3 Surface roughness of pure as-polished Al (a) before and after immersion in (b) 2.5×10^{-6} M H_2SO_4, (c) 5×10^{-6} M H_2SO_4, (d) 2.5×10^{-6} M H_2SO_4 + 2 ppm F^-, (e) 5×10^{-6} M H_2SO_4 + 2 ppm F^- and (f) 2 ppm F^- solutions for 120 h.

Additionally, the surface roughness data reveal that the more amount of fluoride ions, the more roughness was formed in the surface of the test specimens because of the formation of oxide layer which is shown in **Table 1**.

Table I. Average surface roughness of pure as-polished Al before and after immersion in different test solutions.

	Before immersion	After immersion				
Test solutions	**As-polished**	**2.5×10^{-6} M H_2SO_4**	**5×10^{-6} M H_2SO_4**	**2.5×10^{-6} M H_2SO_4 + 2 ppm F^-**	**5×10^{-6} M H_2SO_4 + 2 ppm F^-**	**2 ppm F^-**
Average roughness, *Ra* (μm)	**0.823**	**0.645**	**0.797**	**0.861**	**1.070**	**1.118**

4-3-5 Surface Morphology and Elemental Compositions

Fig. 4 shows the scanning electron micrograph of as-polished Al before and after immersion in different solutions for 120 h at 80° C where the surface is observed with some cubic precipitates on the Al surfaces tested in the solution containing 2.5×10^{-6} M H_2SO_4, 2.5×10^{-6} M H_2SO_4 + 2 ppm F^-, 5×10^{-6} M H_2SO_4 + 2 ppm F^- and 2 ppm F^-. It can be attributed to the Al oxide, which is

crystallized on the surface. The SEM images of as-polished Al in solution of 5×10^{-6} M H_2SO_4 showed a cloudy and little cracks pattern with some trace of white patches for almost in all the sample surfaces.

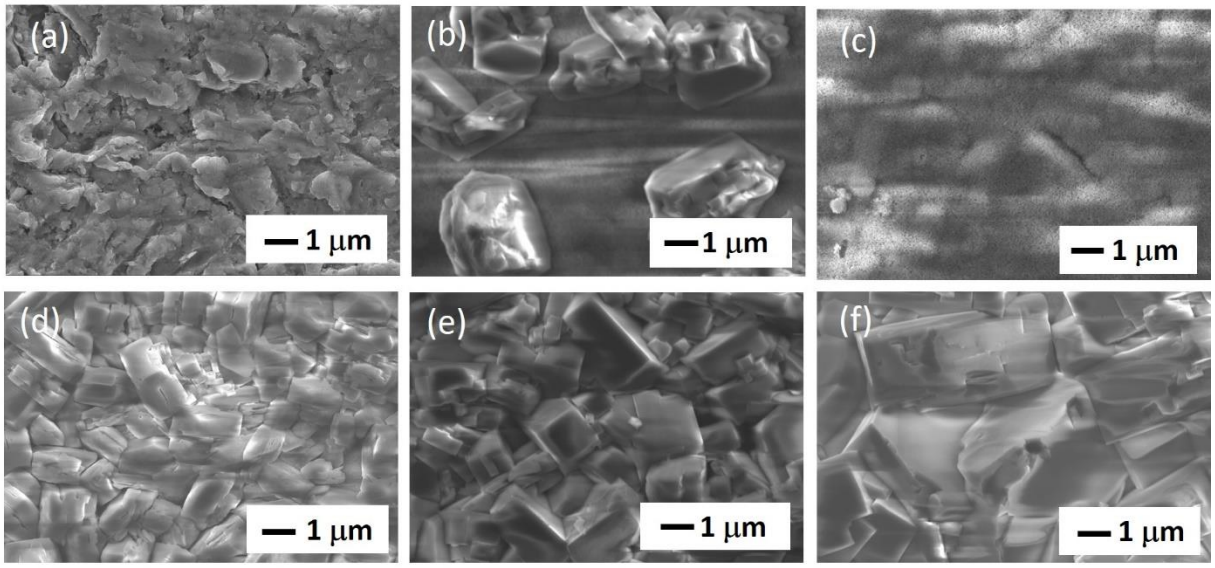

Fig. 4 SEM images of pure as-polished Al (a) before and after immersion in (b) 2.5×10^{-6} M H_2SO_4, (c) 5×10^{-6} M H_2SO_4, (d) 2.5×10^{-6} M H_2SO_4 + 2 ppm F^-, (e) 5×10^{-6} M H_2SO_4 + 2 ppm F^- and (f) 2 ppm F^- solutions for 120 h.

The EDX spectra and images shown in **Fig. 5** described the characteristic signals of as-polished Al after immersion in 5×10^{-6} M H_2SO_4 and 5×10^{-6} M H_2SO_4 + 2 ppm F^- solutions for 120 h, in addition to other elements, such as oxygen and sulfur, which are common as corrosion products of Al in sulfuric acid when a complex of type $Al_2(SO_4)_3(H_2O)_n$ is formed.[16] In case of 5×10^{-6} M H_2SO_4, the atomic percent ratio of carbon, oxygen, Al, sulfur and fluorine are 4.83, 66.29, 28.77 and 0.11, respectively were found which is shown in **Fig. 5(a)**. In addition, in the case of 5×10^{-6} M H_2SO_4 + 2 ppm F^- solution, the atomic percent ratio of carbon, oxygen, Al, sulfur and fluorine are 9.07, 68.16, 22.67, 0.01 and 0.09, respectively were found where extra fluorine atoms are

present which is shown in **Fig. 5(b)**. Thus, it reveals that the mild and severe corrosion occurred in the presence of sulfate and fluoride ions, respectively present in the solutions.

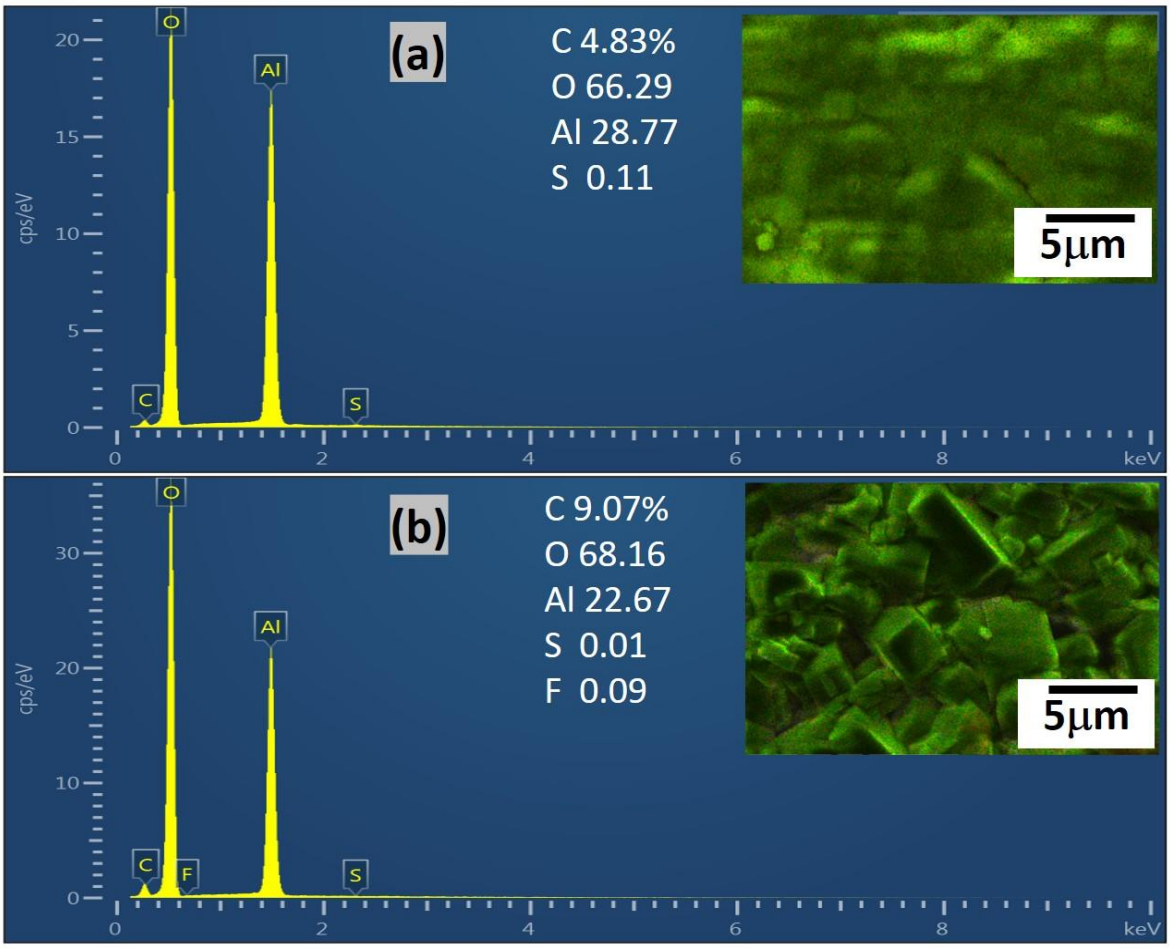

Fig. 5 EDX data and their related atomic percentages of pure as-polished Al after immersion in (a) 5×10^{-6} M H_2SO_4 and (b) 5×10^{-6} M H_2SO_4 + 2 ppm F^- solutions for 120 h.

4-4 Conclusion

Al is known as one of the most promising alternatives to use in different metallic sectors. Here, corrosion behavior of pure Al in sulfuric acid with sodium fluoride media through immersion process at 80° C was studied and the significant results were observed. It was found that the corrosion rate was increasing with increasing the acid concentration as well as through addition of fluoride ions in the acid solutions. On the contrary, the only sulfate ions from the acid solutions work to slow down the corrosion rate even sometimes act as corrosion inhibitors. Thus, it is

suggested and concluded that the rule of fluoride ions and sulfate ions are as corrosion accelerator and inhibitor, respectively. Therefore, it should be taken the special consideration when Al is used for various purposes in different areas.

References

1. D. Y. Li, Y. X. Shi, H. P. Xu, Y. Chen, P. Zhou, X. W. Li, W. X. Feng and S. P. Wang, *Int. J. Electrochem. Sci.* **13**, 9346 (2018).
2. V. S. Sastri, Green Corrosion Inhibitors, Theory and Practice. John Wiley & Sons, Inc., New Jersey, (2011).
3. O. R. Adetunji, P. O. Aiyedun, O. J. Alamu, A. S. Surakat, *J Eng Technol Res.* **3,** 292–297 (2011).
4. V. Mountarlier, M. P. Gigander, B. Normand, J. Pagetti, J. *Corros. Sci*. **47**, 937 (2005).
5. S. A. Umoren, O. Ogbobe, I. O. Igwe, E. E. Ebenso, *Corros. Sci.* **50**, 1998–2006 (2008).
6. A. Y. Musa, A. H., Kadhum, A. B Mohamad, M. S. Takrif, E. P. Chee, *Curr. Appl. Phys.* **12**, 325–330 (2012).
7. J. P. Dasquet, D. Caillard and E. Conforto, *Thin Solid Films* **371**, 183 (2000).
8. I. V. Aoki, M. C. Bernard and C. D. Torresi, *Electrochim. Acta* **46**, 1871 (2002).
9. J. Zhang, M. Klasky and B. C. Letellier, *J. Nucl. Mater*. **384**, 175 (2009).
10. M. Lashgari and A. M. Malek, *Electrochim. Acta* **55**, 5253 (2010).
11. Z. Bo, L. Ying and F. Wang, *Corros. Sci*. **51**, 268 (2009).
12. E. Mccafferty, *Corros. Sci.* **45**, 1421 (2003).
13. S. G. Wang, H. J. Huang, M. Sun, K. Long and Z. D. Zhang, *J. Phy. Chem. C* **119**, (2015).
14. K. Ishii, R. Ozaki, K. Kaneko and M. Masuda, *J. Jpn. Inst. Light Metals* **56**(2), 82–87 (2006).
15. K. Ishii, R. Ozaki, K. Kaneko and M. Masuda, *J. Jpn. Inst. Metals* **70**(10), 845–848 (2006).
16. S. Nomura, *Bulletin of the Jpn. Inst. Metals* **3**(3), 116–126 (1964).

Chapter 5

Stability and Inhibition Effect of Methyl-1H-Benzotriazole onto Aluminum in Deaerated Fluoride-Sulfate Solution

Chapter 5: Stability and Inhibition Effect of Methyl-1H-Benzotriazole onto Aluminum in Deaerated Fluoride-Sulfate Solution

5-1 Introduction

Due to outstanding mechanical and technological characteristics such as strength-to-volume ratio,[1,2] high specific strength and stiffness, good corrosion resistance, recyclability, and minimal costs in comparison to other materials, Al and its alloys are typically used as a structural material in several industrial applications, especially in the aerospace industry.[3, 4] However, materials of Al and its alloy are more responsive materials and prone to localized corrosion appropriately dissociation of the intermetallic particles within their grain boundaries.[5-7] Aluminum (Al) also has comparatively high corrosion resistance in atmospheric environments and needs less protection than other metals except in high and low pH environments.[8] We know that the reactivity of Al is very high due to the formation of a thin oxide protecting compact film layer such as Al oxide (i.e., Al_2O_3) on the Al surface that can easily prevent further corrosion.[9, 10]

Nowadays, with the rapid growth and development of modern technologies, diverse categories of techniques such as anodizing, plasma electrolytic oxidation, coatings, natural compounds that are used as green corrosion inhibitors, and applications of inhibitors (organic or inorganic) have been widely used to minimize the corrosion rate of Al and its alloys in different environments.[11-19] Among these, one of the most effective techniques to inhibit corrosion of Al and its alloys is conventional chrome conversion coatings. However, over the last decades, numerous studies have emphasized that this type of chrome conversion coating is detrimental to human health and hazardous to the environment.[20-24] To improve this situation, it is obligatory to develop chromate-free corrosion inhibitors. Therefore, subsequently, after various decades of research, it was experimentally demonstrated that, organic corrosion inhibitors with high inhibition efficiency are one of the most promising techniques to remarkability minimize the corrosion rate of metals and alloys in different aqueous solution.[25] In addition to this, inhibition is the utmost widespread protection method due to its less toxicity, eco-friendliness, strong chemical activity, comparatively cheapness compared to inorganic inhibitors, shows equally cathodic and anodic characters, special affinity to metal surfaces, biodegradable characteristics, ability to be used in relatively low concentrations, and, after all, better film-forming ability due to the rapid adsorption onto the metal surfaces.[26-28] Indeed, organic inhibitors include several electron donor heteroatoms in their

structure, such as nitrogen (N), phosphorus (P), sulfur (S), oxygen (O), and electrons, that form quickly a thick protective film that does not allow further oxidation on metals and guards the surface of the metal from acidic environments.[29-33] Especially, they can easily interact with the surface of the metal *via* interactions amid empty orbitals and electrons of the benzene rings and have all types of adsorption mechanism capability.[34-39] Based on their inhibition properties, the performance of adsorption is the utmost issue with an organic corrosion inhibitor. A wide range of possible organic inhibitors have been extensively applied for protecting metal and its alloys from corrosion.[40-43]

In recent years, numerous investigators have focused on the fact that nitrogen-containing triazole and its derivatives are important class of five-membered heterocyclic compounds that have been abundantly tested both experimentally and theoretically as effective corrosion inhibitors typically for metals and their alloys because of their extraordinary variety of properties and applications.[44-49] They can easily produce an insoluble protective film layer *via* interaction of organic inhibitors with metal on the metal surface, which prevents metal dissolution and can also significantly reduce the rate of corrosion by producing a metal-triazole complex. Along with their attractive molecular constitutions, they are readily soluble in acidic media.[50] Although the inhibition properties of the heteroatoms (S, N, and O) containing triazole and its derivatives have been well-documented for different metals and alloys, few information has been found for their adsorption criteria and durability of adsorbed layer on metals, particularly for Al.[51-53] Thus, it is considered that there is no example of investigating the influence and effect of methyl-1H-benzotriazole on the corrosion behavior of Al in deaerated fluoride-sulfate solution.

Therefore, the object of our current effort is to investigate the durability and inhibition mechanism of methyl-1H-benzotriazole on Al through immersion for certain period in sulfate fluoride solution at 80 °C by using different electrochemical and analytical techniques.

5-2 Materials and methods

5-2-1 Materials used in this study

The Al (99+%) collected from the Nilaco Corporation, Tokyo was used as the test materials for the immersion process in this study and denoted as the test samples. The Al was cut into pieces of 1 mm of thickness and 6 cm^2 of area. The tests samples were polished using emery paper with the

grit of 40/0, 60/0, 1200 and 2000, rinsed with acetone, and dipped into the PTFE cell contained of 100 cm^3 test solutions.

5-2-2 Solutions preparation for immersion process

The immersion of the test materials was performed in different solutions such as 0.1 ppm F^-, 0.1 ppm F^- + 0.1 ppm SO_4^{2-}, DSW, 0.1 ppm SO_4^{2-}, 0.1 ppm F^- + 0.5 ppm SO_4^{2-}, and 0.1 ppm F^- + 1 ppm SO_4^{2-} solutions for 24, 72 and 120 h at 80 °C without and with Me-BTA as inhibitor under deaerated environment using Ar gas and glove box. All solutions were prepared using Na_2SO_4 and NaF with analytical grade, purchased from Wako Pure Chemical Industries and Kanto Chemical Company Industries, respectively, Japan. Methyl-1H-benzotriazole (Me-BTA), a standard analytical-grade chemical with a purity of 99.98% was used (0.1 mM) as the organic inhibitor with the above prepared solutions in this study to lessen and protect the surface of the test samples from the corrosion. The structural formula of Me-BTA is shown in **Fig. 1**. The pH of the test solutions without and with Me-BTA was measured and disclosed in **Table 1.**

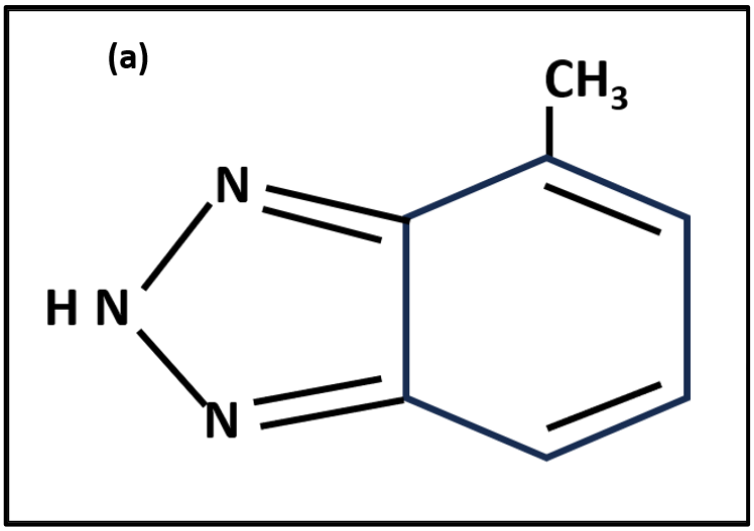

Fig. 1 Structural formula of the studied Methyl-1H-benzotriazole (Me-BTA) compound used in this study.

Table 1. pH of the test solutions without and with Me-BTA.

Solution	pH					
Inhibitor	0.1 ppm F^-	0.1 ppm F^- + 0.1 ppm SO_4^{2-}	DSW	0.1 ppm SO_4^{2-}	0.1 ppm F^- + 0.5 ppm SO_4^{2-}	0.1 ppm F^- + 1 ppm SO_4^{2-}
Without Me-BTA	5.78	5.72	6.3	5.72	5.66	5.62
With Me-BTA	6.34	6.12	5.87	5.41	5.25	5.13

5-2-3 Optical micrographic images

The microscopic images of the test samples were taken after immersion in the test samples without and with Me-BTA *via* Olympus metallurgical microscope (U-IF550, BX60M, Japan).

5-2-4 Weight loss and corrosion rate measurement

The weight of the test specimens was measured after immersion in the test solutions without and with 0.1 mM of Me-BTA at 80 °C in deaerated environment using Ar gas following the typical weight loss measurement.[54] The experiments were repeated at least three times, and the average values were taken. The corrosion rate, C_R (mm y^{-1}) also was calculated using the following Equation given by Fontana.[55]

$$\text{Corrosion rate, } C_R \text{ (in mm y}^{-1}) = \frac{87.6W}{\rho A t} \quad \text{--------- (1)}$$

Where W represents as the weight loss of the sample (in mg), *A as* the surface area (in cm^2), *t* as the immersion time (72h), and ρ as the density of Al (in g cm^{-3}).

After calculating the corrosion rate without and with Me-BTA as inhibitor it was seen that the inhibitor showed greater efficiency. The inhibition efficiency was calculated using the following Equation.[56]

$$\text{Inhibition efficiency, } \eta_{WL} = \frac{\text{Corrosion rate} - \text{Corrosion rate (inh)}}{\text{Corrosion rate}} \times 100 \quad \text{------ (2)}$$

where corrosion rate and corrosion rate (inh) mean without and with inhibitor (Me-BTA), respectively. All the tests and weight loss measurement were made at least three times under the same conditions and mean of the results was used.

5-2-5 Atomic force microscopy

The surface roughness of the test samples after immersion in the test solutions without and with Me-BTA was evaluated by atomic force microscopic (AFM) data using AFM machine (Park Systems, NX-10).

5-2-6 Scanning electron microscopy and EDX data

The surface morphology and elemental composition of the test samples upon exposure to the studied solutions were investigated using field emission scanning electron microscope (SEM) machine (JSM-7800FPRIME) and EDX microanalysis system. The SEM and EDX measurement were performed using 10 mm of working distance and 10 kV of accelerating voltage.

5-3 Results and discussion

5-3-1 Change of optical micrograph after immersion.

Optical micrographs (OM) of Al after 24 h of immersion in different test solutions such as 0.1 ppm F^-, 0.1 ppm F^- + 0.1 ppm SO_4^{2-}, DSW, 0.1 ppm SO_4^{2-}, 0.1 ppm F^- + 0.5 ppm SO_4^{2-}, and 0.1 ppm F^- + 1 ppm SO_4^{2-} solutions at 80 °C without and with Me-BTA are revealed in **Fig. 2** and **Fig. 3**, respectively. The optical micrographs evidenced that a mechanism of corrosion was occurred on the surface of Al without and with Me-BTA. From the micrographs, the test samples showed slight damage; no crack or hole was present, but a porous passive layer was obvious on the surface of Al, which intitles general corrosion products. The lower corroded area was found in case of the presence of the inhibitor Me-BTA.

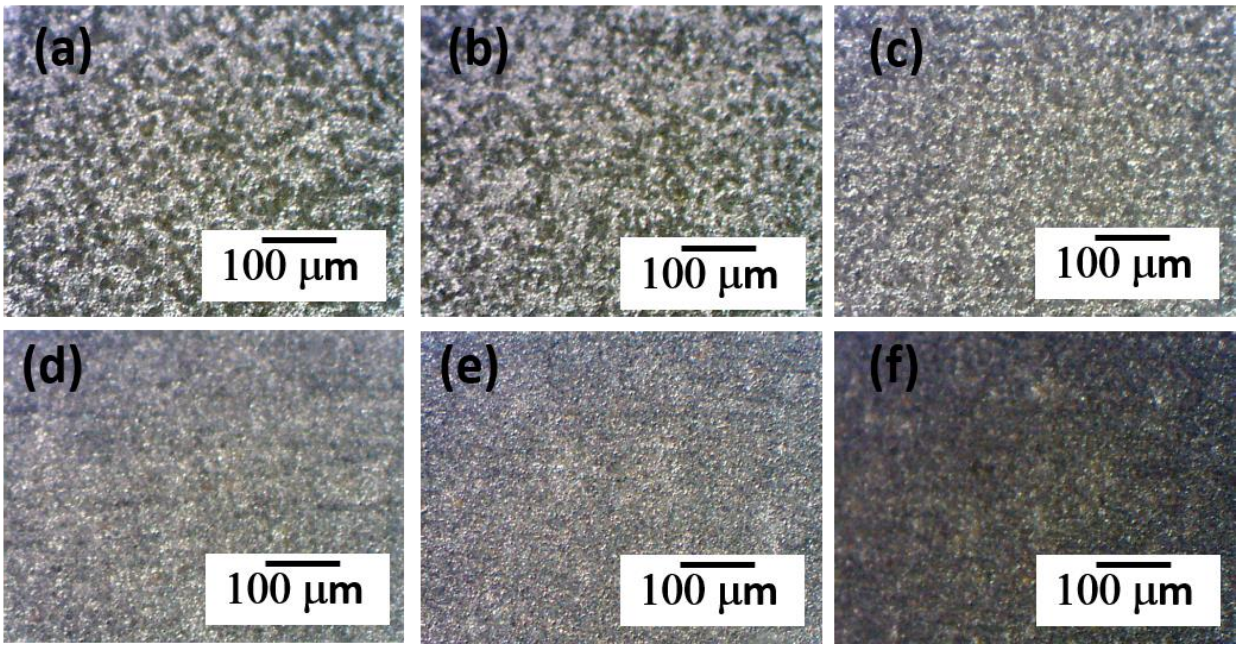

Fig. 2 Microscopic images of Al after immersion in (a) 0.1 ppm F^-, (b) 0.1 ppm F^- + 0.1 ppm SO_4^{2-}, (c) DSW, (d) 0.1 ppm SO_4^{2-}, (e) 0.1 ppm F^- + 0.5 ppm SO_4^{2-}, and (f) 0.1 ppm F^- + 1 ppm SO_4^{2-} solutions for 24 h at 80 °C without Me-BTA.

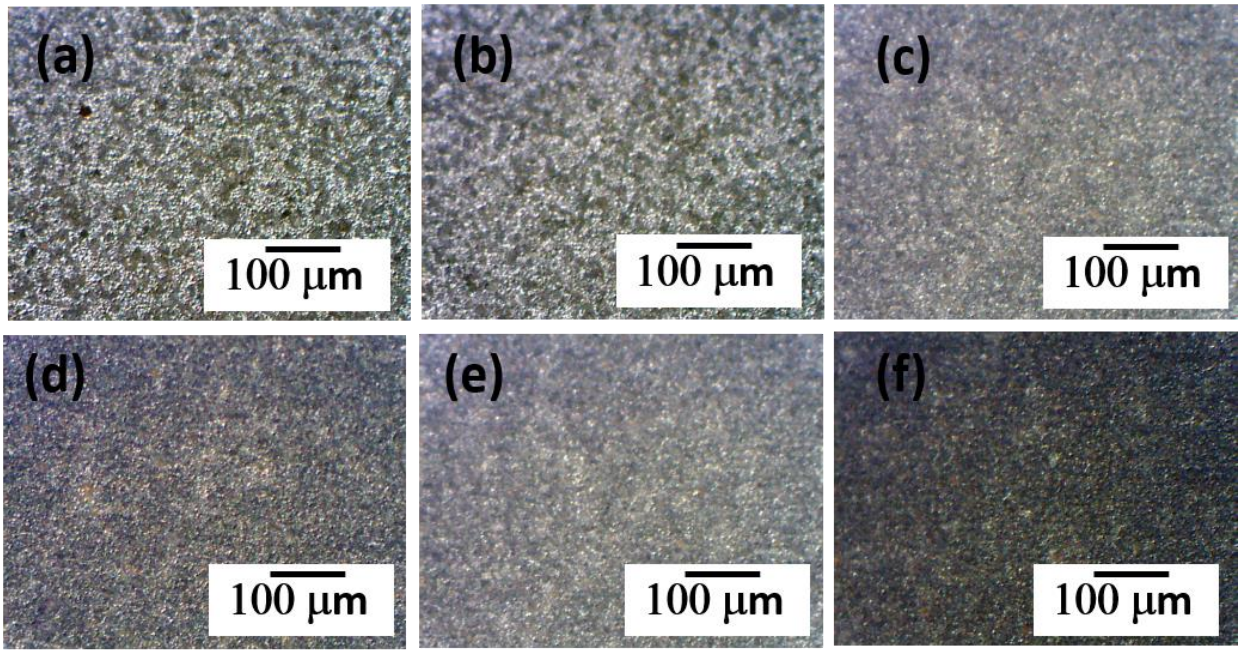

Fig. 3 Microscopic images of Al after immersion in (a) 0.1 ppm F^-, (b) 0.1 ppm F^- + 0.1 ppm SO_4^{2-}, (c) DSW, (d) 0.1 ppm SO_4^{2-}, (e) 0.1 ppm F^- + 0.5 ppm SO_4^{2-}, and (f) 0.1 ppm F^- + 1 ppm SO_4^{2-} solutions for 24 h at 80 °C with Me-BTA.

5-3-2 Mass change with immersion time.

The mass changes of Al in several experimental solutions were measured as a function of the exposure time for 24, 72 and 120 h without and with Me-BTA used as inhibitor. The outcomes attained are presented in **Fig. 4.** From these outcomes, for both cases the mass changes (weight loss) of the test samples for all solutions increase with the exposure time. The recorded mass changes in overall experimental period are the utmost for test samples that exposure in absence of any inhibitor. We also observe that mass changes were higher without Me-BTA addition as compared to that for the addition of 0.1 mM Me-BTA in the test solutions. This result implies that, dissolution of Al in sulfate containing fluoride test solutions in absence of Me-BTA was higher as compared to that of in the presence of Me-BTA. Thus, it is considered that This may be the existence of pre-immersion hydrate Al oxide (Al_2O_3) on the surface of the test samples.

The corrosion rate of test samples after immersion in different test solutions for 24 h at 80 °C without and with Me-BTA were calculated using equation 1 and shown in **Fig. 5.** The results show that corrosion rate was higher in case of fluoride ions and lower in case of sulfate ions as well as the additional sulfate ions in the fluoride solutions. The corrosion rate was 0.1249- and 0.0563-mm y^{-1} in case of 0.1 ppm F^- and 0.1 ppm F^- + 1 ppm SO_4^{2-} solutions, respectively in absence of Me-BTA. In addition, the corrosion rate was decreased with the presence of inhibitor used in the

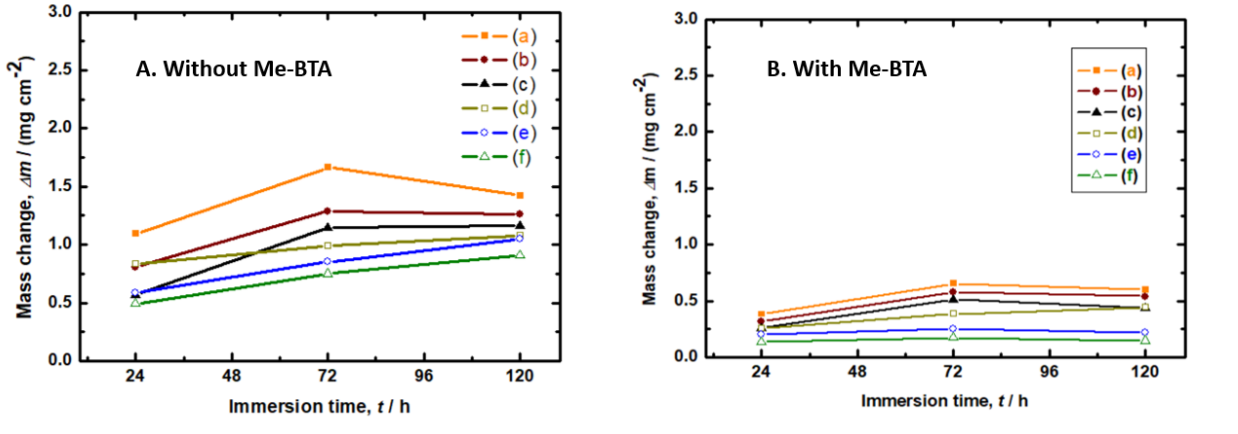

Fig. 4 Mass change of Al after immersion in (a) 0.1 ppm F^-, (b) 0.1 ppm F^- + 0.1 ppm SO_4^{2-}, (c) DSW, (d) 0.1 ppm SO_4^{2-}, (e) 0.1 ppm F^- + 0.5 ppm SO_4^{2-}, and (f) 0.1 ppm F^- + 1 ppm SO_4^{2-} solutions for 24 h at 80 °C without and with Me-BTA.

research. Thus, the corrosion was found as 0.0563- and 0.0131- mm y^{-1} in case of 0.1 ppm F^- + 1 ppm SO_4^{2-} solution without and with Me-BTA, respectively. Therefore, it is suggested that Me-BTA was successfully worked and adsorbed on the surface of Al based materials and performed as a good inhibitor.

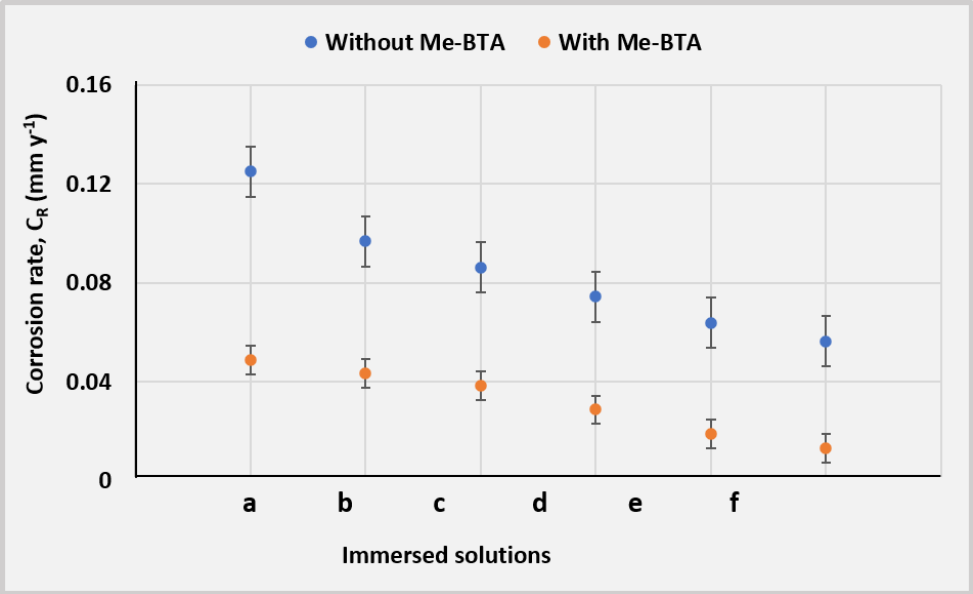

Fig. 5 Corrosion rate, C_R of Al after immersion in (a) 0.1 ppm F^-, (b) 0.1 ppm F^- + 0.1 ppm SO_4^{2-}, (c) DSW, (d) 0.1 ppm SO_4^{2-}, (e) 0.1 ppm F^- + 0.5 ppm SO_4^{2-}, and (f) 0.1 ppm F^- + 1 ppm SO_4^{2-} solutions for 24 h at 80 °C without and with Me-BTA.

5-3-3 Surface roughness analysis.

Atomic force microscopy (AFM) was used to evaluate the surface roughness of the test samples after immersion in different test solutions without and with Me-BTA. After corrosion examination of Al without and with Me-BTA in the fluoride-sulfate-containing solution, the AFM techniques were used to expose the progress of the surface ground. The topography is revealed in **Fig. 6**. In case of the uninhibited solution for the presence of corrosion products such as $Al(OH)_3$, the Al surfaces of the test samples are relatively higher with the presence of some large hills like structures. Whereas, comparatively smoother or flat surfaces with only small hills are seen in case of the inhibited solution.

Moreover, we know that surface roughness is a vital aspect of detecting the corrosion performance of the test samples. The roughness values, R_a obtained from the AFM topography are listed in **Fig.**

7. These values designate that the high percentage of oxygen significantly enlarged the surface roughness of the test samples than that of the uninhibited surface. It would be reasonable to expect that the low surface roughness was existing due to the presence of hydrated Al oxide (Al_2O_3) on the Al surface with Me-BTA.

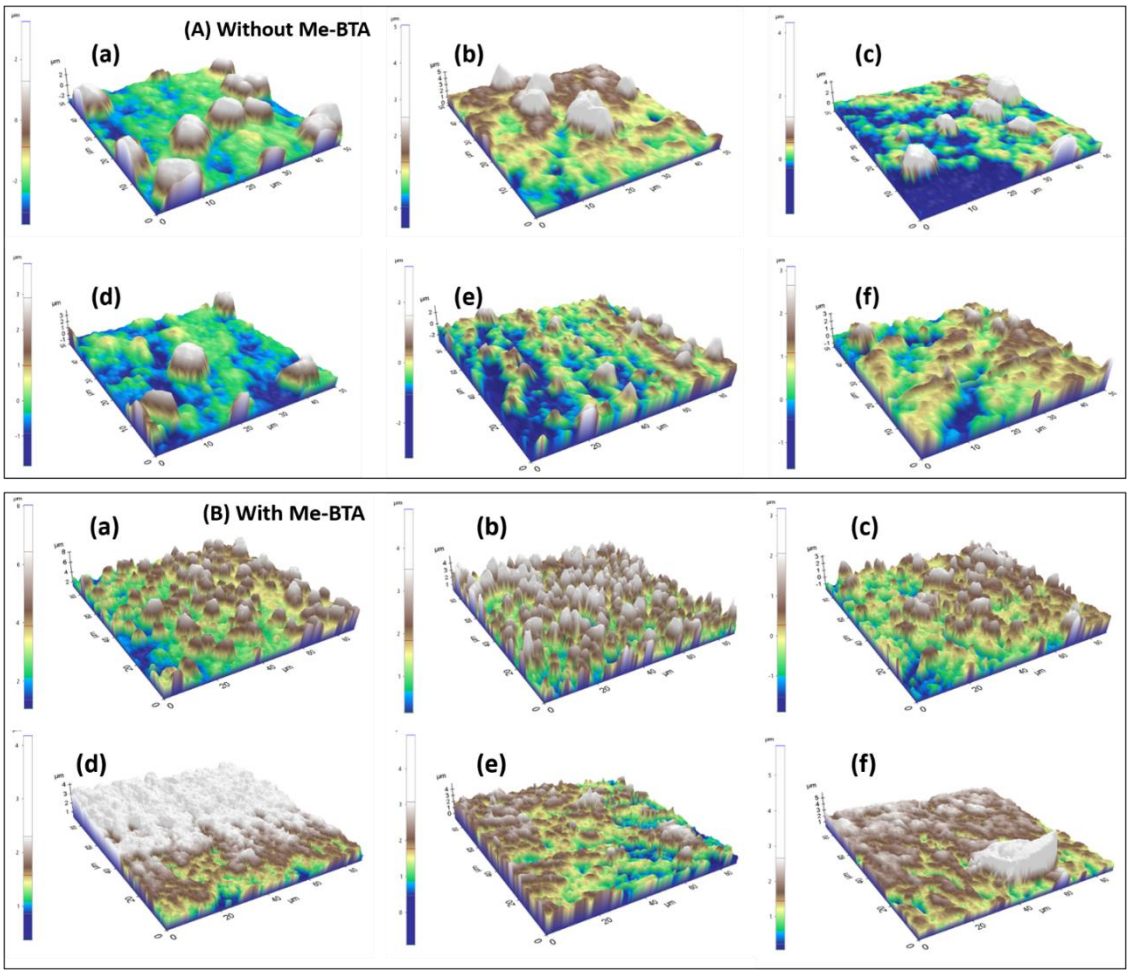

Fig. 6. AFM images of Al after immersion in (a) 0.1 ppm F^-, (b) 0.1 ppm F^- + 0.1 ppm SO_4^{2-}, (c) DSW, (d) 0.1 ppm SO_4^{2-}, (e) 0.1 ppm F^- + 0.5 ppm SO_4^{2-}, and (f) 0.1 ppm F^- + 1 ppm SO_4^{2-} solutions for 24 h at 80 °C (A) without and (B) with Me-BTA.

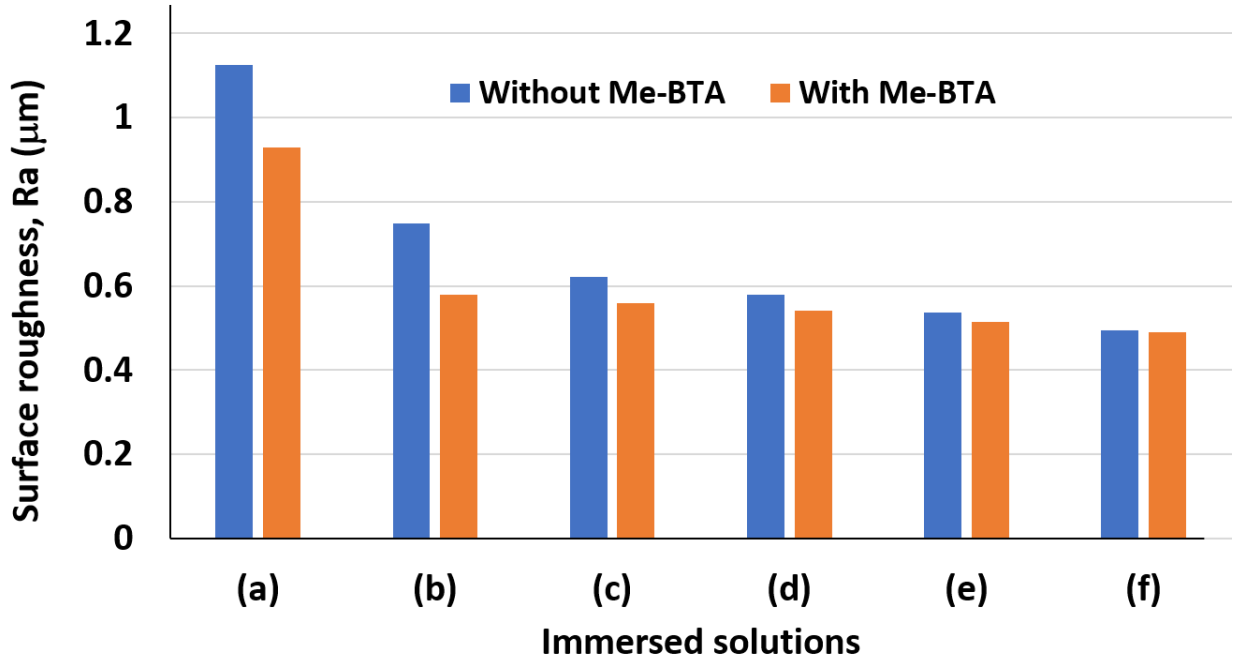

Fig. 7 Surface roughness values, *Ra* (μm) of Al after immersion in (a) 0.1 ppm F^-, (b) 0.1 ppm F^- + 0.1 ppm SO_4^{2-}, (c) DSW, (d) 0.1 ppm SO_4^{2-}, (e) 0.1 ppm F^- + 0.5 ppm SO_4^{2-}, and (f) 0.1 ppm F^- + 1 ppm SO_4^{2-} solutions for 24 h at 80 °C without and with Me-BTA.

5-3-4 Surface morphology by SEM images.

Fig. 8 and **Fig. 9** characterize the surface morphology images of all the test samples without and with Me-BTA using scanning electron microscope after exposure to the different concentrations of sulfate-containing fluoride solutions for 24 h at 80° C. As shown in **Fig. 8,** the SEM images of Al revealed some cubic structures as the corrosion products. These cubic structures like corrosion products gradually decreases and corrosion inhibition efficiency increases with the rising of concentration SO_4^{2-} ions which indicates the formation of Al oxide, which is crystallized on the surface of the test samples.

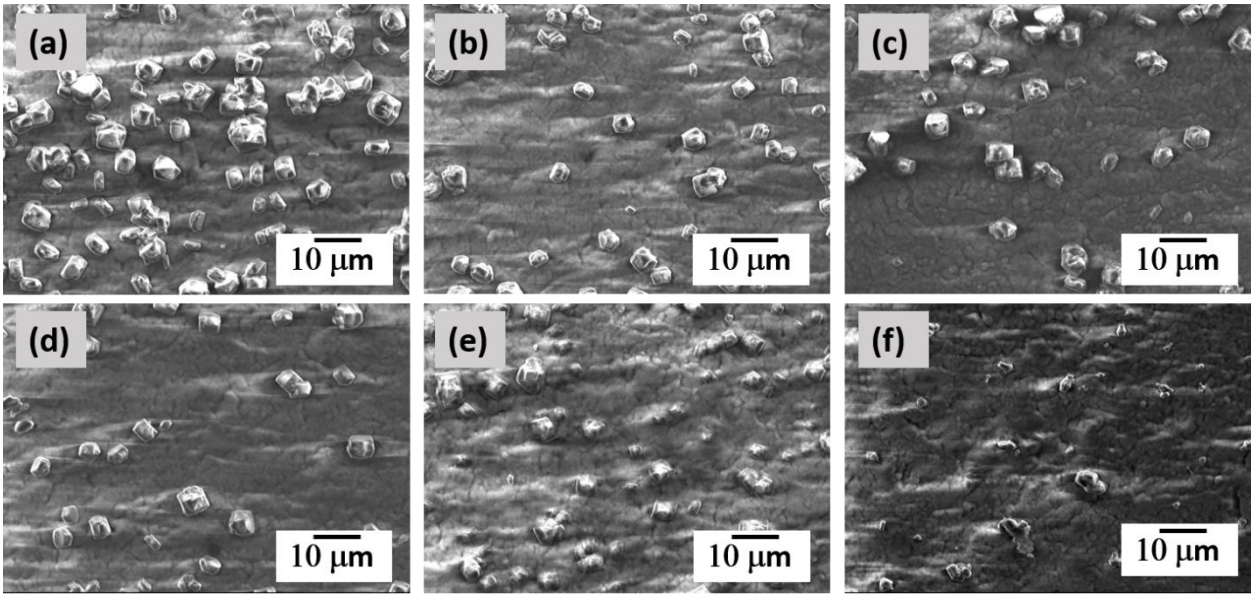

Fig. 8 SEM images of Al without Me-BTA in (a) 0.1 ppm F^-, (b) 0.1 ppm F^- + 0.1 ppm SO_4^{2-}, (c) DSW, (d) 0.1 ppm SO_4^{2-}, (e) 0.1 ppm F^- + 0.5 ppm SO_4^{2-}, and (f) 0.1 ppm F^- + 1 ppm SO_4^{2-} solutions immersed for 24 h at 80 °C.

On the contrary, **Fig. 9** shows the SEM images in the test solutions with Me-BTA where only small localized corrosion products were detected everywhere on the surface of the test samples. The results clearly show that after addition of the inhibitor Me-BTA, the surface converted towards smoother due to the formation of a protective film on the surface of the test samples. Besides, almost no corrosion products were seen on Al surface with higher concentration of sulfate ions such as 0.5 and 1 ppm SO_4^{2-} in the fluoride solution which indicates that the sulfate ion also acts as the inhibitor. Therefore, **Fig. 9**(f) revealed the maximum smoothness with no defected zone on the surface of the Al test samples with the addition of 0.1 mM of Me-BTA.

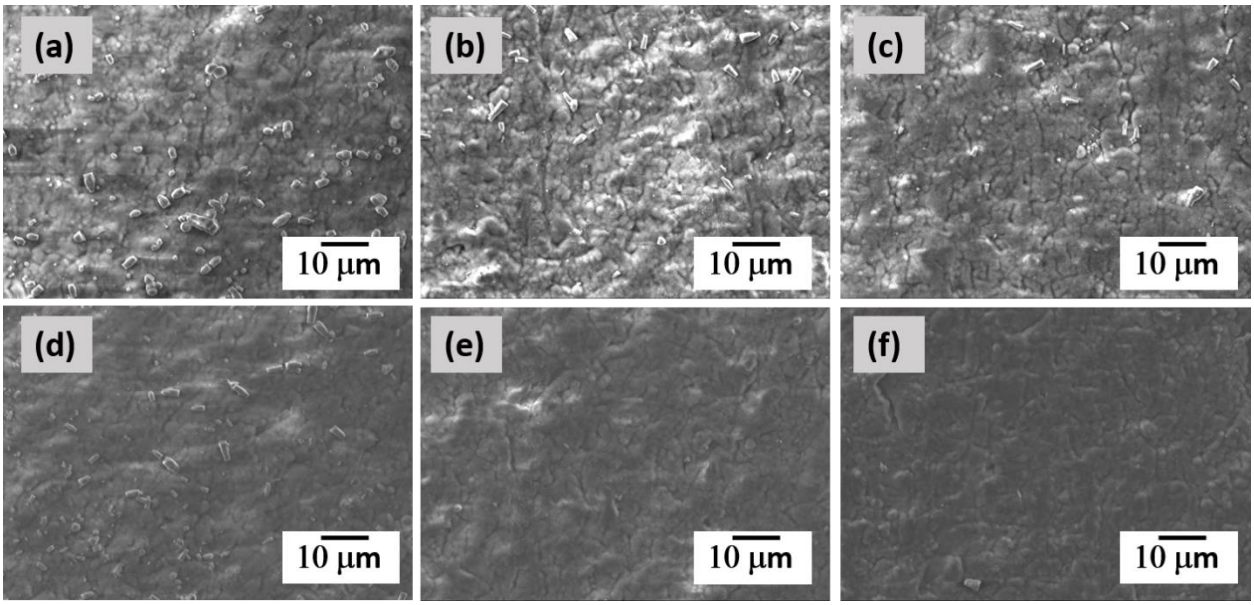

Fig. 9 SEM images of Al with Me-BTA in (a) 0.1 ppm F^-, (b) 0.1 ppm F^- + 0.1 ppm SO_4^{2-}, (c) DSW, (d) 0.1 ppm SO_4^{2-}, (e) 0.1 ppm F^- + 0.5 ppm SO_4^{2-}, and (f) 0.1 ppm F^- + 1 ppm SO_4^{2-} solutions immersed at 80 °C for 24 h.

5-3-5 Elemental composition analysis by EDX.

Fig. 10(A) and **Fig. 10**(B) show the EDX data of Al test samples after immersion in different test solutions without and with Me-BTA. The figures depict the elemental mapping images and compositions of Al test samples after immersion in sulfate ions containing fluoride solution such as 0.1 ppm F^- + 1 ppm SO_4^{2-} without and with Me-BTA. The distribution of Al, C, O, F, S, and N is distinguished by EDX mapping shown in **Table 2.** The EDX analysis confirms that the surface oxide layer was longer enriched with the presence of Al, C, O, F, and S elements upon exposure the Al test samples to the test solutions without Me-BTA.

Furthermore, **Table 2** reveals the elemental compositions with 65.61% of oxygen (O), which is very high and illustrates the attendance of corrosion products such as $Al(OH)_3$. [57, 58] On the other hand, the inhibitory compound Me-BTA absorbs over the Al substrate which seems to happen *via* contact between the N-containing Me-BTA and Al surface. Therefore, N and Al both can possibly contribute to inhibitor-oxide interactions. In addition, elemental compositions in **Table 2** showed the percentage of O is 55.04 which is lower because of the absence of Me-BTA of inhibition solution, demonstrating a low level of corrosion products on the surface of Al, Furthermore,

the presence of 20.85% C in **Fig. 10(B)** confirms the adsorption activities of the inhibitor molecule on the surface of Al test samples.

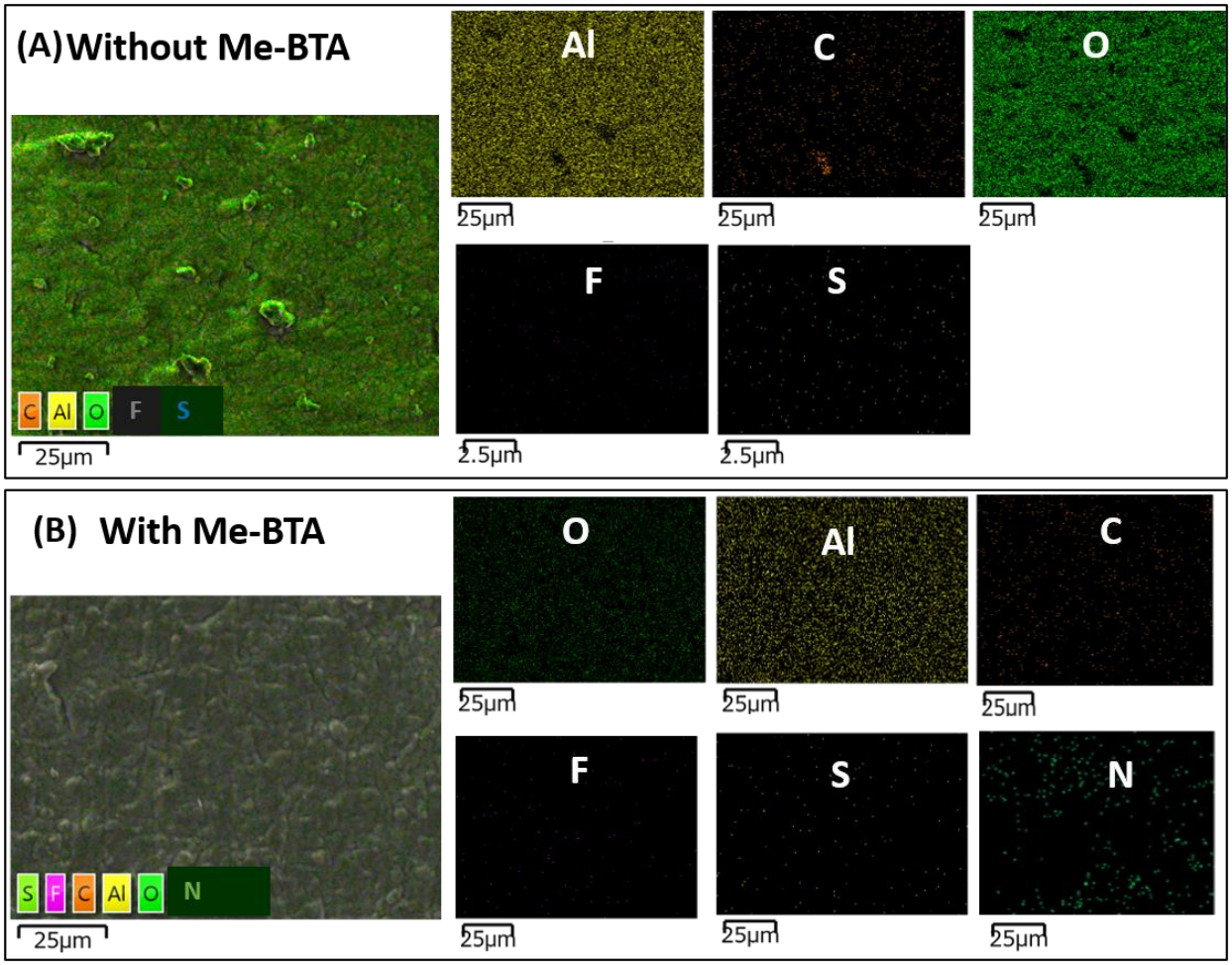

Fig. 10 EDX mapping of Al immersed in 0.1 ppm F^- + 1 ppm SO_4^{2-} solution for 24 h (A) without and (B) with Me-BTA.

Table 2. Elemental compositions of Al presented after immersion in 0.1 ppm F^- + 1 ppm SO_4^{2-} solution for 24 h at 80 °C without and with Me-BTA.

	Elemental composition by atomic %						
	O	**Al**	**C**	**S**	**F**	**N**	**Total**
Without Me-BTA	65.61	26.19	7.09	0.67	0.44	---	100
With Me-BTA	55.04	22.82	20.85	0.07	0.35	0.87	100

5-3-6 Mechanism of interaction of methyl-1H-benzotriazole (Me-BTA) with Al.

Fig. 11 depicts a tentative mechanism for the interaction of Me-BTA on Al surface by interacting with heteroatom (nitrogen) of Me-BTA used as inhibitor to induce the surface films or hypothetical obstruction complex layer after exposure in fluoride-sulfate solution. Nitrogen heteroatom containing Me-BTA molecule has electron clouds that perform as charge midpoints. These charge midpoints enable heteroatom nitrogen to produce weak electrostatic interactions such as Vander walls force with Al metal resulting in physical adsorption of Me-BTA molecule. Successive chemical and physical adsorption of Me-BTA molecule could result in an inhibitor complex layer or film. This inhibitor film or layer shows the performance as a fence against charge transfer such as better hydrophobicity. Furthermore, the protective layer between Me-BTA molecule and Al substrate surface could be different due to some essential factors such as the type of the studied solution, the chemical atmosphere, the type of charge on the surface, the density, the electrostatic contacts, and the chemical structure of the organic compound used in the study.[63] Therefore, the organic inhibitor creates chemisorption and coordination bonds by using their unpaired electrons present in the compound.

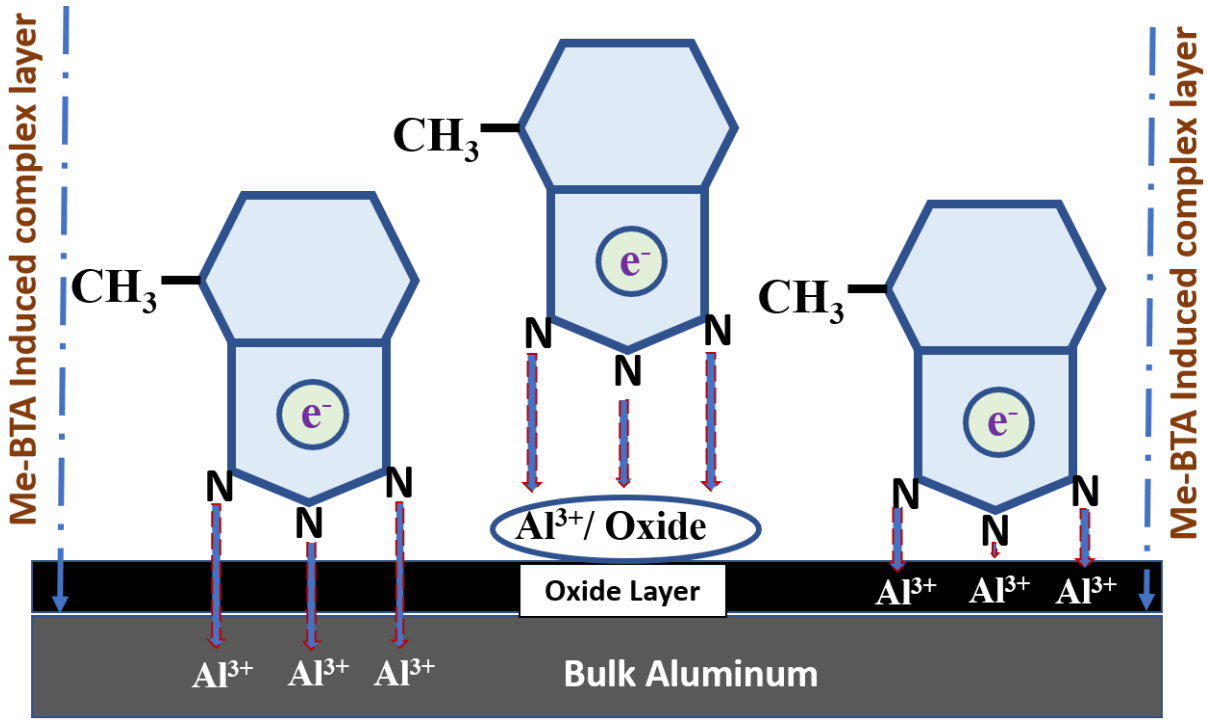

Fig. 11 Proposed shield mechanism for the interaction of methyl-1H-benzotriazole (Me-BTA) with Al.

5-4 Conclusion

Through physical and chemical adsorption on the surface of Al and its environment cause changes in its corrosion. The organic corrosion inhibitors that have environmentally friendly characteristics and can efficiently slow down the rate of corrosion of metallic substances. In this study, the corrosion behavior of Al in fluoride-sulfate solutions without and with the presence of organic corrosion inhibitor through immersion process was investigated. Here, organic corrosion inhibitor methyl-1H-benzotriazole was used onto Al to shield from corrosion. This research work has delivered deep understanding about the stability and mechanism of the inhibitor shielding film, up to 120 h of immersion. The microscopic, atomic force microscopic, scanning electron microscopic images and EDX data of the corrosion products were taken and analyzed. The following key points were deduced from this study.

- The corrosion rate was decreased and surface roughness was improved when methyl-1H-benzotriazole was used in the test solutions.
- The lower amount and smaller sizes of Al oxides as corrosion products were found on the surface of Al.

Thus, it is concluded that the stability and inhibition effect of methyl-1H-benzotriazole molecule on Al in fluoride-sulfate solutions was clearly understood where methyl-1H-benzotriazole showed significant corrosion protection activities and are thought to be more effective in other metallic substances.

References

1. P. Kwolek, *RSC Adv*. **10,** 26078–26089 (2020).
2. P. Kwolek, A. Pustuła, W.J. Nowak, *Surf. Coat. Technol.* **357**, 535–542 (2019).
3. S. Chen, C. Huang, C. Lin, *Corros Sci.* **184**, 109354 (2021).
4. R. Rosliza, W. B. Wan Nik, H. B. Senin, *Mater. Chem. Phys.* **107**, 281–288 (2008).
5. V. Mountarlier, M. P. Gigandet, B. Normand, et al. *Corros. Sci.* **47,** 937 (2005).
6. O. O. Joseph, O. O. Joseph, *Mater. Sci. Eng. C*. **1107**, 012170 (2021).
7. M. A. Alam, A. Jahan, E. Suzuki, H. Yashiro, *Eng. Rep.* e12750 (2023).
8. P. Kwolek, *RSC Adv.* **10,** 26078–26089 (2020).

9. A. K. Mishra, R. Balasubramanian, *Corros. Sci*. **49**(3), 1027–1044 (2007).
10. M. A. Alam, A. Jahan, E. Suzuki. H. Yashiro, *ChemistrySelect*, **8**, e202300379 (2023).
11. P. Kwolek, A. Pustuła, W. J. Nowak, *Surf. Coat. Technol*. **357**, 535–542 (2019).
12. R. Rosliza, W. B.W. Nik, H. B. Senin. *Mater. Chem. Phys.* **107**, 281**–**288 (2008).
13. O. O. Joseph, O. O. Joseph, *Mater. Sci. Eng.* **1107**, 012170 (2021).
14. G. Asan, A. Asan, *J. Mol. Struct.* **1201**, 127184 (2020).
15. M. P. Martínez-Viademonte, S. T. Abrahami, H. Theodor, B. Malte, T, Herman, *Coatings* **10**, 1106 (2020).
16. K. Xhanari, M. Finsˇgar, *Arab. J. Chem.* **12**, 4646–4663 (2019).
17. M. Niknahad, S. Moradian, S. M. Mirabedini, *Corros. Sci.* **52**(6), 1948–1957 (2010).
18. T. G. Harvey, *Corros. Eng. Sci. Technol.* **48**(4), 248–269 (2013).
19. S. S. Golru, M. M. Attar, B. Ramezanzadeh, *J. Ind. Eng. Chem.* **24**, 233–244 (2015).
20. X. F. Liu, *Corros. Sci.* **49**(9), 3494–3513 (2007).
21. Y. Ma, X. Zhou, G. E. Thompson et al., *Surf. Interface Anal.* **45**(10), 1479–1484 (2013).
22. N. Ogurtsov, A. A Pud, P. Kamarchik et al., *Synth. Met.* **143**(1), 43–47 (2004).
23. M. Finˇsgar, K. Xhanari, B. Petovar, *Microchem. J.* **147**, 863–871 (2019).
24. X. He, W. Li, H. Li, *J. Vac. Sci. Technol.* **14**(4), 2039–2047 (1996).
25. V. S. Sastri, John Wiley & Sons, (2012).
26. M. R. Jakeria, R. J. Toh, X. Chen et al., *J. Appl. Electrochem.* **52**, 1021–1044 (2022).
27. T. Zhang, S. Cao, H. Quan, et al., *Res. Chem. Intermed.* **41**, 2709–2724 (2013).
28. C. M. Fernandes, L. X. Alvarez, N. E. dos Santos et al., *Corros. Sci.* **149**, 185–194 (2019).
29. Q. Ma, S. Qi, X. He et al., *Corros. Sci.* **129**, 91–101 (2017).
30. J. Li, D. Chen, D. Zhang et al., *Colloids Surf, Physicochem. Eng. A.* **550**, 145–154 (2018).
31. M. Faisal, A. Saeed, D. Shahzad et al., *Corrosion Reviews* **36**, 507–545 (2018).
32. A. Nahlé, R. Salim, F. El Hajjaji et al., *RSC Adv.* **11**, 4147**–**416 (2021).
33. A. Ahmed, A. Amiery, A.B. Mohamad, et al., *Sci. Rep.* **12,** 4705**–**4726 (2022).
34. I. Elazhary, M.R. Laamari, A. Boutouil, et al., *Anti-Corros. Method* **66**, 544–555 (2019).
35. S. Deng, X. Li, X. Xie, *Corros. Sci.* **80**, 276–289 (2014).
36. C. Verma, M.A. Quraishi, A. Singh, *J Taiwan Inst Chem Eng.* **58,** 127–140 (2016).
37. M. A. Mostafa, M. Ashraf, Ashmawy, A. M. A. Reheim et al., *J. Mol. Struct.* **1236**, 130292 (2021).

38. T. Zhang, S. Cao, H. Quan et al., *Res. Chem. Intermed.* **41**, 2709–2724 (2013).
39. K. J. Lewis, J. Aklian, USA Patent, 1999.
40. A. Garner, USA Patent, 2014.
41. N. Nwaji, G. Fomo, J. Mack et al., *Electrocatalysis*, **10**(4), 445–458 (2019).
42. E. -S. M. Sherif, *J. Ind. Eng. Chem.* **19**, 1884–1889 (2013).
43. S. Zor, S. Sagdinç, *Prot. Met.* **50**, 244–253 (2014).
44. S. V. Lamaka, M. L. Zheludkevich, K. A. Yasakau, et al., *Electrochem. Acta* **52**, 72317247 (2007).
45. L. B. Coelho, D. Cossement, M. -G. Olivier, *Corros. Sci.* **130**, 177–189 (2018).
46. M. L. Zheludkevich, K. A. Yasakau, S. K. Poznyak, et al., *Corros. Sci.* **47**, 3368–3383 (2005).
47. T. Ma, B. Tan, L. Guo et al., *Mater. Sci. Eng.* **272**, 115330 (2021).
48. M. A. Mostafa, M. Ashraf, M. A. M. Ashmawy et al., *J. Mol. Struct.* **1236**, 130292 (2021).
49 K. S. Bokati, C. Dehghanian, *J. Environ. Chem. Eng.* **6**, 1613–1624 (2018).
50. S. Marcelin, N. Pébère, *Corros. Sci.* **101**, 66–74 (2015).
51. L. B. Coelho, M. Mouanga, M. -E. Druartet al., *Corros. Sci.* **110**, 143–156 (2016).
52. ASTM G1. Standard Practice for Preparing, Cleaning, and Evaluating Corrosion Test Specimens; ASTM, (1999).
53. M. G. Fontana, Corrosion Engineering. 3rd ed. Singapore: McGraw-Hill, International Ed; **171**, (1987).
54. A. Singh, K. R. Ansari, M. A. Quraishi et al., *J. Mol. Struct.* **1206**, 127685–127723 (2020).
55. B. G. Prakashaiah, D. V. Kumara, A. A. Pandith et al., *Corros. Sci.* **136**, 326–338 (2018).
56. F. M. Queiroz, M. Magnani, I. Costa et al., *Corros. Sci.* **50**, 2646–2657 (2008).
57. P. M. Niamien, H. A. Kouassi, A. Trokourey et al., *ISRN Mater. Sci.* **623754**, 1–15 (2012).
58. A. R. El-Sayed, M. M. El-Hendawy, M. S. El-Mahdy et al., *Sci. Rep.* **13**, 4812–483 (2023).

Chapter 6

Benzylphosphonic Acid Self-Assembled Monolayer onto Aluminium and Performance Evaluation for Use as Bipolar Plate in PEMFC

Chapter 6: Benzylphosphonic Acid Self-Assembled Monolayer onto Aluminium and Performance Evaluation for Use as Bipolar Plate in PEMFC

6-1 Introduction

Organic inhibitor compounds contain numerous electron donor heteroatoms in their structure, such as nitrogen (N), phosphorus (P), sulfur (S), oxygen (O), and electrons, that adsorb on the Al surface to form a thick, strong shielding film. [1,2] Since organics are not naturally friendly, they are very tough to recover and recycle due to the formation of complex compounds with metal. This not only causes a loss of economic energy but also consumes a lot of energy. In the unique circumstances of sustainable development to recover this serious issue, self-assembly technology is one of the most auspicious metal surface treatment systems due to its ease of operation[3] and low environmental pollution,[4] especially for aluminum (Al) and its alloys.[5]

The important merits of using self-assembled film are simple and flexible technology with little energy consumption, high wet adhesion to a metal surface, and nanoscopic molecular control and componential diversity.[6-9] Since organic phosphonic acid contains the organic functional group R in its structure, it can be expected not only as a corrosion-resistant coating but also as a primer that improves the adhesion of surface treatment layers through chemical bonding. Usually, a very common category of organic phosphonic acid molecules used in self-assembly processes consists of two parts: a hydrophilic head group and a hydrophobic tail.[10]

However, self-assembled monolayers of phosphonic acids have been interesting devotion and intensively studied because the phosphonic acid-based molecules can be easily formed into a highly dense and ordered film by the liquid phase method on various oxide surfaces including Al_2O_3.[11,12] The structures of the Benzylphosphonic acid compound used in this study is shown in **Fig. 1.**

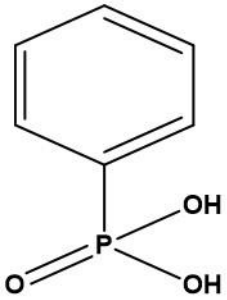

Fig. 1 Chemical structure of benzylphosphonic acid compound used in this study.

As shown in **Fig. 2**, organic phosphonic acid is chemically adsorbed by condensation with hydroxyl groups on the surface of Al and forms a self-assembled monolayer (SAM), thereby avoiding metal corrosion.

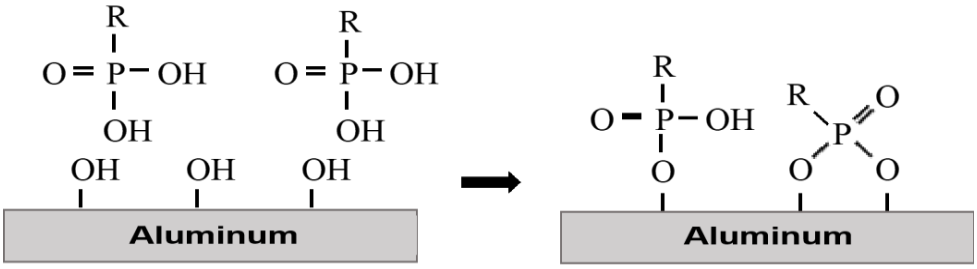

Fig. 2 Schematic diagram of SAM formation of organic phosphonic acid on Al.

Yet, the application of surface treatment with organic phosphonic acid to PEMFC separators has not yet been reported.

That's why in this present work we will try to investigate the mechanism of self-assembly adsorption of BPA on bare Al substrates, and the deposited film was characterized using several analytical techniques, as well as SEM, EDX, XPS, and contact angle, in order to examine the nature and thickness of the film for different deposition times.

6-2 Materials and methods

The Al, provided by the company of Nilaco, Japan, is used as a substrate in this present work. For the weight loss test, all Al coupons were cut with dimensions of 30 mm × 20 mm × 1 mm. All

chemicals are standard commercial grade and are used as received without further purification. The materials include benzylphosphonic acid (BPA, 97%, Sigma-Aldrich). 1 mM benzylphosphonic acid aqueous solution was prepared by dissolving 0.177 g of phenylmethyl phosphonic acid in 1 litter of DI water. All test samples were exposed to this 1 mM benzylphosphonic acid solution for several duration. The experimental method is expressed in the following way:

Dry polished by emery paper (4/0, 6/0, 1200 and 2000) and wet polished by Al paste

⬇

Cleaned with acetone in an ultrasonic bath each for 5min

⬇

Immersed in 1 mM benzylphosphonic acid solution for the duration of 0.1 h, 1h, 2h, 12h and 24h

⬇

Immersed in the simulated solutions at 80 °C for 24-120 h

⬇

Surface observation through microscopic, SEM, TEM, EDX and contact angle data

6-3 Results and discussion

6-3-1 Amount of corrosion

Fig. 3 depicts the amount of corrosion in several experimental solutions with exposure times of 24 h, 48 h, 72 h, 96 h, and 120 h without and with 24 h BPA treatment. This result suggested that the dissolution of Al in sulfate-containing fluoride test solutions in the absence of BPA was higher as compared to that in the presence of BPA. **Fig. 4** represents the mass changes of Al in 0.1 ppm F^- + 0.1 ppm SO_4^{2-}, solutions measured as a function of the exposure time for 24 h after BPA

treatment at different times (1, 2, 12, and 24 h). The results show that the corrosion rate gradually decreases with an increase in the immersion time of Al in BPA solution.

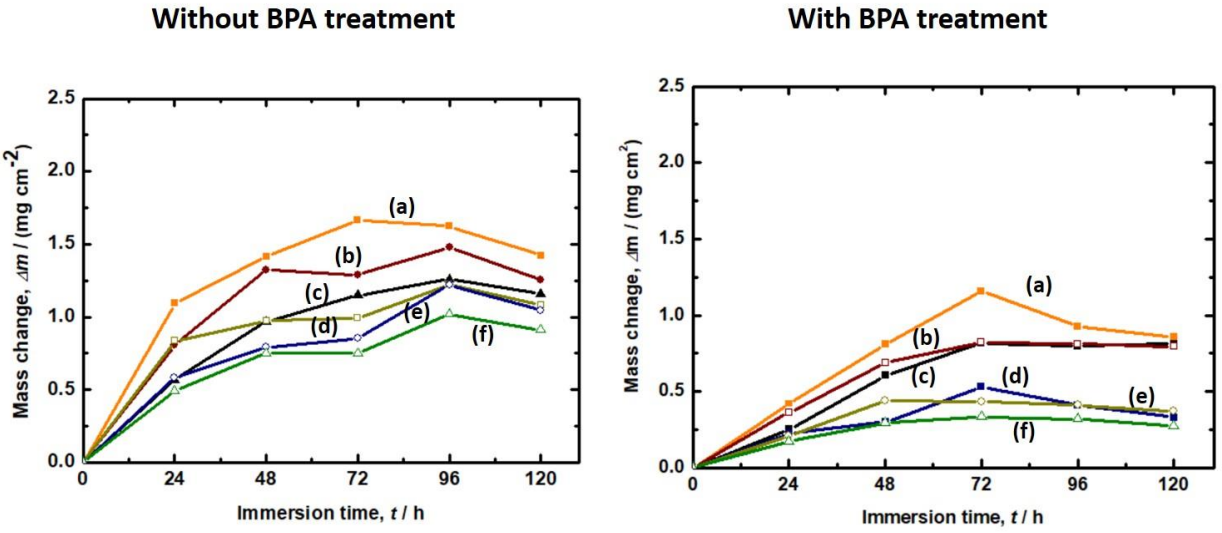

Fig. 3 Mass change of Al after immersion in (a) 0.1 ppm F^-, (b) 0.1 ppm F^- + 0.1 ppm SO_4^{2-}, (c) DSW, (d) 0.1 ppm SO_4^{2-}, (e) 0.1 ppm F^- + 0.5 ppm SO_4^{2-}, and (f) 0.1 ppm F^- + 1 ppm SO_4^{2-} solutions for 24 h at 80 °C without and with BPA.

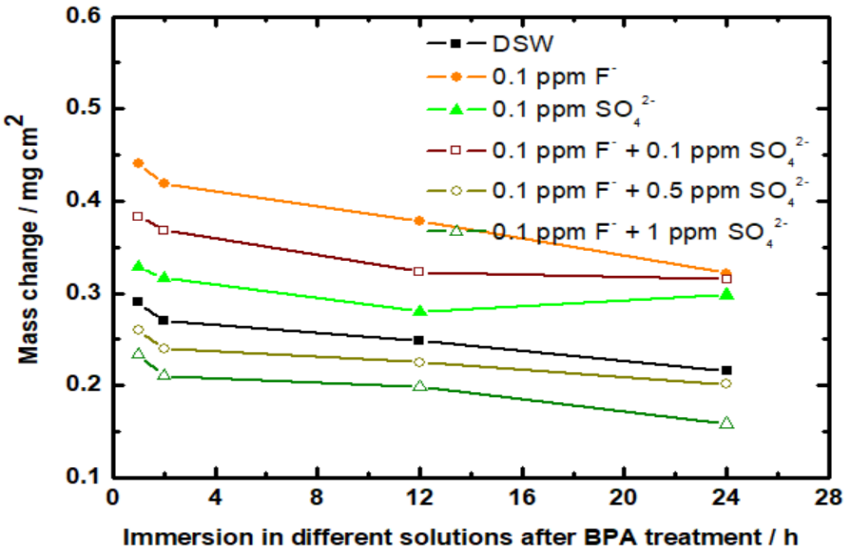

Fig. 4 Mass change of Al after 1, 2, 12, and 24 h of BPA treatment and immersion in different solutions for 24 h at 80 °C.

6-3-2 SEM and EDX data analysis

Fig. 5 characterizes the surface morphology images of the test samples after 1h of BPA treatment and immersion in different concentrations of fluoride and sulfate solutions for 24 h at 80°C using scanning electron microscope. **Fig. 6** characterizes of the test samples without and with 0.1, 1, 2, 12, and 24 h of BPA treatment and immersion in 0.1 ppm F^- + 0.1 ppm SO_4^{2-} solution for 24 h at 80 °C. As shown in **Fig. 5,** the SEM images of Al revealed cubic structures. These cubic structures as corrosion products were gradually decreased and corrosion inhibition efficiency increased with rising the concentration of SO_4^{2-} ions. These corrosion products are considered as Al oxides which are crystallized on the surface of the test samples. On the contrary, in the case of **Fig. 6,** after BPA treatment at different times such as 0.1, 1, 2, 12, and 24 h, the cubic structures as the corrosion products were gradually decreased. Finally, the surface of Al was smooth in case of 24 h of BPA treatment even almost no corrosion products were seen.

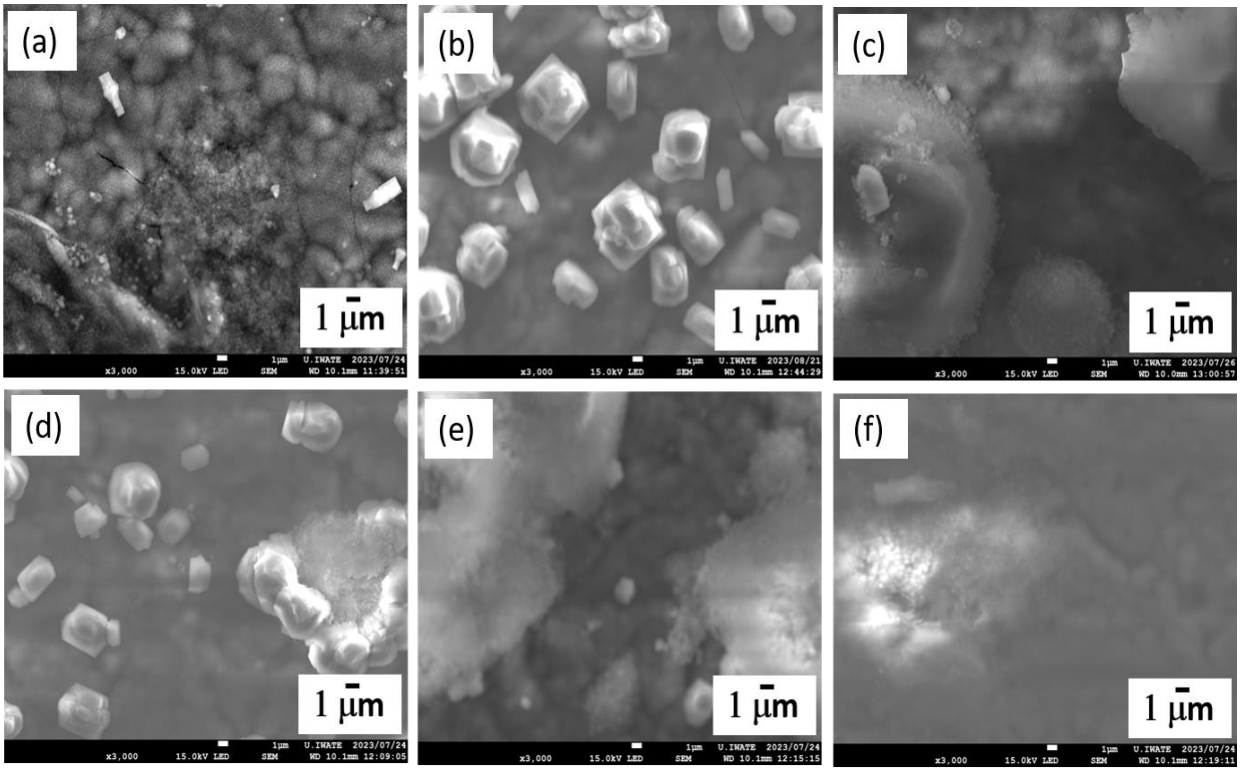

Fig. 5 SEM images of Al after 1h of BPA treatment and immersion in (a) 0.1 ppm F^-, (b) 0.1 ppm F^- + 0.1 ppm SO_4^{2-}, (c) DSW, (d) 0.1 ppm SO_4^{2-}, (e) 0.1 ppm F^- + 0.5 ppm SO_4^{2-}, and (f) 0.1 ppm F^- + 1 ppm SO_4^{2-} solutions immersed for 24 h at 80 °C.

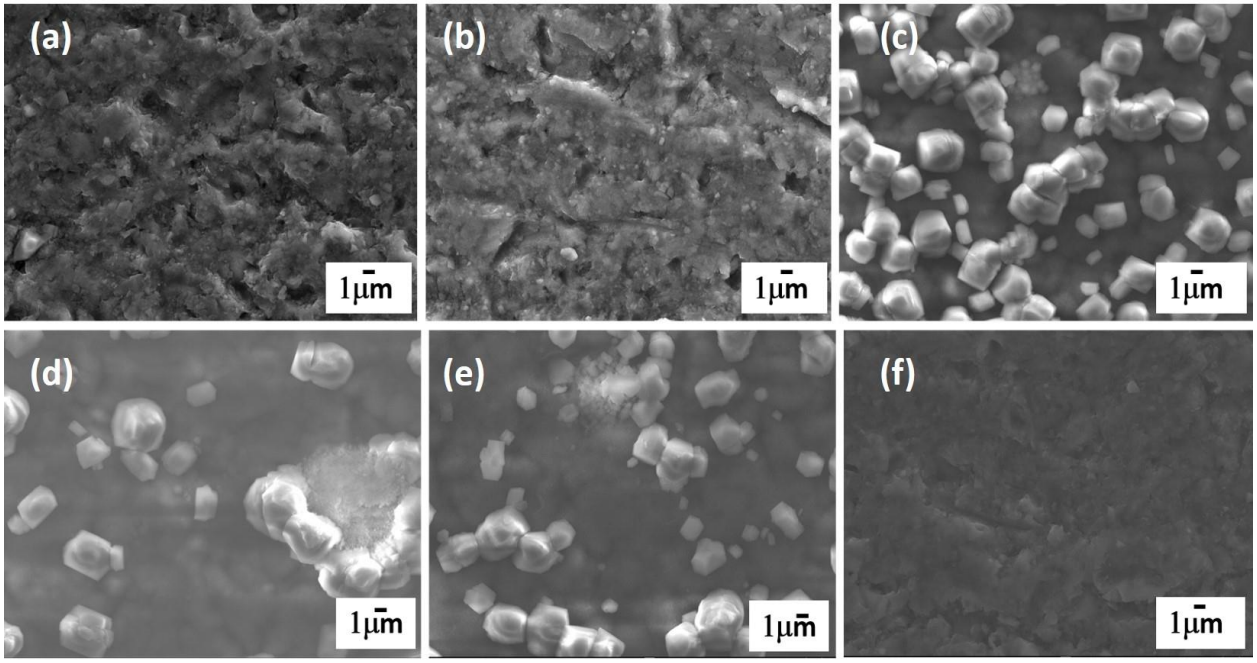

Fig. 6 SEM images of Al (a) without and with (b-f) 0.1, 1, 2, 12, and 24 h of BPA treatment and then 24 h of immersion in 0.1 ppm F^- + 0.1 ppm SO_4^{2-} at 80 °C.

The EDX test results of the self-assembled film after 1 h of BPA treatment and immersion in 0.1 ppm F^- + 0.1 ppm SO_4^{2-} solution for 24 h at 80°C are shown in **Fig. 7**. It is clearly observed that from there are some it is mainly contained the elements such as C, O, Al, and P. Compared with previous data in Chapter 3, where the percentage of oxygen (O) was 66% which was very high and illustrated the presence of corrosion products as $Al(OH)_3$. On the contrary, with the formation of self-assembled film on the Al surface, the percentage of oxygen is decreased by about 33.41%. To sum up, the change in element content confirmed the successful preparation of the self-assembled film by BPA.

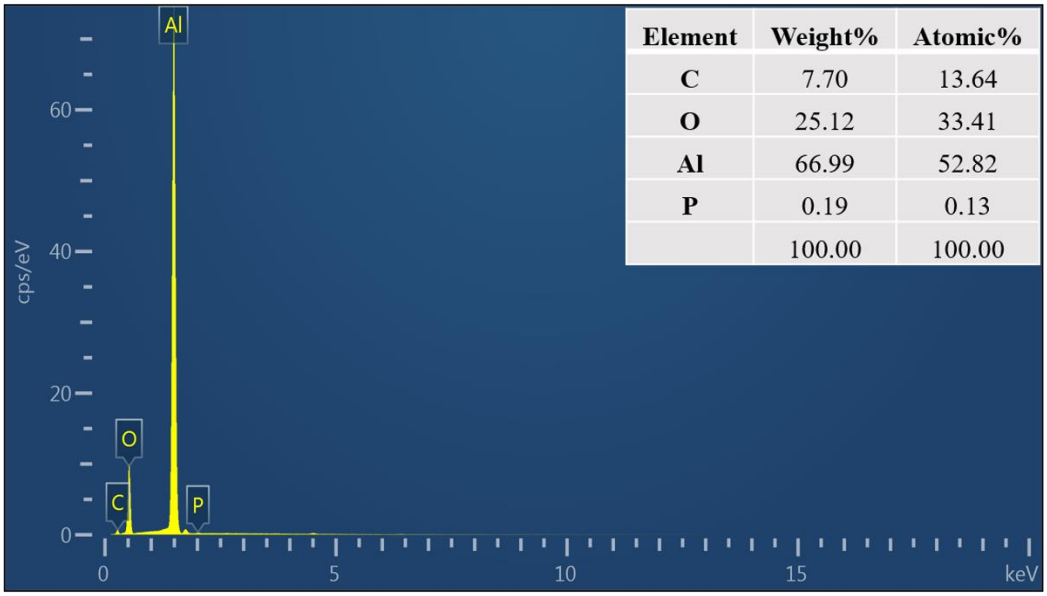

Element	Weight%	Atomic%
C	7.70	13.64
O	25.12	33.41
Al	66.99	52.82
P	0.19	0.13
	100.00	100.00

Fig. 7 EDX spectrum and elemental composition of Al after 1 h of BPA treatment and immersion in 0.1 ppm F^- + 0.1 ppm SO_4^{2-} solution for 24 h at 80°C.

The SEM images of Al without (a, b) and with (c, d) 1 h of BPA treatment and then immersion for 24 h at 80 °C in DSW and 0.1 ppm F^- are shown in **Fig. 8**. The results clearly show that after treatment with the inhibitor BPA, the surface converted towards smoother due to the formation of

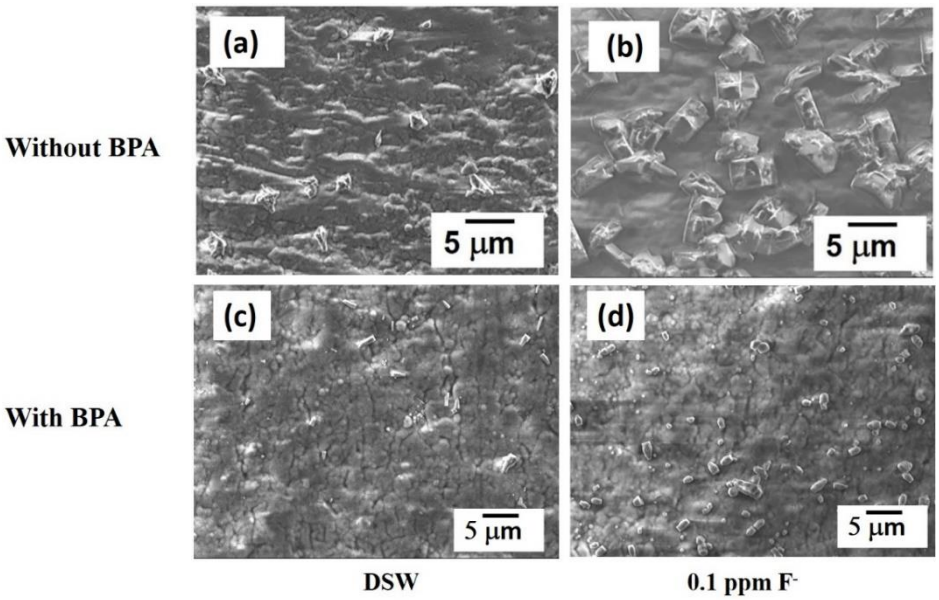

Fig. 8 SEM images of Al without (a, b) and with (c, d) 1 h of BPA treatment and then immersion for 24 h at 80 °C in DSW and 0.1 ppm F^- .

a protective self-assembled film on the surface of the test Al samples which indicates that the BPA can be used as corrosion inhibitors and improve the surface of Al when used as BP materials in PEMFC.

6-3-4 TEM analysis

Furthermore, the TEM pictures were taken to explore the thickness of the film on the surface of the Al after 24 h immersion in a 0.1 ppm F^- + 0.1 ppm SO_4^{2-} solution for 24 h at 80 °C after BPA treatment (0.1 h, 1 h, 2 h, 12 h, and 24 h). **Fig. 9** presents the variation of the film formed formation increases with increasing the assembly evolving time in BPA containing aqueous solution at 0.177 g/L with thicknesses of 35µm, 0.98 µm, 0.89 µm, 0.88 µm, and 0.67 µm, respectively. So, it is shown that, with increasing exposure time, the thickness of the film gradually decreases.

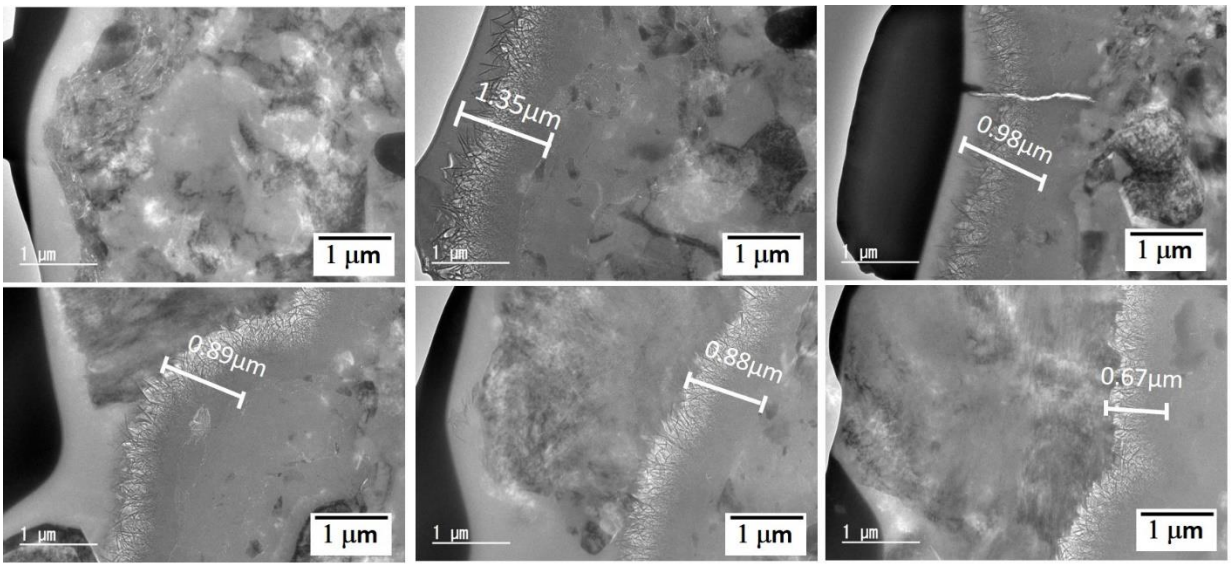

Fig. 9 TEM images of Al, 24 h immersion in 0.1 ppm F^- + 0.1 ppm SO_4^{2-} for 24h at 80 °C after BPA treatment (0.1h, 1h, 2h, 12h and 24h.

6-3-5 Contact angle data

The SEM surface attendance and corresponding contact angle images of Al samples without and with SAMs before and after BPA treatment and after immersion in the test solution are shown in **Fig. 10**. The surface images of the Al have a noteworthy change after self-assemble treatment by BPA. The presence of SAMs makes the Al sample surface smoother. In other words, the SAMs can

efficiently inhibit the corrosion of Al in fluoride-sulfate containing solution. From contact angle data we also further confirmed successful self-assembly of the self-assembled membrane. Additionally, the values of contact angles of Al after cleaning and washing were 65.4° but after 1 h in BPA treatment BPA contact angles rises to104.9° and 104.9° after (1h BPA treatment) 24 h immersion in 0.1 ppm F^- + 0.1 ppm SO_4^{2-} at 80 °C. It reveals that the hydrophobicity of Al surface is improved owing to the presence of SAMs which is beneficial to the corrosion protection of Al and some other materials.

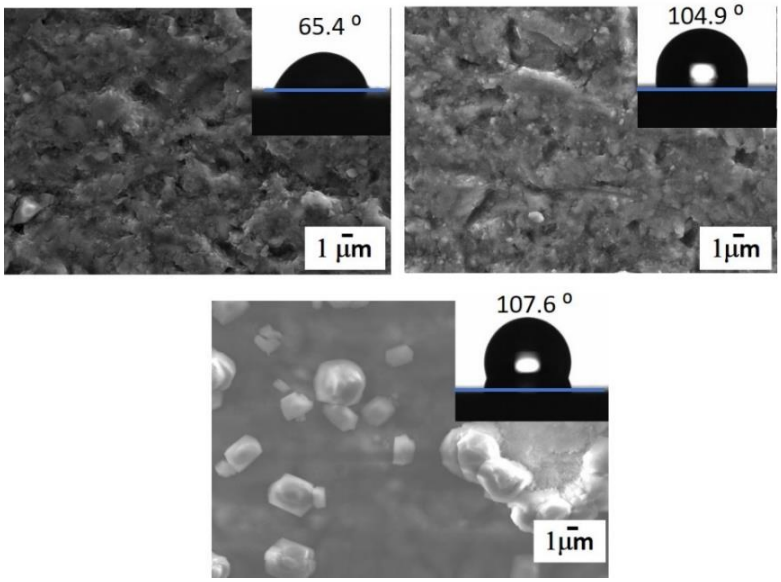

Fig. 10 The SEM surface morphology and contact angle pictures of Al samples without and with SAMs after BPA treatment and after immersion in test solution.

6-4 Conclusion

In this study, we illustration that BPA deposited onto Al in a self-assembly process. The inhibition result of BPA molecule on Al surface in fluoride sulfate containing solution, and depicted the resulting assumptions:

- The corrosion onto Al metal was measured through the adsorption of inhibitor organic molecules BPA also improve surface layers through chemical bonding when using Al as the bipolar plate.

- The inhibition effectiveness attained from the weight loss measurements agreed results in which the treated environment had a lower value than the untreated one.
- Surface observation and elemental compositions were studied by microscopic images, SEM, EDX, and contact angle data.

So, we are trying to apply this surface treatment on Al and evaluate the performance through power generation tests.

References

1. S. Marcelin, N. Pébère, *Corros. Sci.* **101**, 66–74 (2015).
2. L. B. Coelho, M. Mouanga, M. -E. Druart et al., *Corros. Sci.* **110**, 143–156 (2016).
3. J. Ma, W. Meng, L. Zhang, F. Li, T. Li, *RSC Adv.* **11**(9), 5035–5043 (2021).
4. R. Saberi Moghaddam, E. R. Draper, C. Wilson, H. Heidari, D. J. Adams, *RSC Adv.* **8**(59), 34121–34125 (2018).
5. M. V. Puc-Oxté, M. A. Pech-Canul, *Methods Mater.* **68**(3), 137–149 (2021).
6. Q. An, T. Huang, and F. Shi, Chem. *Soc. Rev.* **47**, 5061 (2018).
7. B. Arrotin, J. -M. Noël, J. Delhalle, L. Mespouille, and Z. Mekhalif, *J. Coat. Technol. Res.* **16**, 1121 (2019).
8. T. G. Harris, R. Götz, P. Wrzolek, V. Davis, C. E. Knapp, K. Ly, P. Hildebrandt, M. Schwalbe, I. Weidinger, and I. Zebger, *J. Mater. Chem. A* **6**, 15200 (2018).
9. H. -Q. Fan, D. -D. Shi, M. -M. Ding, M. -C. Li, Y. F. Cheng, and Q. Li, *Prog. Org. Coat.* **138**, 105392 (2020).
10. A. Ulman, *Chem. Rev.* **96**, 1533–1554 (1996).
11. M. Maxisch, P. Thissen, M. Giza, and G. Grundmeier, *Langmuir* **27**, 6042 (2011).
12. P. Thissen, M. Valtiner, and G. Grundmeier, *Langmuir* **26**, 156 (2010).

Chapter 7

Summary

Chapter 7: Summary

7-1. Introduction

The fuel cells are the energy sources used in various sectors. The polymer electrolyte membrane fuel cells (PEMFCs) are the most alternative techniques that has many advantages such as lightest, smallest, most durable, long stack life, fast starts up, high energy efficiency and can continuously operate at low temperature. PEMFCs are considered as ideal power source as no emission of any pollutants such as CO or NOx, and only water is produced as byproduct when hydrogen is used as fuel.

Aluminum (Al) is used as one of the most promising alternatives as bipolar plate materials in PEMFC because of its many suitable factors especially light weight and low density. Considering the above points, the corrosion behavior of Al based-materials used as bipolar plate in PEMFC are studied in this research works which is summarized below.

7-2. Corrosion Behavior of Aluminum-Carbon Composite Bipolar Plates in Polymer Electrolyte Membrane Fuel Cells

Here, the following findings were obtained as a result of conducting the PEMFC power generation test using a composite bipolar plate with Al as the reaction gas isolation plate and glassy carbon as the flow path forming material.

- No significant corrosion was observed on the Al isolation plate on the cathode side after the 500-h power generation test, but the anode side turned into white from the center of the flow path to the gas outlet side, and about 1 μm of a thick oxide film was formed.
- A thick oxide layer was formed when Al was immersed in distilled water while only a thin oxide layer was found in the saturated humid air.
- When a power generation test was conducted using Al bipolar plate coated with TiN-SBR, the cell voltage was increased significantly which was approached as similar as the performance of graphite. It indicates that Al can be used as bipolar plates without any problem by performing surface treatment in combination with a carbon channel forming material.

7-3. Corrosion Behavior of Aluminum in the Simulated and Real Environments for Use as a Bipolar Plate Component in Polymer Electrolyte Membrane Fuel Cells

In this chapter, we have reported the corrosion behavior of Al and its correlation between the simulated and real environments for use as BPs in PEMFC and the following findings were attained:

- Systematically explored the corrosion performance of Al in simulated and real environments in PEMFC. Surprisingly, the results showed that the corrosion in the real environment was more positive than that in the simulated environment.
- Almost no substantial corrosion was discovered on the Al reaction gas isolating plate on the cathode side after the 500 h of single cell power generation test. It was clearly seen that the gas isolating plate maintained its metallic luster, and no thick film was observed. Thus, it was presumed that the cathode side was in an environment where only gas was present during the single cell power generation test. However, in case of the anode side, the Al gas isolating plate maintained its luster near the gas inlet side but turned into white discoloration along the flow path from the central part to the gas outlet side, and a hydrated oxide layer of pseudo-boehmite with a two-layer structure of around 1 μm thick oxide film was formed after 500 h of single cell power generation test. So, it was suggested that during the single cell power generation test, the condensed water in which humidified gas and back-diffused water were condensed existed in the flow path on the anode side.

Thus, it is concluded that the Al would become the suitable candidate a gas isolating plate material in polymer electrolyte membrane fuel cell applications.

7-4. Corrosion behavior of aluminum in fluoride ion containing sulfuric acid solution through immersion process

In this chapter, the corrosion behavior of Al in sodium fluoride and sulfuric acid media through immersion process at 80° C was studied and significant results were observed. It was found that the corrosion rate was increasing with increasing the acid concentration as well as through addition of fluoride ions in the acid solutions. On the contrary, the only sulfate ions from the acid solutions work to slow down the corrosion rate even sometimes act as corrosion inhibitors. Thus, it is

suggested and concluded that the rule of fluoride ions and sulfate ions are as corrosion accelerator and inhibitor, respectively. Therefore, it should be taken the special consideration when Al is used for various purposes in different areas.

7-5. Stability and inhibition effect of methyl-1H-benzotriazole onto aluminum in deaerated fluoride-sulfate solution

This research work has delivered deep understanding about the stability and mechanism of the inhibitor shielding film, up to 120 h of immersion. The microscopic, atomic force microscopic, scanning electron microscopic images and EDX data of the corrosion products were taken and analyzed. The following key points were deduced from this study.

- The corrosion rate was decreased and surface roughness was improved when methyl-1H-benzotriazole was used in the test solutions.
- The lower amount and smaller sizes of Al oxides as corrosion products were found on the surface of Al.

Thus, it is concluded that the stability and inhibition effect of methyl-1H-benzotriazole molecule on Al in fluoride-sulfate solutions was clearly understood where methyl-1H-benzotriazole showed significant corrosion protection activities and are thought to be more effective in other metallic substances.

7-6. Benzylphosphonic acid self-assembled monolayer onto aluminium and performance evaluation for use in PEMFC

In this chapter, it was illustrated that BPA was deposited onto Al in a self-assembly process. The inhibition result of BPA molecule on Al surface in fluoride sulfate containing solution was carried out and depicted the following assumptions:

- The corrosion onto Al metal was measured through the adsorption of inhibitor organic molecule BPA and improved the surface layers through chemical bonding for the purpose of using Al as the bipolar plate in PEMFC.
- The inhibition effectiveness attained from the weight loss measurements agreed results in which the treated environment had a lower value than the untreated one.

- Surface observation and elemental compositions were studied by microscopic images, AFM, SEM, EDX, and contact angle data.

Thus, the surface treatment on Al was carried out to evaluate the performance as bipolar plate through power generation tests in PEMFC.

7-7. Conclusion

In summary, the corrosion behavior of Al-based materials in polymer electrolyte membrane fuel cell environment was studied in this research works. The useability and different modification techniques were carried out to improve the surface of Al using immersion process in different solutions for use as bipolar plate in polymer electrolyte membrane fuel cell environment.

List of Publications and Presentations

Articles

1. **Corrosion Behavior of Pure Aluminum in the Simulated and Real Environments for Use as a Bipolar Plate Component in Polymer Electrolyte Membrane Fuel Cells**

   Aklima Jahan, Md. Ashraful Alam, Eiichi Suzuki, and Hitoshi Yashiro, *Industrial & Engineering Chemistry Research*, 62, 20223–20235, **2023**,
   ACS. https://doi.org/10.1021/acs.iecr.3c02167

2. **Fluoride Ions Effect on the Corrosion Behavior of Pure Aluminum in Deaerated 0.05 M Sulfuric Acid Solutions**

   Md. Ashraful Alam, **Aklima Jahan,** Eiichi Suzuki, and Hitoshi Yashiro, *ChemistrySelect*, 8 (24), e202300379, **2023**. https://doi.org/10.1002/slct.202300379

3. **Surface morphology and corrosion behavior of pure aluminum and its alloys in aqueous sulfuric acid medium**

   Md. Ashraful Alam, **Aklima Jahan**, Eiichi Suzuki, and Hitoshi Yashiro, *Engineering Reports*. e12750, **2023**. https://doi.org/10.1002/eng2.12750

4. **Corrosion Behavior of Pure Aluminum in the Simulated PEMFC Environment**

   Md. Ashraful Alam, **Aklima Jahan**, Ayumu Minoura, Sekai Yonezawa, Eiichi Suzuki, and Hitoshi Yashiro, *Zairyo to Kankyo* 70 (3), 64-67, **2021**.
   https://doi.org/10.3323/jcorr.70.64

Proceedings

1. **Corrosion Behavior of Aluminum-Carbon Composite Bipolar Plates in Polymer Electrolyte Membrane Fuel Cells**

   Aklima Jahan, Md. Ashraful Alam, Sekai Yonezawa, Eiichi Suzuki, and Hitoshi Yashiro, *ECS Transactions* 108 (7), 131-141, **2022**. DOI**:** 10.1149/MA2022-01351518mtgabs

2. **Investigation of Corrosion Performance of Pure Aluminum as Bipolar Plate in PEMFC Environment**

   Aklima Jahan, Md. Ashraful Alam, Sekai Yonezawa, Eiichi Suzuki, and Hitoshi Yashiro, *ECS Transactions* 102 (5), 45-54, **2021**. DOI**:** 10.1149/MA2021-01371180mtgabs

3. **Corrosion Behavior of Aluminum in Dilute Fluoride and Sulfate Solutions for Use as Bipolar Plate of PEFC**

   M. A. Alam, **A. Jahan**, S. Yonezawa, E. Suzuki, and H. Yashiro, *ECS Transactions* 102 (5), 37-44, **2021**. DOI**:** 10.1149/MA2021-01371179mtgabs

Presentations

1. **Corrosion analysis of aluminum in PEFC using aluminum-carbon combined bipolar plates**

   Sekai Yonezawa, **Aklima Jahan,** Md. Ashraful Alam, Hitoshi Yashiro. 68th Materials and Environment Symposium, B306, Japan, October 28, **2021**.

Acknowledgement

First of all, I would like to thank one and Almighty **Allah** who has created all the things, without His blessings no one can do anything.
It was a great journey to complete my PhD (doctoral) degree at Iwate University, Japan. I am liable to express my deepest gratitude, cordial thanks, deepest sense of respect and appreciation to my reverend supervisor **Professor Dr. Hitoshi Yashiro** for his indispensable and expert guidance, valuable and constructive suggestions, and generous help in my research work. This work would not be possible without his help.
I would like to express my sincere gratitude to Dr. Eiichi Suzuki, Assistant Professor, Dept. of Chemistry and Biological Sciences, Faculty of Science and Engineering, Iwate University, Japan for his valuable advice and generous help.

I am very much grateful to the Ministry of Education, Culture, Sports, Science and Technology *(*MEXT), Japan for the financial support through Monbukagakusho (MEXT) scholarship to carry out this research work in Japan.

I am thankful to all other Professors, lab members and all those who have directly or indirectly helped me in the whole period of the research work in the Department of Chemistry and Biological Sciences, Faculty of Science and Engineering, Iwate University, Japan.

I am grateful to all the friends and community members of Bangladesh and other countries in Morioka, Japan.

I am also grateful to all of my respected teachers and friends of my primary school (elementary school), high school, college (senior high school), and universities for their valuable teachings, love, cordial help and dua.

I am so much grateful and respectful to my beloved parents for their heartfelt blessings and immeasurable sacrifice, and to other family members in Bangladesh for their inspiration and sacrifice during my study period.

I would like to express my special and sincere thanks to my dear husband **Dr. Md. Ashraful Alam**, for making my dream come true with his kind help, understanding, immense sacrifice, and cooperation.

Last but not the least, I am most indebted to my beloved sons **Anas Bin Ashraf**, **Affan Bin Ashraf**, and **Ahmad Bin Ashraf**. They have sacrificed a lot during this long journey. They have been deprived of much love from their mother.

The Author

(**Aklima Jahan**)

Dedication

This Doctoral thesis is dedicated to my beloved Parents

and

My Beloved Sons.

------ Aklima Jahan ---- March 2024----